Prions come in all shapes and sizes : mathematical modeling of protein self-aggregation and conversion

Paul Lemarre

THESE DE DOCTORAT DE L'UNIVERSITÉ DE LYON

Opérée au sein de
l'Université Claude Bernard Lyon 1
École doctorale **InfoMath**, ED 512

Spécialité : **Mathématiques**
N. d'ordre **2021LYSE1078**

Soutenue publiquement le 04 mai 2021 par

Paul Lemarre

Le prion sous toutes ses formes

Modélisation mathématiques des processus d'agrégation et de conversion des protéines

---

devant le Jury composé de :

M. Mostafa Adimy	INRIA Grenoble Rhône-Alpes	Examinateur
Mme Meredith Greer	Bates College	Examinatrice
Mme Florence Hubert	Institut de Mathématiques de Marseille	Rapporteure
Mme Véronique Maume-Deschamps	Institut Camille Jordan	Examinatrice
M. Laurent Pujo-Menjouet	Institut Camille Jordan	Directeur de thèse
M. Human Rezaei	INRA Jouy-en-Josas	Président du Jury
Mme Suzanne Sindi	University of California, Merced	Co-directrice de thèse
M. Glenn Webb	Vanderbilt University	Rapporteur

Institut Camille Jordan
Laboratoire de recherche en mathématiques Lyon/Saint-Étienne

Le prion sous toutes ses formes

Modélisation mathématique des processus d'agrégation et de conversion de protéines

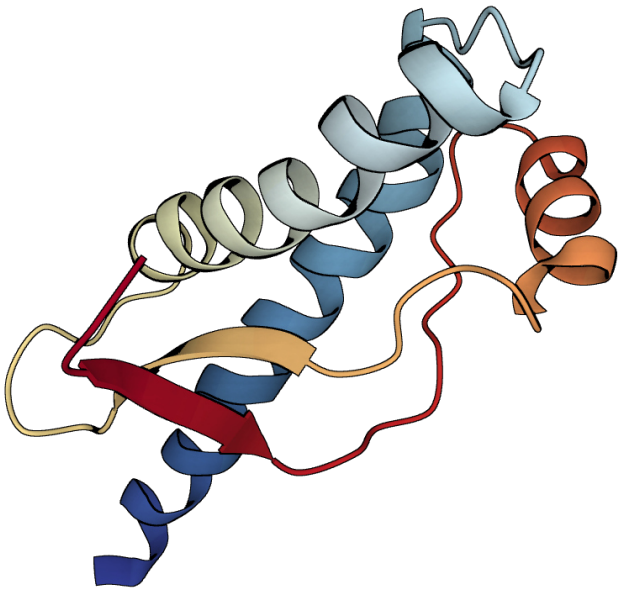

Paul Lemarre

Thèse de doctorat

UNIVERSITY OF CALIFORNIA MERCED
Université Claude Bernard Lyon 1

Résumé

Depuis la découverte de la nature des prions, de nombreux modèles mathématiques ont été proposés afin de représenter ces assemblages de protéines et leur réplication. Après quatre décennies de recherche expérimentale et conceptuelle, la compréhension des phénomènes d'agrégation de protéines, ansi que des maladies neurodégénératives qui leurs sont associées, a grandement progressé. Cependant la complexité de ces systèmes reste entière, et les modèles classiques commencent à montrer leurs limites. En particulier, aucun modèle ne reproduit l'immense diversité des objets qui sont observés au cours de la propagation des prions, alors que l'on en découvre continuellement de nouveaux sous l'avancée des procédés expérimentaux. Dans ce manuscrit, notre objectif est d'identifier les faiblesses des modèles classiques à travers l'apport de résultats biologiques récents. Par la suite, nous proposons des améliorations à ces modèles en incluant de nouveaux processus, en ajoutant des niveaux de structuration et de diversité aux agrégats. Trois axes orientent les résultats, correspondant à trois contextes biologiques différents. La première partie se déroule dans le système nerveux des mammifères, et étudie la cinétique d'auto-agrégation de PrP, la bien nommée protéine prion. Dans la seconde partie nous abordons une approche multi-échelle novatrice pour représenter la propagation d'agrégats de protéines dans des cellules de levure en croissance. La troisième partie explore la dissémination spatiale de petits oligomères dans les étapes précoces de la maladie d'Alzheimer. Ces trois axes se recoupent autour du thème central de la diversité structurale et son rôle crucial dans la propagation.

Mots clés: Agrégats de protéines, modèle cinétique, équations différentielles ordinaires, systèmes dynamiques.

Abstract

Following the discovery that prions are self-replicating assemblies of proteins, mathematical models were developed in parallel with experimental methods in order to conceptualize this phenomenon. After four decades of research, much insight has been gained into protein misfolding processes and the neurodegenerative diseases which they cause. However, the complexity of these systems remains undiminished and the classical models of protein aggregation are now showing their limits. In particular, the observed spectrum of objects generated during the propagation of prions is not accounted for in any model, whereas it keeps expanding under the development of experimental tools. In the present manuscript, our aim is to identify the weaknesses of classical models of prion propagation in light of recent biological evidence. We then suggest modified and improved models, by including different processes, by adding more levels of organization and more diversity to protein aggregates. Three main topics are presented, corresponding to different instances of protein aggregation and different biological systems. The first part takes place in the mammalian nervous system, and investigates the self-aggregation kinetics of PrP, the aptly named prion protein. In the second part, we model the replication of protein aggregates inside dividing yeast cells, by proposing a novel multi-scale approach. In the third part, we explore the spatial propagation of small protein oligomers in the early stages of Alzheimer's Disease. These three axes are linked by the central role of structural diversity in the global protein aggregation system.
Key words: Protein aggregation, kinetic model, ordinary differential equations, dynamical systems.

Résumé substantiel

La découverte de la protéine prion (PrP) et de son rôle dans la tremblante du mouton et dans la maladie de Creutzfeldt-Jakob a initié, dans le courant des années 1980, un effort de recherche colossal. Tout l'enjeu était de comprendre comment une protéine peut devenir infectieuse et causer des troubles neurologiques graves. On sait aujourd'hui que l'événement déclencheur est le changement de conformation et l'assemblage en agrégats de la protéine PrP. En effet cette protéine, ainsi que de nombreuses protéines du monde vivant, a la propriété de pouvoir être stabilisée sous plusieurs formes différentes (au sens géométrique du terme). La forme la plus courante est la forme endogène, observée dans les cellules saines du système nerveux des mammifères. Cette forme est nommée $\mathrm{PrP}^{\mathrm{C}}$ (pour "cellulaire") et correspond au PrP monomérique. Cependant, d'autres conformations existent et celles-ci ont une propension à former des assemblages, tels que des agrégats, des oligomères ou des fibres. Ces formes sont regroupées sous l'appellation $\mathrm{PrP}^{\mathrm{Sc}}$ (pour "scrapie", qui est le nom anglais de la tremblante). Ces assemblages sont eux-mêmes capables d'induire le changement de forme de monomères de $\mathrm{PrP}^{\mathrm{C}}$ en $\mathrm{PrP}^{\mathrm{Sc}}$, ce qui leur permet de s'allonger et de se répliquer. La propagation massive d'agrégats de PrP au sein du système nerveux, du cerveau en particulier, est la cause principale des déficiences cognitives subies par les individus atteints de la maladie de Creutzfeldt-Jakob, ainsi que de l'issue inévitablement fatale de cette maladie. Au-delà des maladies neurodégénératives, les processus de prions sont courants en biologie et certains systèmes en tirent même des avantages. C'est le cas des plantes et des levures par exemple, dont certaines protéines se comportent comme des prions dans le but de réagir rapidement à des changements environnementaux brusques.

La modélisation mathématique des prions a joué un rôle fondamental dans la conceptualisation et la compréhension de ces phénomènes. Les modèles considérés comme classiques aujourd'hui sont à la base inspirés des modèles physiques de la condensation et de la coagulation. Ils considèrent généralement les agrégats de prions comme des fibres longilignes, qui croissent par leurs deux bouts en convertissant successivement des monomères, et dont le nombre augmente par simple fragmentation. Ce modèle fonda-

mental a été formalisé et étudié avec beaucoup d'attention, ainsi que nombre de ses variations. Cependant, à mesure que la biologie expérimentale progresse, les complexités des systèmes d'agrégation de protéines se dévoilent et les limites des modèles classiques apparaissent. Avec l'étude intensive des prions, *in vivo* comme *in vitro*, une immense diversité de processus et de structures s'est dessinée et continue de s'étendre aujourd'hui. On sait à présent que les prions sont capables de former différents types de structures, allant du petit oligomère amorphe aux larges plaques rigides. Qui plus est, ces assemblages ont aussi une structuration interne en sous-unités ou blocs élémentaires. Enfin, différents groupes d'objets peuvent être en coévolution ou en compétition au sein du même environnement. La diversité structurelle est un aspect fondamental de la propagation des prions, encore peu pris en compte dans la modélisation. Après avoir identifié les points précis sur lesquels les modèles classiques sont en peine, nous proposons différentes adaptations et améliorations, chacune placée dans un contexte et des enjeux spécifiques. Trois axes dirigent cette approche.

La premier axe correspond à l'étude de la protéine PrP, dans le système biologique constitué par le système nerveux des mammifères. Y sont présentées les spécificités de ce système et les résultats biologiques récents, non encore expliquées par les modèles. Deux modèles sont proposés et étudiés. Le premier prend en compte l'existence d'une structure interne pour les agrégats, les sous-unités, et en déduit des explications qualitatives pour un certain nombre de phénomènes liés au problème des souches de prion. Le second modèle est dédié à la formation, par la protéine PrP, de petits oligomères *in vitro*, et leur comportement oscillatoire complexe. Dans ces deux cas, la diversité structurelle permet d'élargir le domaine de validité de modèles existants et de tirer des conclusions nouvelles sur la compréhension de la maladie à prions.

Le second axe s'intéresse à un système biologique *a priori* très différent, celui des levures. Il se trouve que les levures synthétisent plusieurs protéines qui se comportent comme des prions. La particularité de ce système est que les agrégats de prions peuvent être transmis d'une cellule mère à ses filles au moment de la division cellulaire. La propagation des agrégats au sein d'une colonie en pleine croissance correspond donc à l'évolution cinétique de centaines de milliers de systèmes couplés entre eux. L'enjeu pour le modélisateur est alors de savoir lier les phénomènes chimiques de l'échelle moléculaire aux phénomènes physiques de l'échelle cellulaire.Nous proposons un cadre théorique et pratique permettant de traiter cette difficulté à l'aide d'un modèle multi-échelles. Cette approche est mise en œuvre pour un cas précis d'expérience biologique de la littérature et permet d'obtenir des informations cruciales sur le processus moléculaire qui agit au sein des cellules.

Le troisième et dernier axe est dédié à la dissémination spatiale de petits oligomères dans le cerveau, pendant les étapes précoces de la maladie d'Alzheimer. Plusieurs protéines se comportant comme des prions sont impliquées dans la pathogénèse de cette

maladie. L'accent est mis sur le rôle particulier de la protéine Amyloïde Beta (Aβ), dont l'agrégation sous forme de grandes plaques rigides est l'un des bio-marqueurs principaux utilisés pour le diagnostic de la maladie d'Alzheimer. Les résultats biologiques récents montrent que ce sont en fait les petits assemblages oligomériques, formés très tôt dans le développement de la maladie, qui sont les plus toxiques et les plus influents sur la propagation globale de la dégénération. Nous modélisons leur évolution à l'aide d'un modèle spatial, qui permet de représenter leur dissémination au voisinage des neurones.

Chacun de ces axes met en évidence un ou plusieurs aspects de la diversité structurelle et son influence sur la propagation des prions, que ce soit au sein d'un organisme vivant comme un mammifère ou une cellule de levure, ou *in vitro*. Prendre en considération cette diversité s'avère une approche fructueuse, bien que complexe, qui permet l'élaboration de modèles modernes mieux adaptés aux observations biologiques.

Acknowledgements - Remerciements

Une thèse de doctorat, c'est un travail personnel mais pas solitaire. Je n'en serais pas arrivé au bout avec toute ma tête sans les gens qui m'entourent et sur qui je peux compter.

J'ai la chance d'avoir des amis à toute épreuve, que l'on se soit rencontrés en maternelle, au lycée, en prépa, à Centrale Lyon, dans un bar ou ailleurs. J'ai toujours pu trouver refuge chez l'un deux pour oublier mes équations le temps d'une soirée ou d'un weekend, à Paris, à Nantes ou à Lyon. Impossible de citer tous les noms sans en oublier, donc je ne m'y risquerai pas, mais il se reconnaîtront.

Je ne pourrais évidemment pas m'en tirer sans mentionner ma famille, qui s'agrandit lentement mais sûrement. Vivre éloignés nous a étrangement rapprochés, et "rentrer à la maison" n'a jamais eu autant de sens pour moi qu'aujourd'hui. A mon frère qui a toujours été et continue d'être un exemple et un modèle pour moi; à ma belle-sœur qui, dans sa grâce et sa bonne humeur, nous apprend à tous ce que c'est d'être fort; à ma nièce, petit tourbillon d'amour et de malice, qui n'a cesse de nous émerveiller. A mon père qui a sans doute été mon premier contact avec la science, qui m'a poussé à étudier et interroger, mais qui m'a aussi appris à me débrouiller et à être heureux tout simplement; à ma belle-mère et sa famille qui sont devenus ma famille, sans retenue ni demi-mesure. A ma mère qui me soutient de toutes ses forces, qui m'accompagne dans chaque moment, et me pousse à aller au bout de mes ambitions, ne serait-ce que pour la rendre fière.

Spending a little more than a year in California was as much an opportunity as it was a challenge for me, but I was fortunate enough to meet some great people. The little city of Merced now holds a special place in my heart, as it became my home away from home, filled with kind and generous people. In some way I learned who I really am, I brought myself out of my comfort zone and became a bigger version of myself. I have to thank Abbie for that, as she relentlessly pushed and supported me, made me do stuff I would have never dared dream of before. Her people welcomed me in and offered me shelter when I needed a family. Eric and Hope were always great partners in crime, either for work advice or beer recommendations, or just a moment of fun. To all the friends I made along the way and who showed me the real american experience.

The present manuscript is the conclusion of almost four years of collaboration with my advisors, Laurent and Suzanne. I could not have hoped for better people to accompany me in this journey. Their generosity and open-mindedness are without equal. They trusted me all along the way and gave me room to grow, with an endless supply of support and kindness for when I needed it. I have not heard this from many of my fellow PhD students, but I can safely say that I had a great time and I would do it again without hesitation.

Alors que je deviens petit à petit un scientifique à part entière, il m'arrive de revenir sur des années d'école et d'éducation et de me demander ce qui m'a fait choisir cette voie plutôt qu'une autre. Le premier déclic s'est fait en 1ère dans le cours de SVT de M. Garcia à La Colinière, une curiosité est née alors qui ne s'est jamais estompée. Puis viennent les années prépa, dont je garde d'excellents souvenirs, avec M. Rey, M. Almeras et M. Sauvageot, chacun une inspiration à sa manière. Arrivé à Centrale, je découvre mon intérêt pour les mathématiques et leurs applications, par le biais de Grégory Vial et Céline Helbert en particulier, dont la bienveillance et l'engouement sont contagieux. C'est en piochant parmi toutes ces figures que je me suis construit une idée du scientifique je veux être, et que j'entreprends aujourd'hui de devenir.

Finally I would like to thank the referees Florence Hubert and Glenn Webb for taking the time to review my manuscript and honoring with their presence at my defense. I would also like to thank the other members of the jury Mostafa Adimy, Meredith Greer, Véronique Maume-Deschamps and Human Rezaei for honoring me with their presence at my defense.

Contents

List of Figures

List of abbreviations

Aβ Amyloid-Beta. 19

AFM Atomic Force Microscopy. 58

APP Amyloid Precursor Protein. 110

ATP Adenosine Triphosphate. 85

GdnHCl Guanidine Hydrochloride. 82

Hsp Heat-Shock Protein. 82

ODE ordinary differential equation. 9

OvPrP Ovine PrP. 31

PrP Prion Protein. 3

SEC Size-Exclusion Chromatography. 56

SLS Static Light Scattering. 59

Chapter 1

Introduction

This manuscript is dedicated to presenting the work realized during my PhD thesis, on the subject of modeling prions with mathematical tools. The broad objective of this study is to design, compare and validate models of protein conformational change and self-aggregation. These processes, loosely referred to as prion processes, are involved in the propagation of neurodegenerative diseases such as the Creutzfeldt-Jakob Disease or Alzheimer's Disease, but they are also observed in various biological systems including yeast and plants. Chapter 1 introduces the general biological notions required to understand the concept of prions as well as some currently open problems. In a second part, we present the most commonly used mathematical models for prions, their assumptions, their formulations and their limitations. Finally, we detail the goals of the present study and the corresponding contributions by proposing three main research axes, that structure the manuscript as follows:

- Part I: Mammalian prions and the structural diversification of aggregates

- Part II: Multi-scale models in yeast prions, from molecules to phenotype
- Part III: The propagation of oligomers in neurodegenerative diseases, a spatio-temporal approach

1.1 Prion diseases and protein misfolding

Over the past three decades, prions have been the subject of intensive research and even though enormous progress has been made to understand these phenomena, they keep revealing new intricacies and puzzling problems. Prion proteins are capable of adopting multiple shapes (conformations) and have been associated with a number of diseases in mammals. In this Section, we discuss the history of the prion, the basics of prion propagation and the first mathematical models of prion dynamics.

1.1.1 The protein-only hypothesis

A brief history of the prion, summarized from the more extensive work of [Pujo-Menjouet, 2016]. The first prion disease was observed in sheep during the 18th century. This disease decimated sheep herds in the United Kingdom, and infected animals produced terrible wool, and the economic stakes motivated the first scientific studies. The sheep showed shaking and scratching symptoms that led to the name "scrapie". For almost two centuries, the nature of the pathogen agent eluded scientists. In the 1920's, unheard of cases of human dementia were reported by Creutzfeldt and Jakob. Later studies established a direct link between scrapie and the disease affecting these patients, now known as the Creutzfeldt-Jakob Disease. Since the beginning the controversy was to know whether the pathogenic agent was genetic or viral. In the 1930's, the disease was shown to be transmissible, and could even be transmitted from one species to another. This supported the idea that the pathogen was a virus. The story then continues in Papua New Guinea in the 1950's, where a strange epidemic named Kuru was spreading among a tribe called the Fore people. It primarily affected women and children. They first showed shaking symptoms then strong physical impairment, ending inevitably in fatal pneumonia. The reason was soon identified to be the cannibalistic rites of the tribes. Indeed the Fore people ate their dead. The women and children consumed the brains while the muscles were kept for the men. Just like scrapie, this disease was transmissible, and the symptoms were very similar. Thus, the connection was suggested by William J. Hadlow [Hadlow et al., 1959]. However the pathogenic agent was still not identified.

In the 1960's, it was shown that this pathogen did not contain any nucleic acids. In other words it did not contain any DNA or RNA, so it ruled out the possibility of a virus [Alper et al., 1967]. In 1967, Griffith [Griffith, 1967] suggested that the scrapie agent be a **protein**. In 1982, S. Prüsiner [Prusiner, 1982] brought definite proof of this hypothesis by showing directly that protein constituents could be infectious. This led him to coin the term "prion", as in "Proteinaceous Infectious Only". This controversial conjecture

encountered strong resistance in the scientific community, but is now broadly accepted as true. The culprit was identified as a single protein that was termed Prion Protein (PrP). This protein is now known to be associated with Creutzfeldt-Jakob Disease, all Transmissible Spongiform Encephalopathies (including scrapie and mad cow disease), Kuru, Fatal Familial Insomnia and Gertsmann-Sträussler-Scheinker syndrome. A more detailed version of this fascinating scientific "crime story" can be found in [Pujo-Menjouet, 2016]. The problem remains that this protein is normally synthesized by mammals, yet we are not all affected by the prion disease.

How can a protein be infectious? Proteins are chains of amino acids, that are encoded in the DNA and assembled by the cell machinery. As they get erected, these long chains of molecules fold into complex shapes, and adopt the 3D conformation that is most efficient thermodynamically. For most proteins, this optimal shape is unique and it defines their function. Indeed, the folding of a protein conceals some parts of the chain and exposes other parts, which are then accessible to interact with external chemical agents, proteins, membranes or receptors.

In the case of PrP, different conformations of the protein are stable. The normal shape $\mathrm{PrP}^{\mathrm{C}}$, "cellular", is found in healthy individuals and contains mostly alpha-helices. This form is not resistant to proteases, enzymes that break down proteins by cleaving peptide bonds. In individuals infected with the prion disease, another conformation of the protein is stable. This form was termed $\mathrm{PrP}^{\mathrm{Sc}}$, as in "scrapie". This abnormal form of the protein is prone to aggregation, contains mostly beta-sheets, and is much more resistant to protases [Colby and Prusiner, 2011]. The crucial characteristic of $\mathrm{PrP}^{\mathrm{Sc}}$ is that it is capable of converting $\mathrm{PrP}^{\mathrm{C}}$ to $\mathrm{PrP}^{\mathrm{Sc}}$ by directly interacting with it. This is the key mechanism in the propagation and transmission of the disease. The information of the abnormal conformation is stored in aggregates and transmitted through **templating**. As the disease progresses, aggregates grow longer and can coalesce into higher-order structures that are called amyloid plaques. This progressive conversion of PrP in the brain is coupled with progressive neuronal degradation [Collinge, 2001]. The typical symptoms are dementia, cognitive impairment, memory loss, physical impairment. Even though the pathogen has been identified, the exact cause of the neuronal degeneration is still not understood. Prion diseases are fatal and as of now there is strictly no successful therapy [Aguzzi et al., 2018].

A widespread biological mechanism. The phenomenon of protein self-aggregation and structural conversion is more general than the specific case of the prion disease [Weissman et al., 2004]. For historical reasons, such processes are now termed "prion-like processes". They are associated with many neurodegenerative diseases, although some involve different proteins than PrP: Parkinson's Disease with α-synuclein, Huntington's Disease with huntingtin, Alzheimer's Disease with Amyloid-β as well as Tau protein, and others [Soto, 2003]. But in a broader sense, prions are considered biological tools.

Indeed prion processes are known to be used in various biological systems where they act as tic switches. When a protein is converted to its prion form, its function changes and this may change the phenotype of an organism in a matter of hours. For instance this is used in plants and to resist brutal environmental changes, such as temperature shocks [March et al., 2016, Chernoff, 2016]. In this case, the prion property was selected as a bet-hedging strategy. Prions are also present in yeast, where they act as epigenetic switches [Tuite and Serio, 2010, Liebman and Chernoff, 2012]. In the present study we name "prion" the shape of any protein that can convert normally folded proteins as well as self-aggregate.

1.1.2 The prion replication process

The first step. How does the prion conversion process start? In the case mammals, all individuals synthesize PrP but most of them are not affected by the prion disease and their PrP adopts the healthy conformation PrP^{C}. The misconformation can start spontaneously, but it is an extremely rare event. Proteins evolve in a very crowded and dynamic environment, and they are sometimes forced to partially unfold. A stable aggregate may be randomly formed from PrP^{C}, and start the progress of the disease. This is called a (primary) **nucleation**, and the corresponding disease is referred to as a sporadic case. Different models of nucleation have been proposed, placing the rate-limiting step at a different level. The first idea introduced in [Cohen et al., 1994] considered that the spontaneous conversion of PrP^{C} monomers to PrP^{Sc} was the rate-limiting step. These monomers could then go and convert PrP^{C} by forming dimers with normal monomers [Laurent, 1998]. This model, called the **hetero-dimer model**, has been progressively abandoned because it could not capture pathological dynamics with feasible chemical rates [Eigen, 1996]. However it is worth mentioning for historical reasons but also because it serves as an inspirational basis for development of new models in our study, see Chapter 3. The hypothesis that is now generally accepted is the one introduced by [Lansbury and Caughey, 1995], where the rate-limiting step for nucleation is the formation of an aggregate of minimal size, a nucleus. This model is known as the **Nucleated Polymerization model** and we dedicate part of the present manuscript to its study. Some factors may increase the probability of a nucleation event happening (risk factors), such as genetic mutations. Aggregation can be triggered *in vitro* by increasing protein concentrations above physiological levels or treating proteins with denaturing agents. Once the process starts, *i.e.* a seed has been formed or introduced in the brain, the formation of aggregates from normally folded proteins is an autocatalytic process (a chemical reaction in which one product is also a reactant) that follows a deterministic evolution.

The expansion: autocatalytic conversion. Two different mechanisms are required for the aggregation process to successfully accelerate: structural change and secondary nucleation. First, the normally folded monomers have to be structurally converted to

the prion form. The mechanism that is commonly suggested is templating. By directly interacting with aggregates, the normal proteins are able to breach the energy barrier and adopt the prion conformation. In a way, the prion form "copies" itself onto normal monomers, hence the term templating. Second, in order to accelerate the process, the number of templating agents must increase. The way this happens is still partially understood from a biological standpoint. Different mechanisms have been suggested for this step, and we explore some of them in the present study. The general idea is that the presence of aggregates catalyzes the formation of new aggregates and new templating interfaces, leading to auto-amplification of the process. This is referred to as **secondary nucleation**, as opposed to primary nucleation which happens spontaneously and stochastically. In the hetero-dimer model this happens simultaneously as templating because monomers are the templating effectors, but for the Nucleated Polymerization model a different mechanism needs to be introduced.

The Nucleated Polymerization model. The most commonly accepted model for templating and secondary nucleation is the Nucleated Polymerization model, introduced by [Lansbury and Caughey, 1995]. In this representation, aggregates are linear stacks of proteins, with two ends acting as templating interfaces. The fibril ends trap normally folded proteins and convert their structure. In other words, templating and aggregate growth are assumed to be the same phenomenon. In this model, aggregates can split in multiple pieces, which allows the templating ends to increase in numbers Secondary nucleation is thus modeled as a fragmentation process. The last assumption of the Nucleated Polymerization model is the existence of a nucleus size, a minimal stable size for aggregates. If fragmentation creates an aggregate smaller than this critical size, it is immediately disassembled into normal monomers. These processes are illustrated in Figure 1.1. This model has become a standard for prion biology and its mathematical formulation has been studied in great detail (see Section 1.2). However it needs to be emphasized that the idea of linear fibrils growing and breaking apart is far too simplistic compared to the complexity of the biology. Self-aggregation mechanisms are in fact extremely complicated, and exhibit many intriguing features as we now develop.

1.1.3 Towards a modern view of prions

The general principles we presented in the previous section give an idea of how prions behave, and the classical model of Nucleated Polymerization seems relatively intuitive. Indeed it allows translating simple mechanistic ideas into equations as described in the Section 1.2. Yet, as any model, it is a simplification of reality, and the problem of prions is immensely more complicated than it seems at first. A modern view of prions requires diversity and interactions that are yet to be understood. We briefly introduce a few concepts of state-of-the-art prion research without diving into the technical material. The experimental results that support these concepts are detailed further on in the study.

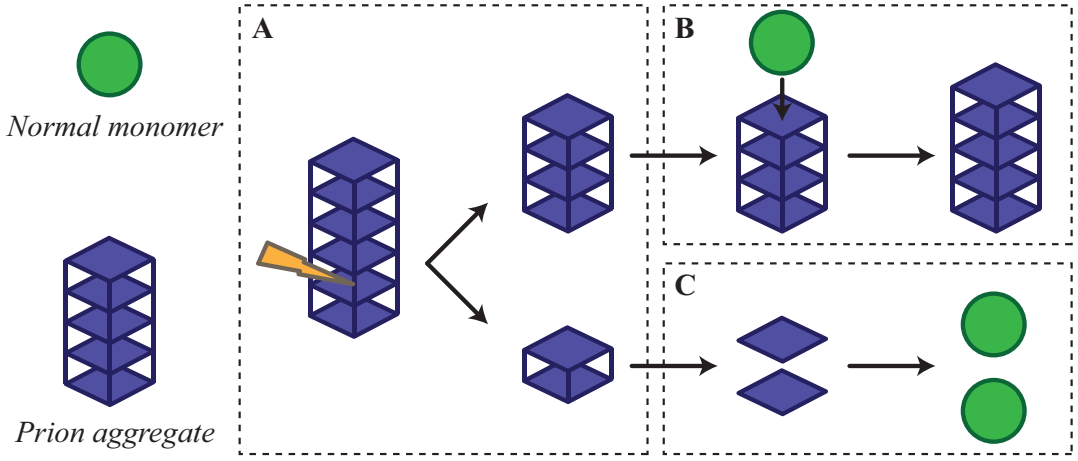

Figure 1.1 – **Illustration of the classical representation of the prion replication process: the Nucleated Polymerization model.** (A) Fragmentation of an aggregate into two pieces. (B) Growth by polymerization of normal monomers. (C) An aggregate below the nucleus size (here 3) is immediately disassembled into monomers.

The concept of strains. One biological property of prion diseases is the existence of different strains. The same disease can be propagated with different pathological properties (incubation time, symptoms, deposition pattern in the brain...) [Collinge and Clarke, 2007]. These different strains are believed to be associated with different conformations of the prion protein. There is in fact one normal conformation and a wide variety of possible prion conformations. The strain information, or strain determinant, is then stored in the three-dimensional shape of the protein. The process of templating allows copying this information onto normally folded proteins, and strains are thus transmissible. The concept of strain and the diversity of possible abnormal conformations is general for all prion-like processes. Most neurodegenerative diseases exist under various strains, that are identified based on the observable pathological markers or symptoms [Scialò et al., 2019]. Yeast prions are no exception to this phenomenon [Lindquist and Krishnan, 2005], and it is the subject of Chapter 5. The existence of these different possible conformations is broadly accepted, but it raises many questions. How do strains interact? Do they compete for normal monomers? Can they coexist?

The cloud hypothesis. These questions have yet to be answered in detail, but results show that interactions between strains are complex. Indeed strains can interact, and the outcome of these interactions is often bewildering. Strain co-evolution and selection do not seem to follow the rules of Darwinism for population dynamics, with prevalence of the most efficient predator. Technical results are detailed in dedicated Chapters 2 and 5, but we wish to introduce here the cloud hypothesis to give a peek into the modern

representation of prions. An opinion that is gaining weight in the prion community is that pathological strains (*i.e.* as given by a set of symptoms and markers) and conformational strains (*i.e.* one structure of the prion protein) are not identifiable one-to-one. More precisely, pathological/phenotypical strains are the combined result of multiple conformations of the protein co-evolving, interacting and cooperating to convert normal monomers [Collinge, 2010, Bateman and Wickner, 2013, Baskakov, 2014]. Various results support this idea and some of them are detailed in our technical reviews (Chapters 2 and 5). The problem immediately becomes more complex. This hypothesis suggests that prions exist under a wide range of conformations, hence the name "cloud hypothesis". It is applicable to all prion processes, in particular yeast prions.

Structural diversity of aggregates. One of the most striking evidence that strains are composed of multiple conformations is the structural diversity of prion aggregates. Direct observations of aggregates revealed that they are not solely composed of linear fibrils, growing and breaking apart. Different types of assemblies co-exist and co-evolve. These assemblies have different levels of structural organization. They range from small amorphous oligomers to long rigid fibrils, sometimes with inner structural organization too. They most reasonably correspond to different conformations of the protein, which links this result with the cloud hypothesis. This representation of prion aggregates populations is illustrated by Figure 1.2. Different structures necessarily have different propagation properties and chemical properties. The idea of fibrils growing by monomer addition and breaking apart needs to be nuanced with a more complete vision of many different types of structures co-evolving, competing or cooperating to recruit normal protein monomers [Igel-Egalon et al., 2019a]. This view is the modern representation of prion processes, and contrasts with the classical Nucleated Polymerization model. Aggregate diversity is common to all prion-like processes, as polymerization pathways often include different types of structures, starting with small oligomers before evolving towards longer and more rigid species, sometimes ending in large amyloid plaques. This was observed for mammalian prions [Eghiaian et al., 2007], for other protein misconformation [Haass and Selkoe, 2007] and also for yeast prions [Sharma et al., 2017]. It is a concept of particular importance because in neurodegenerative diseases, the most infectious and toxic protein assemblies are believed to be small oligomers and not the large fibrils or plaques observed in late stages [Silveira et al., 2005, Haass and Selkoe, 2007].

Understanding how and why different structures and conformations are formed, which are the most important in the propagation and toxicity of the disease are some of the foremost aspects of current prion research from a biological standpoint. Deciphering and fighting the spread of neurodegenerative diseases is a major motivation for studying these problems, but there are also potential applications in prion-like processes as can be suggested by the increasing number of examples where prions act as versatile biological tools.

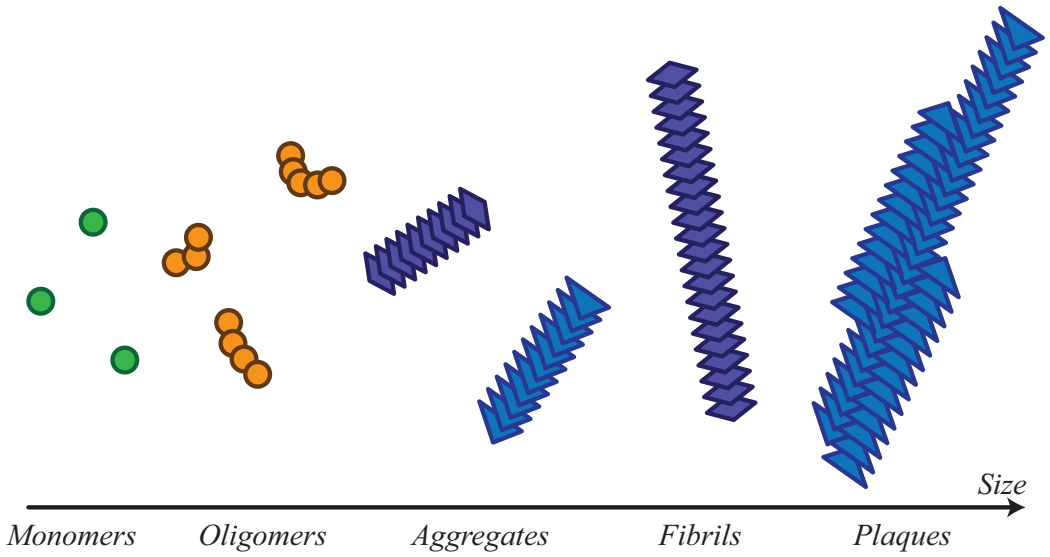

Figure 1.2 – **Schematic illustration of the diverse assemblies formed by prion proteins.** Each prion disease strain is the combined result of a dynamic range of assemblies each corresponding to a different conformation of the protein monomer.

1.2 Mathematical models of growth-fragmentation

We introduce here the classical models used for prions, and the associated mathematical tools. We focus on deterministic models of aggregation and templating derived from mass-action kinetics.[1] Note that many different modeling approaches for prion diseases have been considered in the past, different scales (epidemiology at the population level, at the scale of the individual, at the scale of cells) and different descriptions (one dimensional, two or three dimensional, discrete or continuous). Detailed reviews are proposed in [Lenuzza, 2009, Pujo-Menjouet, 2016, Sindi, 2017]. The introduction we propose here focuses on the aspects that are essential for the rest of the study. In particular we detail the mathematical model derived from the Nucleated Polymerization model of [Lansbury and Caughey, 1995], which wears the same name by extension. We establish its different formulations, the main results regarding its analysis, and stress some of its limitations.

Why mathematical models? Understanding the intricacies of prion replication and propagation is crucial in the fight against neurodegenerative diseases. Mathematical modeling builds bridges between the molecular scale, that can hardly be observed di-

[1] It needs to be emphasized that this type of model is not relevant when studying the very first steps of protein aggregation, when proteins can spontaneously and randomly change conformation. Investigating the phenomenon of sporadic nucleation is a problem in itself and requires probabilistic tools and stochastic equations, see for instance [Yvinec, 2012].

rectly *in vivo*, and events that happen at larger scales such as pathological symptoms in the case of neurodegenerative diseases, or phenotypical changes in the case of yeast. Biologists suggest mechanistic schemes and reactions based on bio-chemical data and intuition, but testing and using these hypotheses requires the help of mathematics. A mathematical model may validate or invalidate a proposed mechanism through qualitative interpretation, but it can also have a predictive value by using a quantitative interpretation and asymptotic properties.

1.2.1 Modeling aggregate growth through polymerization

The first process that needs to be represented by the model is templating. In the Nucleated Polymerization model, aggregates are linear stacks of proteins that can grow by addition of monomers to their ends. This reaction is called polymerization. The opposite reaction, loss of monomers from the aggregates, is named depolymerization. The development of models for protein aggregation was inspired by models of Oswald ripening and crystallization. Two approaches exist in order to describe aggregate size, namely discrete or continuous size description. The parameters of these equations are named identically in both formulations, with the convention that the size-dependency is indicated by a subscript in the discrete case (k_i for size i) and by a function notation in the continuous case ($k(x)$ for size x).

Discrete approach: the Becker-Döring model. With the discrete approach, we track the concentration U_i of aggregates of integer size i. If V denotes the monomer concentration, the polymerization and depolymerization reactions are described by

$$\mathrm{U}_i + \mathrm{V} \xrightarrow{\tau_\mathrm{i}} \mathrm{U}_{i+1},$$
$$\mathrm{U}_i \xrightarrow{\mathrm{k_i}} \mathrm{U}_{i-1} + \mathrm{V}.$$

Here the reaction rates are assumed to be size-dependent in all generality. This translates into an ordinary differential equation (ODE) for each variable U_i

$$\frac{dU_i}{dt} = \tau_{i-1}U_{i-1}V - \tau_i U_i V + k_{i+1}U_{i+1} - k_i U_i.$$

A minimal size has to be set for the aggregates, and it needs to be greater than or equal to 2 (since an aggregate of size 1 is a monomer). A common choice is to define a minimal size of 2. In this case, the complete (and infinite) set of ODEs obtained for

polymerization-depolymerization is the following

$$\begin{cases} & \dfrac{dU_2}{dt} = \tau V^2 - \tau_2 U_2 V + k_3 U_3 - k_2 U_2, \\ \text{for } i > 2, & \dfrac{dU_i}{dt} = \tau_{i-1} U_{i-1} V - \tau_i U_i V + k_{i+1} U_{i+1} - k_i U_i, \\ & \dfrac{dV}{dt} = -2\tau V^2 - \displaystyle\sum_{i=2}^{\infty} \tau_i U_i V + \sum_{i=2}^{\infty} k_i U_i + k_2 U_2. \end{cases} \tag{1.1}$$

The spontaneous creation of aggregates of size 2 was added, *i.e.* the reaction

$$\mathrm{V} + \mathrm{V} \xrightarrow{\beta} \mathrm{U}_2.$$

The equation on the monomer concentration was also added, so that the system verifies mass conservation. Per usual, the mass ρ is defined as the total concentration of monomers present in the system, aggregated or soluble

$$\rho = V + \sum_{i=2}^{\infty} i U_i.$$

It is straightforward to verify that system (1.1) conserves this quantity over time. This system is the Becker-Döring model, and it is a simplified version of more general coagulation models. It needs to be completed with initial conditions in order to be properly analyzed. Existence and uniqueness of solutions, as well as asymptotic convergence and steady-state solutions are classical results, see for instance [Hingant and Yvinec, 2017].

Continuous approach: the Lifshitz-Slyozov model. With the continuous approach, aggregate size is described as a real quantity x, and we now track a distribution of aggregates, where $u(x,t)$ designates the density of aggregates of size x at time t. The infinite system of ODEs becomes a partial-differential equation, more particularly the following transport equation

$$\frac{\partial u}{\partial t}(x,t) + \frac{\partial}{\partial x}\big(V\tau(x)u(x,t) - k(x)u(x,t)\big)(x,t) = 0. \tag{1.2}$$

Once again the polymerization and depolymerization rates are potentially size dependent $\tau = \tau(x)$ and $k = k(x)$. In order to define a well-posed problem, this equation needs to be completed with boundary conditions as well as initial conditions. A typical choice for boundary conditions is to impose a minimal size $x_0 \geq 0$ and

$$\begin{aligned} u(x_0,t) &= 0, \\ \lim_{x\to\infty} u(x,t) &= 0. \end{aligned}$$

This system gives the continuous counterpart of the Becker-Döring model, and is called the Lifshitz-Slyozov model. It is also a very classical model, with established results and conditions for well-posedness, existence of solutions and asymptotic convergence. The relationship between the discrete and the continuous description has been formally investigated [Yvinec et al., 2015].

Influence and limitations. The two models we introduced here, the Becker-Döring model and the Lifshitz-Slyozov model, are classical in the modeling of aggregation processes. Indeed they allow to represent the evolution of a size distribution under the influence of simple mechanistic processes such as polymerization and depolymerization. They are building blocks for more elaborated models, but they are not complete models of prion replication in themselves. One reason is that they do not include a secondary nucleation process, in other words they do not take into account the creation of new aggregates. The exception here is in the Becker-Döring model, because it includes the spontaneous creation of a minimal aggregate from two monomers. However this cannot represent a secondary nucleation process as we described earlier. Indeed this reaction is not autocatalytic, and the convergence of the system towards an aggregated state does not depend on the presence aggregates initially. We now introduce a way to make these models relevant for prion replication, by introducing an aggregate replication mechanism.

1.2.2 Modeling aggregate replication through fragmentation

One commonly suggested mechanism to represent secondary nucleation is fragmentation. The simplest representation is binary fragmentation: any aggregate can be divided into two smaller pieces. This process is entirely described by a fragmentation rate along with a fragmentation kernel. The fragmentation rate β is the size-dependent probability of an aggregate to undergo a splitting event. The fragmentation kernel κ describes the transition probability between aggregate sizes. The following formulations are almost strictly equivalent in continuous or discrete size description, for brevity we only detail the continuous size-description.

General formulation of the fragmentation equation. Without prior assumptions on the fragmentation rate or the fragmentation kernel, the fragmentation equation is written as follows

$$\frac{\partial u}{\partial t}(x,t) = -\beta(x)u(x,t) + \int_{y=0}^{\infty} \beta(y)\kappa(y,x)u(y,t)dy + \int_{y=0}^{\infty} \beta(y)\kappa(y,x-y)u(y,t)dy. \tag{1.3}$$

Aggregates of size x are lost when a fragmentation event occurs with rate $\beta(x)$, but are gained by fragmentation of any other aggregate of size y into either a piece of size x or a piece of size $y-x$ (because we consider binary fragmentation, it also creates a piece of size x). In the discrete case, this equation is translated into a system of ordinary differential equations that are strictly equivalent by replacing the integrals with sums and the size

distribution $u(x,t)$ with a set of concentrations $U_i(t)$.

Relevant assumptions for the fragmentation kernel. The value $\kappa(y,x)$ represents the probability of creating an aggregate of size x by fragmenting an aggregate of size y, as is illustrated by Figure 1.3. In order to make the fragmentation process relevant mechanistically, the fragmentation kernel has to verify certain hypotheses. The very first assumption is that the kernel is a probability density, which means that for $y > 0$

$$\int_{x=0}^{\infty} \kappa(y,x)dx = 1.$$

An aggregate can only fragment into smaller pieces, which imposes

$$\text{if } x > y > 0,\ \kappa(y,x) = 0.$$

The kernel needs to conserve mass, the total number of monomers in an initial aggregate is recovered in the sum of all its fragments. This expresses as

$$\int_{x=0}^{y} x\kappa(y,x)dx = y.$$

Finally aggregates are not assumed to have any preferential direction of fragmentation and since we consider binary fragmentation (splitting into two fragments), the fragmentation kernel has to be symmetrical

$$\text{for } y > x > 0, \kappa(y,x) = \kappa(y,y-x).$$

With these assumptions, the fragmentation equation is now reduced to

$$\frac{\partial u}{\partial t}(x,t) = -\beta(x)u(x,t) + 2\int_{y=x}^{\infty} \beta(y)\kappa(y,x)u(y,t)dy.$$

Taking into account the nucleus size. In order to fully represent the biological hypotheses of the Nucleated Polymerization model, we include the concept of a nucleus size. This size x_0 is the minimum stable size for an aggregate, which means any aggregate that is created with a smaller size is immediately disassembled into monomers. This reflects on the monomer equation as follows

$$\frac{dV}{dt} = 2\int_{x=0}^{x_0} x\int_{y=x}^{\infty} \beta(y)\kappa(y,x)u(y,t)dydx. \tag{1.4}$$

Simplification with uniform fragmentation. A classical way of simplifying the fragmentation equation is to consider uniform fragmentation. This means that any link in an aggregate is equally likely to be split. This has two consequences, first the fragmentation rate is now a linear function of size and by extension we refer to fragmentation rate

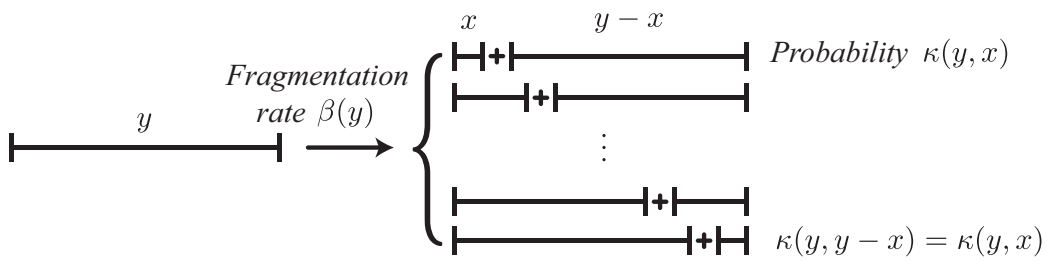

Figure 1.3 – **Illustration of the fragmentation rate and the fragmentation kernel.** An aggregate of size y can fragment with rate $\beta(y)$, into two pieces of size x and $y-x$. The fragmentation kernel $\kappa(y,x)$ represents the probability of creating a fragment of size x from an aggregate of size y.

as $\beta(x) = \beta x$. The second consequence is that the fragmentation kernel is analytically expressed as $\kappa(y,x) = \dfrac{1}{y}\chi_{[0,y]}(x)\chi_{[x_0,\infty]}(y)$, where χ_I is the indicator function of set I. This reduces the equations to

$$\begin{aligned}\frac{\partial u}{\partial t}(x,t) =& -\beta x u(x,t) + 2\beta \int_{y=x}^{\infty} u(y,t)dy,\\ \frac{dV}{dt} =& \beta x_0^2 \int_{y=x_0}^{\infty} u(y,t)dy.\end{aligned}$$

Note that in the discrete case, if the nucleus size is referred to as n_0, the monomer equation is modified to

$$\frac{dV}{dt} = \beta n_0(n_0-1)\sum_{j=n_0}^{\infty} C_j.$$

This is the only notable divergence between the discrete and continuous formulations of the fragmentation equation with a nucleus size. With all these terms introduced and explained, we are now ready to formulate a complete model of Nucleated Polymerization.

1.2.3 The Nucleated Polymerization model

General formulation. The processes introduced above are now combined and used to formulate the complete Nucleated Polymerization model. Overall it includes the following mechanisms

- Monomers are produced with a constant speed λ and degraded with a rate γ.
- Aggregates grow by addition of monomers with second order reaction rate $\tau(x)$. Depolymerization is not explicitly included in this formulation.

- Aggregates fragment with rate $\beta(x)$ and kernel $\kappa(y, x)$, and are stable only for a size larger than the nucleus size x_0.

- Aggregates are degraded with rate μ.

These biological processes and reactions are illustrated and summarized in Figure 1.4.

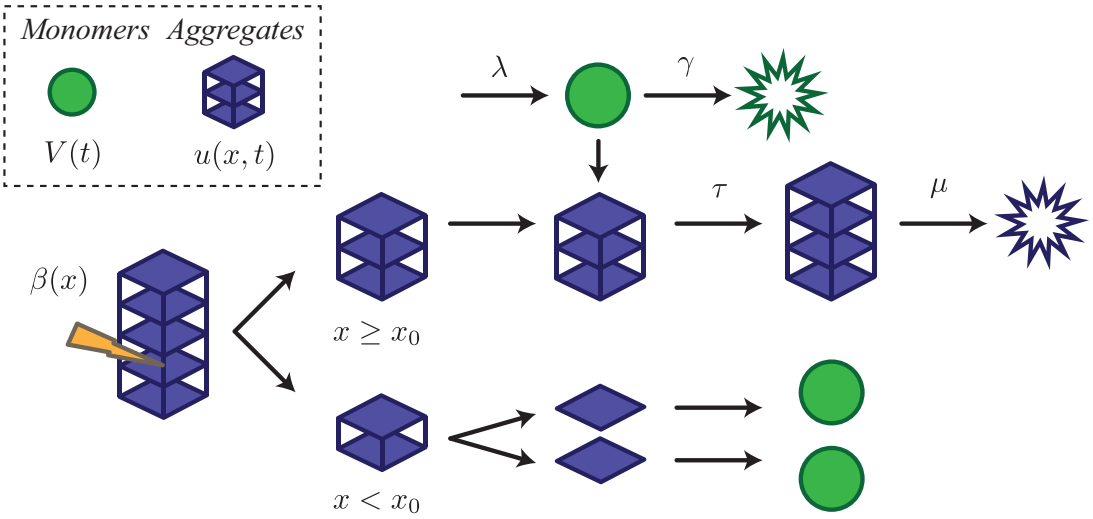

Figure 1.4 – **Biological processes involved in the Nucleated Polymerization model** and notations used in the mathematical formulation, as described in the main text. The figure illustrates the case of a nucleus size x_0 of 3.

In the continuous description, the general formulation of the Nucleated Polymerization model is written as follows

$$\begin{cases} \dfrac{dV}{dt} = \lambda - \gamma V - V \displaystyle\int_{y=x_0}^{\infty} \tau(y)u(y,t)dy + 2\int_{x=0}^{x_0} x \int_{y=x_0}^{\infty} \beta(y)\kappa(y,x)u(y,t)dy, \\ \dfrac{\partial u}{\partial t}(x,t) + \dfrac{\partial}{\partial x}(\tau(x)Vu(x,t)) = -\mu u(x,t) - \beta(x)u(x,t) + 2\displaystyle\int_{y=x}^{\infty} \beta(y)\kappa(y,x)u(y,t)dy. \end{cases} \tag{1.5}$$

The equivalent system of ODEs in the discrete size description is the following (using the

same notations for the reaction rates)

$$\begin{cases} \dfrac{dV}{dt} = \lambda - \gamma V - V \displaystyle\sum_{j=n_0}^{\infty} \tau_j U_j + 2 \sum_{i=2}^{n_0} i \sum_{j=n_0}^{\infty} \beta(j)\kappa(j,i)U_j, \\ \dfrac{dU_i}{dt} + \tau(i)VU_i - \tau(i-1)VU_{i-1} = -\mu U_i - \beta(i)U_i + 2\displaystyle\sum_{j=i}^{\infty} \beta(j)\kappa(j,i)U_j. \end{cases} \tag{1.6}$$

This system has been extensively studied analytically [Masel et al., 1999, Greer et al., 2006, Prüss et al., 2006]. In particular the relationship between the discrete and continuous formulations is well established [Doumic et al., 2009]. The case most studied and used in practice is the case of uniform fragmentation.

Uniform fragmentation and moment closure. When we add the assumption of uniform fragmentation and a constant polymerization rate τ, the system simplifies as

$$\begin{cases} \dfrac{dV}{dt} = \lambda - \gamma V - \tau V \displaystyle\int_{y=x_0}^{\infty} u(y,t)dy + \beta x_0^2 \int_{y=x_0}^{\infty} u(y,t)dy, \\ \dfrac{\partial u}{\partial t}(x,y) + \tau V \dfrac{\partial u}{\partial x}(x,t) = -\mu u(x,t) - \beta x u(x,t) + 2\beta \displaystyle\int_{y=x}^{\infty} u(y,t)dy. \end{cases} \tag{1.7}$$

This partial differential equation system is particularly interesting because it admits a moment closure. If we define the first two moments of the aggregate distribution as

$$U(t) = \int_{x=x_0}^{\infty} u(x,t)dx,$$
$$P(t) = \int_{x=x_0}^{\infty} xu(x,t)dx,$$

it is straightforward to verify that these variables are solutions of a three-dimensional ODE system. The system obtained by moment closure is written as follows

$$\begin{cases} \dfrac{dV}{dt} = \lambda - \gamma V - \tau VU + \beta x_0^2 U, \\ \dfrac{dU}{dt} = \beta P - 2\beta x_0 U - \mu U, \\ \dfrac{dP}{dt} = \tau VU - \beta x_0^2 U - \mu P. \end{cases} \tag{1.8}$$

This system behaves like a SEI epidemiology model [Prüss et al., 2006]. It has two possible equilibria, and the behavior of the solutions is based on a basic reproductive number. This is all summarized by the following theorem.

Theorem 1.1. *The Nucleated Polymerization model. Assume all parameters $\lambda, \gamma, \tau, \beta$ and x_0 are positive. For each initial condition taken in $X = \{(V, U, P) \in \mathbb{R}^3 : V, U, P - x_0 U \geq 0\}$, the system (1.8) admits a unique solution $(V(t), U(t), P(t))$ for $t \geq 0$, with $(V(t), U(t), P(t))$ in X.*

We define $\mathcal{R}_0 = \frac{\lambda}{\gamma} \frac{\beta\tau}{(\mu+\beta x_0)^2}$. Two steady-states are possible.

1. *The Disease-Free Equilibrium $(V, U, P) = \left(\frac{\lambda}{\gamma}, 0, 0\right)$. This equilibrium exists for any choice of positive parameters. It is globally asymptotically stable if and only if $\mathcal{R}_0 \leq 1$.*

2. *The Endemic Equilibrium $(V, U, P) = (V^*, U^*, P^*)$, with*

$$\begin{aligned} V^* &= \frac{(\mu + \beta x_0)^2}{\beta\tau}, \\ U^* &= \frac{(\mu + \beta x_0)^2}{\mu\tau(\mu + 2\beta x_0)}(\mathcal{R}_0 - 1), \\ P^* &= \frac{\mu + 2\beta x_0}{\beta} U^*. \end{aligned}$$

   It is feasible ($U^* > 0$ and $P^* > 0$) and globally asymptotically stable if and only if $\mathcal{R}_0 > 1$.

The proof of this theorem is obtained using classical Lyapunov functions. It is developed for instance in [Greer et al., 2006]. The Endemic Equilibrium corresponds to steady-state distribution of aggregates that is analytically tractable, see [Engler et al., 2006]. Because of these properties, the Nucleated Polymerization model is an attractive choice for the study of prions. Its simplification into a three-dimensional system reduces the complexity and the number of parameters, which can then be inferred quantitatively [Masel et al., 1999, Tanaka et al., 2006, Rubenstein et al., 2007]. For all of these reasons, the Nucleated Polymerization model is a starting point for the development of new and modern models.

Generalizations and extensions. Some studies have suggested more general formulations of this model, in order to overcome some of its limitations. In particular, the effect of size-dependent parameters (polymerization rate and fragmentation rate) has been studied in detail using a principal eigenvalue method [Calvez et al., 2009, Calvez et al., 2010, Doumic and Gabriel, 2010, Calvez et al., 2012]. In the general case, stability results are not as strong as the ones obtained for constant rates and uniform fragmentation. Overall it is hypothesized but not proven that, under very specific parameter choices, two endemic equilibria exist, with one of them stable and the other unstable. Those parameter choices also yield multi-modal steady-state distributions, which are interesting concerning the biology, but too difficult analytically to be used quantitatively.

Another extension worth mentioning was presented in [Greer et al., 2007]. This study included a non-linear incidence rate depending on the concentration of aggregates, as well as a coalescence process through which two aggregates can join and form a larger aggregate. Overall those modifications do not change the qualitative behavior of the model and do not change the expression of the basic reproductive number $\mathcal{R}_0$. The Nucleated Polymerization model was also extended and used in the context of yeast prions, see Subsection 5.2.2 for more detail.

1.2.4 Limitations of the classical models

Global behavior. The Nucleated Polymerization model, just like the Becker-Döring model, is a global model. Its long-term behavior depends on the choice of parameters but not on the choice of initial conditions. This means that under this perspective, the (asymptotic) outcome of an infection only depends on the environment and chemical conditions, but not on the inoculum or seed itself, as long as it contains a positive concentration of aggregates. It is relevant when studying mammalian neurodegenerative diseases *in vivo*, since aggregation can only be detected once it is well advanced and already irreversible. However, *in vitro* studies of aggregation phenomena require taking into account the effects of low densities of aggregates. This problem is also crucial in the context of multiple interacting strains since the outcome depends strongly on the initial seed, as we develop in Chapter 2. In the context of yeast prions, global models are also limited because these prions have the characteristic of being reversible, and this is the object of more discussion in Chapter 5. The opposite of a global model is a multi-stable model, where multiple steady-states may be stable at the same time and solutions may be attracted to one or another depending on the initial condition. To the best of our knowledge, the only multi-stable models ever introduced in the context of prion biology were suggested by [Laurent, 1998] and inspired by the hetero-dimer model.

Aggregate diversity. The models we introduced up until now only include one type of structure, with a simple growth and replication process. This makes the equations straightforward and the analytical study tractable. However it is in conflict with experimental observations. In particular, as we mentioned previously, prions are composed of many different co-evolving structures, corresponding to different protein conformations. As such, the classical models do not capture this aspect but they can be used as building blocks to design more versatile models. Identifying the mechanisms behind structural diversification would provide insight into many perplexing features of prion propagation.

Fragmentation is not a plausible mechanism. Discussion with biologists suggests that fragmentation of mammalian prion aggregates *in vivo* seems unlikely (personal communication with H. Rezaei). Indeed these aggregates evolve extra-cellularly in the cerebro-spinal fluid. This means that they do not interact with intra-cellular chaperones and machinery that are associated with protein quality control and fragmentation. In the case of yeast prions, chaperones are indeed involved in the propagation of aggregates,

and fragmentation is believed to be the main process of aggregate replication. However the role of these chaperones is not clearly understood and is still controversial, see Subsection 5.1.3. As much as fragmentation is appealing in terms of modeling, because it leads to tractable equations with simple behavior, there needs to be efforts in suggesting and exploring other secondary nucleation mechanisms.

1.3 Aims and contributions

In this study, we aim at developing new models of prion processes that are adapted to the biological context and the most recent experimental findings. Three main axes are defined, each corresponding to a different biological setting and involving a different mathematical approach.

1.3.1 Structural diversification in mammalian prions

Recent *in vitro* and *in vivo* studies of mammalian prions revealed the importance of structural diversity in the propagation of the disease [Igel-Egalon et al., 2017, Igel-Egalon et al., 2019b]. It has become clear that aggregates have an internal structure, they are composed of elementary subunits, and different types of aggregates (each with their own types of elementary subunits) coexist in a single strain. Part I is dedicated to the study of this aspect. In this part, we propose a review of state-of-the-art biological results on aggregate structural diversity and the problems it is associated with, as well as a review of mathematical models that take into account this diversity. Two contributions are then proposed. First we suggest a model of aggregate growth and fragmentation by including a novel species, the elementary subunit, as an intermediate in the polymerization pathway. This allows us to bring new insight into strain interaction and coexistence problems. These results are published in [Lemarre et al., 2018]. Next, we propose and study a model for the formation of small PrP oligomers *in vitro*. Such oligomers exhibit the same spectrum of diversity as infectious prion aggregates. In particular, depolymerization of these oligomers reveals intricate dynamics, with nonlinear effects of concentration as well as the interaction of multiple timescales. Our model captures some of these qualitative features by including a complex depolymerization pathway.

1.3.2 Multi-scale prion aggregate propagation in yeast cells

The case of yeast prions is quite different from mammalian prions, and it comes with its own complexity. Part II focuses on this system. This part introduces the specificities of yeast prions, in terms of biology but also in terms of mathematical modeling. We then propose a mathematical framework designed to tackle the multi-scale aspect of the yeast prion system. This framework is based on the use of impulsive differential equations. We also introduce a kinetic model of prion replication that is bi-stable. This aspect of the model is essential and specific to yeast prions, and contrasts with every model used

before in this context. Our results bring new insights into the study of yeast prions, suggesting a different perspective on long established results and giving leads for further investigation. These results are published in [Lemarre et al., 2020].

1.3.3 Spatial propagation of oligomers in neurodegenerative diseases

Part III focuses on the study of the spatial propagation of neurodegenerative diseases in the brain. We review biological results concerning the role of protein misfolding in neurodegenerative diseases, with a focus on Alzheimer's disease. In particular we emphasize on the importance of structural diversity coupled with spatial propagation in the progression of the disease. We also review previous mathematical studies that investigated the spatial propagation of neurodegeneration. We then propose a model that is based on growth-fragmentation equation coupled with size-dependent diffusion, and use it to study the propagation of small Amyloid-Beta (Aβ) oligomers during the very early stages of Alzheimer's Disease. These results are published in [Andrade-Restrepo et al., 2019].

Part I

Mammalian prions: kinetic models of structural diversification

Chapter 2

Introduction to structural diversification and open problems

This first part is dedicated to the study of mammalian prions, namely the conformational change and self-aggregation of the protein PrP *in vivo* and *in vitro*. As mentioned in Chapter 1, these processes are involved in the propagation of various fatal and incurable diseases including Creutzfeldt-Jakob disease, Kuru, fatal familial insomnia, Gertsmann-Straüssler-Scheinker syndrome and all transmissible spongiform encephalopathies [Ironside et al., 2018]. This chapter introduces the main results obtained by the biologists and the questions that remain open. We also address previous modeling studies of particular interest.

2.1 The diversity of prion aggregates

We now detail state-of-the-art knowledge and biological observations about mammalian prions, with particular emphasis on the various levels of diversity involved.

2.1.1 The strain phenomenon

Pathological strains and conformational strains. Historically, strains were defined based on pathological properties, including symptoms, protein deposition and brain lesion

patterns, incubation time and other biological markers [Morales, 2017]. However, with the protein-only hypothesis and a clearer understanding of the pathogenesis, strains were linked to the structural information propagated by prion aggregates [Collinge and Clarke, 2007]. A strain would then be the consequence of the propagation of one specific misconformation of PrP, or a conformational strain. The reality is more complex, as is illustrated for instance by results from [Le Dur et al., 2017], where inoculation of mice with the same pathological strain leads to infection by different pathological strains, depending on the level of PrP^C expression in these mice and the level of dilution of the inoculum. The structural information transmitted is the same in each case, but a different strain is selected in the host depending solely on the amount of available PrP^C. This suggests that pathological strains and structural strains are not identifiable in a one-to-one relation. Pathological strains are in fact caused by a combination of different protein conformation, and their associated assemblies. If not specified otherwise, we use the word "strain" when referring to pathological strains, and "conformation" to refer to one conformation of the protein.

Interactions of prion strains. Multiple studies have investigated the interaction of different strains in the same host. One typical way of probing these interactions is with co-infection studies. An interesting result is that co-infection by different strains yields an outcome that depends on the timing and the order of the different inoculations [Langenfeld et al., 2016]. In particular, long incubation strains seem to interfere with the progression of short incubation strains [Marín-Moreno et al., 2018]. On the other hand, some strains do not seem to interact in any way and replicate independently [Eckland et al., 2018]. Even further than selecting a single strain from an initial mixture of different conformations, co-infection sometimes leads to co-occurrence of different pathological strains in the same host [Langenfeld et al., 2016, Kobayashi et al., 2019]. Let us imagine a parallel with population dynamics and evolution. One would think that competition for a common resource (PrP^C monomers) drives the system towards the selection of the species (prion assemblies) that is most efficient at recruiting monomers. In molecular biology and virology this is referred to as selection of the best replicator [Nee, 2016]. It seems difficult to classify pathological strains using this reasoning considering the non-trivial co-infection results. One could argue that the best replicator reasoning should be applied to individual aggregated species, considering that these species co-exist and cooperate to produce different pathological strains. This reasoning is also difficult to support, since it has been observed that over the course of the disease, the structures that are selected and favored inside the host are not necessarily the structures most efficient at replicating [Igel-Egalon et al., 2019b]. Overall, the structural composition of pathological strains remains difficult to identify, and the interactions between these different strains are consequently difficult to predict. They require specific modeling approaches, as the classical models are limited when it comes to studying interacting

strains, as we develop in Subsection 2.2.1.

2.1.2 Structural diversity of mammalian prion assemblies

With the progress of experimental technology, new insight has been provided on the structure of prion aggregates. It is now clear that the idea of linear fibrils growing and fragmenting is outdated.

Internal structure of aggregates. Bio-chemical analysis of PrP^{Sc} aggregates revealed an internal structure that differs from the model of monomers assembling one by one on top of each other. Indeed [Igel-Egalon et al., 2017] showed the existence of an elementary protomer or subunit, which constitutes the aggregates. This was evidenced by a fast-dilution method, where aggregates were isolated and in the absence of available monomers, the size distribution changed. However the size distribution was not shifted, instead a transfer was observed between two clearly identified modes in the distribution. This indicated the disassembly of the aggregates into a smaller species without accumulation of any intermediate. Further investigation revealed that this smaller species did not correspond to monomers. For the studied strains, PrP^{Sc} aggregates are thus composed of elementary subunits and are in equilibrium (detailed balance) with them. It is hypothesized that this is a common property of all prion aggregates. The subunits themselves are composed of a few monomers, the exact number is evaluated at 3 although this might depend on the type of aggregate and the strain considered [Igel-Egalon et al., 2017]. The way these subunits are formed and the precise reactions that drive the equilibrium between aggregates and their subunits are not yet known in detail.

Poly-dispersity of assemblies. In addition to the internal structure of aggregates, it was recently observed that different types of aggregates co-evolve during the disease progression. Of course these different types of aggregates each have their own inner structure. In particular, it appears that some aggregates are formed during the early stages of the disease, before being transformed into different, larger aggregates later on [Igel-Egalon et al., 2019b]. These observations correlate with *in vitro* observation of polymerization pathways which include sequential steps with different associated structures. The early stages of spontaneous *in vitro* aggregation involve the formation of small oligomers [Eghiaian et al., 2007, Chakroun et al., 2010], also referred to as micelles [Alvarez-Martinez et al., 2011, Hingant et al., 2014]. Early oligomers are already diverse with multiple subpopulations, and inner structures, as is detailed in Chapter 4. Prolonged incubation of these oligomers leads to the formation of PrP^{Sc} fibrils. Different types of assemblies are not just associated with a difference in the size of aggregates, as would be suggested by observing size-distribution data only. In fact, different oligomers observed *in vitro* or different types of aggregates observed *in vivo* at different stages of the disease are associated with different conformations of the protein. The transition from one type of aggregate to another implies a structural change of the protein. The sequential transition between different structures is referred to as the polymerization pathway.

Overall, at least four levels of organization are identified among prion aggregate populations (of a single pathological strain), corresponding to different scales. An illustration of this diversity and the different scales involved is proposed in Figure 2.1. At the scale of protein monomers, structural information is stored in the three-dimensional conformation of peptide chains. Inside aggregates, monomers are organized in subunits, or elementary bricks. Aggregates themselves are organized in a size distribution. Finally at the largest scale, different aggregate types (each with their inner structure, and their specific protein conformation) coexist and interact, in order to produce multimodal and dynamic size-distributions. The kinetics of formation and interactions between these different structures and scales are not fully understood and call for mathematical modeling.

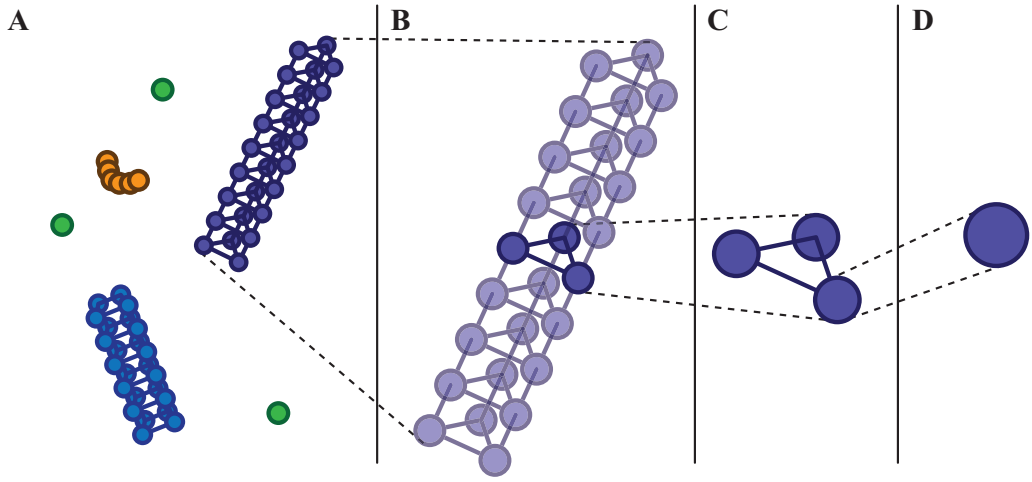

Figure 2.1 – **Illustration of the four levels of organization in PrP^{Sc} aggregate populations.** (A) At the scale of the host, different types of aggregates and oligomers co-evolve. (B) Aggregates are organized in a size structure. (C) Aggregates have an inner structure, they are composed of subunits. (D) Inside subunits, the protein monomers contain structural information in their conformation.

2.1.3 The species barrier

Strain adaptation. A concept that is intimately related to strains is the species barrier, along with strain adaptation [Igel-Egalon et al., 2018]. Some prion strains are transmissible in heterologous hosts, in other words from one mammalian species to another, or from one version of PrP^{C} to another. Some strains however, are not transmissible across species, and when transmission is possible in one direction it may not be possible in the reverse direction. However the most interesting and puzzling result is that in some cases transmission is possible only after an adaptation phase [Baskakov, 2014]. Serial passage (*i.e.* infecting individuals one after another with brain homogenates) in a new host species leads to adaptation of the strain. The incubation time decreases upon each

passage until it reaches a final value [Le Dur et al., 2017]. The number of sequential infections required for full adaptation depends on the strain and species configuration, but is highly reproducible. Some models have been suggested to interpret these results, with the formation of intermediate conformations, and convergence towards a host-dependent optimal strain (with the question remaining of what optimal means).

The role of structural diversity. Recent findings suggest that the key to understanding strain adaptation lies in the concept of aggregate diversity [Igel-Egalon et al., 2019a]. Indeed the species barrier, when it exists, is more difficult to cross by one isolated aggregated species from a pathological strain than by inoculating the full mix of assemblies that compose this strain. This suggests that the diverse structures and conformations that compose pathological strains interact and cooperate in the context of strain adaptation.

In recent years, the discoveries in the field of mammalian prion biology have unveiled increasing levels of complexities and diversity in prion aggregates. Not only do they exist in different strains, each strain is the combined result of the dynamic interaction of multiple types of aggregates, each having their own inner structure and their own specific formation pathway. Structural diversity encapsulates all these levels of organization, and it is crucial to understand how and why this diversity exists in order to decipher the properties of prion propagation.

2.2 State-of-the-art models

We now detail the state of prion modeling, with the perspective of the open problems mentioned earlier and in particular with respect to structural diversity and strain interactions.

2.2.1 The Nucleated Polymerization model and the limitations of global models in the context of interacting strains

Subsection 2.2.1 is adapted from published work [Lemarre et al., 2018].

Generalizing the Nucleated Polymerization model. The first step in modeling prion diversity is to start from classical and established models. The Nucleated Polymerization model, as we emphasized earlier, does not take into account structural diversity. Yet, it may be used to model a multiple strain scenario. We investigate this approach by introducing different independent competing strains, each interacting only with the monomers and evolving following a Nucleated Polymerization model (with strain-specific parameters). This model is illustrated by Figure 2.2 in the case of two independent strains. Let us consider the general case of N strains, with $N \geq 2$. Each strain evolves according to the Nucleated Polymerization model with uniform fragmentation introduced in Subsection 1.2.3, but with specific parameters. The polymerization rate τ_i, the fragmentation rate β_i, the nucleus size x_i and the degradation rate μ_i are all positive constants

dependent on the strain index $i = 1 \dots N$. Since they all follow a uniform fragmentation process, we have moment closure and we can write a system of ODEs. The variables of this system are the monomer concentration V and the first two moments of the size distribution for each strain U_i and P_i.

$$\begin{cases} \dfrac{dV}{dt} = \lambda - \gamma V + \displaystyle\sum_{i=1}^{N} (-\tau_i V U_i + \beta_i x_i^2 U_i), \\ \dfrac{dU_i}{dt} = \beta_i P_i - \mu_i U_i - 2\beta_i x_i U_i, \ i = 1 \dots N, \\ \dfrac{dP_i}{dt} = \tau_i V U_i - \mu_i P_i - \beta_i x_i^2 U_i, \ i = 1 \dots N. \end{cases} \tag{2.1}$$

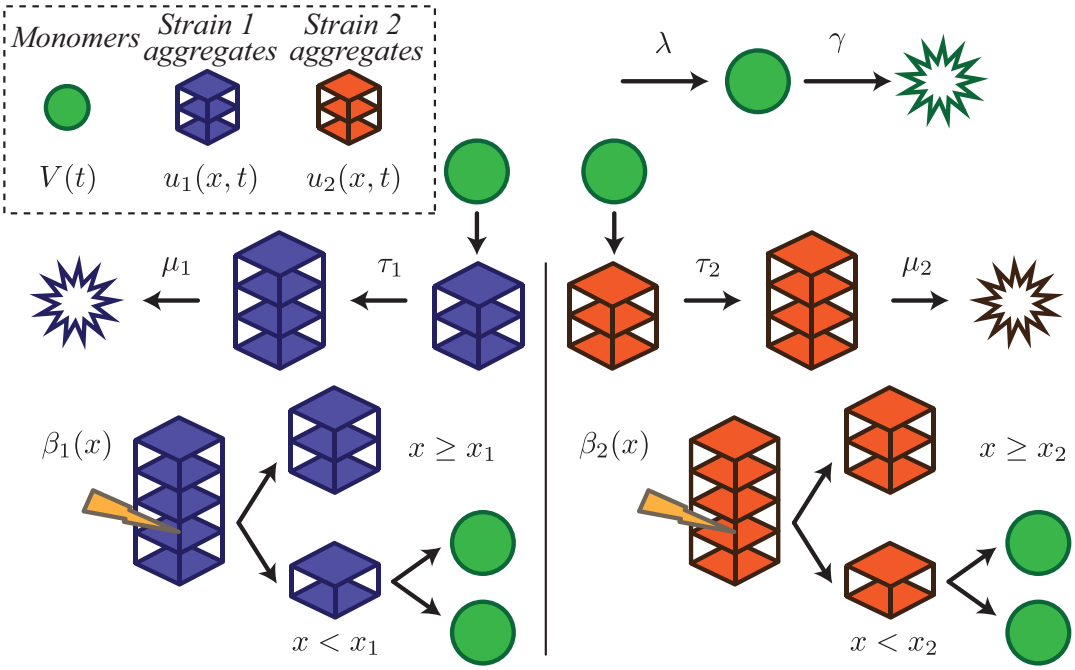

Figure 2.2 – **Variables and parameters for the Nucleated Polymerization model generalized to the case of two strains.**

Equilibrium analysis. Let us now consider the different possible steady-states in our multi-strain Nucleated Polymerization model given by System (2.1). Note that different steady-states are possible depending on the parameters. First, the **Disease-Free Equilibrium**, when all prion strains become extinct, always exists and is given by

$$(V, U_1, P_1, \dots, U_N, P_N) = (\lambda/\gamma, 0, 0, \dots, 0, 0).$$

Then for each strain $i = 1, \dots N$, there is a **Strain-Specific Endemic Steady-State** corresponding to the asymptotic presence of strain i only. It is given by

$$(V, U_1, P_1, \dots, U_i, P_i, \dots, U_N, P_N) = \Big(\frac{(\mu_i + \beta_i x_i)^2}{\beta_i \tau_i}, 0, \dots, 0, \frac{\lambda\beta_i\tau_i - \gamma(\mu_i + \beta_i x_i)^2}{\mu_i\tau_i(\mu_i + 2\beta_i x_i)}, \frac{\lambda\beta_i\tau_i - \gamma(\mu_i + \beta_i x_i)^2}{\mu_i\beta_i\tau_i}, 0, \dots, 0\Big).$$

We note that the non-zero quantities in the steady-state correspond exactly to the Nucleated Polymerization endemic steady-state for the strain in isolation. The strain-specific endemic steady-state is biologically feasible (*i.e.* all concentrations are positive) only when $\frac{\lambda}{\gamma}\beta_i\tau_i > (\mu_i + \beta_i x_i)^2$. As introduced in the single strain case, we define a strain-specific basic reproductive number

$$R_0^i = \frac{\lambda}{\gamma}\frac{\beta_i\tau_i}{(\mu_i + \beta_i x_i)^2}, \tag{2.2}$$

and note that biological feasibility of the strain-specific endemic steady-state corresponds to exactly $R_0^i > 1$.

Next, we consider steady-states where multiple strains exist together. We define such steady-states to be **Coexistence Steady-States**. We note that for each strain at steady-state, the following strain-specific relation on the normally folded protein monomer density must be satisfied:

$$V = \frac{(\mu_i + \beta_i x_i)^2}{\beta_i\tau_i} = \frac{\lambda}{\gamma}\frac{1}{R_0^i}. \tag{2.3}$$

As such, only strains with the same basic reproductive number can exist together at steady state. This means that as long as strains have different steady-state normal monomer concentrations, they cannot coexist at steady-state in this multi-strain model. Because the reproductive number of a strain R_0^i is a function of the strain-specific biological parameters, it is highly unlikely that these R_0^i coincide exactly. Moreover, even if by chance two strains had an identical R_0^i, coexistence would not be robust as the slightest perturbation of one parameter would completely remove the possibility of a coexistence equilibrium.

Asymptotic behavior. In addition, much like the original Nucleated Polymerization model, only one steady-state at a time will be asymptotically stable. The behavior of this multi-strain model (2.1) is driven by the following theorem.

Theorem 2.1. *Assume all parameters λ, γ and $\tau_i, \beta_i, x_i, \mu_i$ for $i = 1 \dots N$ are positive. For each initial condition taken in*

$$X = \{(V, U_1, P_1, \dots, U_N, P_N) \in \mathbb{R}^{2N+1} : V, U_1, P_1 - x_1U_1, \dots, U_N, P_N - x_NU_N \geq 0\},$$

the system (2.1) *admits a unique solution that is in X for all $t \geq 0$. Further suppose that*

the quantities $R_0^i = \frac{\lambda\beta_i\tau_i}{\gamma(\mu_i+\beta_i x_i)^2}$ *are distinct pairwise and define*

$$\mathcal{R}_0 = \max_{i=1\ldots N} \left\{R_0^i\right\}.$$

If $\mathcal{R}_0 \leq 1$*, the disease-free equilibrium* $(\lambda/\gamma, 0, 0, \ldots, 0, 0)$ *is globally asymptotically stable on* X*.*
If $\mathcal{R}_0 > 1$*, suppose Strain 1 verifies this maximum (renumbering the strains if necessary), there exists an endemic equilibrium for each strain with* $R_0^i > 1$ *(including Strain 1). The equilibrium involving only Strain 1 is given by*

$$\left(\frac{(\mu_1+\beta_1 x_1)^2}{\beta_1\tau_1}, \frac{\lambda\beta_1\tau_1 - \gamma(\mu_1+\beta_1 x_1)^2}{\mu_1\tau_1(\mu_1+2\beta_1 x_1)}, \frac{\lambda\beta_1\tau_1 - \gamma(\mu_1+\beta_1 x_1)^2}{\mu_1\beta_1\tau_1}, 0, 0, \ldots, 0, 0\right),$$

and is globally asymptotically stable on $\{(V, U_1, P_1, \ldots, U_N, P_N) \in X : U_1 > 0, P_1 > 0\}$*. Note that if* $U_1(0) = P_1(0) = 0$*, the outcome will be given by the same theorem without considering Strain 1.*

Proof. The existence and uniqueness of solutions is proved in the same fashion as in the single strain case, with direct adaptation of the proof provided in [Prüss et al., 2006]. The global results rely on Lyapunov functions, and the proof is presented in Appendix A. □

The limitations of global models. The previous theorem means that the Nucleated Polymerization model, when generalized to multiple independent strains, predicts the prevalence of at most one strain. Two strains can coexist at steady-state only if their basic reproductive numbers are equal, which is highly constraining in terms of biochemical parameters. This model predicts an outcome where the most efficient strain, which in this case means the strain with the highest basic reproductive number R_0, takes over all the other strains in presence. In other words, the Nucleated Polymerization model is a global model, even in the case of multiple strains, and does not allow for coexistence of strains. This is conflicting with most experimental results we presented above. We wish to emphasize that this limitation of the Nucleated Polymerization model is common to all global models, *i.e.* models for which there is at most one globally stable equilibrium. In particular, this is also the case of the Becker-Döring model and its multiple-strain behavior is similar [Wattis, 1999]. In order to allow for more varied strain interactions and give insight into problems such as the species barrier, it is crucial to investigate multi-stable models, and we propose one in Chapter 3.

2.2.2 Models of mammalian prions with structural diversity

With the perspective of aggregate structural diversity in mind, we review models that take this aspect into consideration and that suggest approaches to study it.

Micelles and the incompressible lag-time. The first model to explicitly include a supplementary step in the polymerization pathway was introduced for the study of *in*

vitro PrP^{Sc} amyloids [Alvarez-Martinez et al., 2011]. This study exhibited the existence of an incompressible lag-time for the formation of prion assemblies. The classical nucleation model suggests that the rate-limiting reaction of aggregate formation is the creation of a nucleus, a stochastic and rare event. This would account for the lag-time in the case of spontaneous accumulation, however according to this hypothesis the lag-time should be completely compressed if the reaction starts with existing aggregates, in other words if the reaction is seeded. The results from [Alvarez-Martinez et al., 2011] show that even a seeded polymerization reaction is limited by an incompressible lag-time. In addition to this result, electron microscopy imaging of *in vitro* samples showed the existence of different structures. In particular the early stage of PrP^{Sc} self-aggregation was marked by the appearance of spherical oligomers, later followed by long linear fibrils. This led to the formulation of a polymerization model which included an intermediate in the polymerization pathway, termed micelles [Hingant et al., 2014]. Those spherical intermediates were suggested to act as a facilitator for the formation of aggregates. PrP^{C} monomers first accumulate into these micelles and undergo a preliminary and reversible conformational change, before forming fibrillar aggregates with an irreversible conformational change. This model offered a reasonable explanation for the lag time measured in seeded *in vitro* polymerization reactions. The model itself is based on the use of multiple Becker-Döring schemes as building blocks. The idea of an intermediate in the polymerization pathway is also the starting point of our contribution in Chapter 3.

Structural transition during depolymerization of OvPrP oligomers. Previous studies have shown that Ovine PrP (OvPrP) spontaneously forms oligomers when incubated at temperatures higher than 45°C. Different types of oligomers are formed within a few minutes of incubation [Eghiaian et al., 2007], and further investigation of these subpopulations reveals that they are each composed of multiple constituting elements. An in-depth introduction to the behavior of OvPrP oligomers is given in Chapter 4, and we propose a kinetic model to explain the oscillatory and non-linear behavior observed during the depolymerization of these oligomers.

Monomeric conversion and oscillations. Another case where structural diversity was considered is the study of oscillations during human PrP^{Sc} depolymerization experiments [Doumic et al., 2019]. The difference with the results from [Armiento et al., 2017] lies in the assemblies subject to depolymerization. Here the depolymerization experiment is applied to PrP^{Sc} (pathological) fibrils of human PrP, and not oligomers of OvPrP. Real time monitoring of those experiments revealed transient oscillatory behavior. In order to explain those oscillations, a model was proposed by combining a Becker-Döring model with a monomeric intermediate. In a way this combines the concepts introduced by the hetero-dimer model as well as the Nucleated Polymerization model. A novel mechanism was also included, that of catalyzed depolymerization. In this model, the presence of normal PrP^{C} monomers catalyzes the depolymerization of aggregates into PrP^{C}. Those

features allowed the simulations to exhibit similar oscillatory behavior, providing a potential explanation for the experimental observations. The concepts of catalyzed depolymerization and monomeric intermediate are both used in our contribution in Chapter 4.

The different models introduced above are based on similar principles. They use classical models in combination with novel mechanisms, which are all forms of structural diversification. They were motivated by unaccounted for experimental observations. Note that they are all global models, and as such are limited if applied to the case of multiple strains. Our contributions fit in this context, by suggesting mechanisms to complete the classical models in order to explain biological results.

Chapter 3

The Template Assistance model

Chapter 3 is adapted from published work [Lemarre et al., 2018].

Given the open problems in the context of multiple strains for mammalian prions, as introduced in Chapter 2, we propose a novel model of prion kinetics. Our aim is to give insight into the problems of strain interaction, strain adaptation and the species barrier by including structural diversification of prion aggregates. Structural diversity is an important aspect of prion dynamics that was neglected until recently, and our results support the idea that it may be the key to understanding prion strains.

3.1 Introducing the Template Assistance model

3.1.1 A polymerization intermediate

Motivation and inspiration. We introduce a model adapted from the Nucleated Polymerization model, with an additional step in the polymerization pathway. Before mono-

mers are aggregated, they have to be converted into a species that we call subunits. Subunits act as a templating interface by directly interacting with the monomers, and their formation is autocatalytic but reversible. Subunits themselves are assembled into aggregates, following the dynamics of the Nucleated Polymerization model with a uniform fragmentation process. This formulation combines ideas from different studies and experimental results. It is reminiscent of the micelle model from [Hingant et al., 2014], and the formation of the subunits is inspired from the hetero-dimer model [Cohen et al., 1994] to which we add a non-linearity in a similar way as in [Laurent, 1998]. The fact that subunits are the species accumulated into aggregates means we are considering aggregates that have an inner structure, as described experimentally by [Igel-Egalon et al., 2017].

Model formulation. The model considers three different species through time $t \geq 0$, monomers with concentration $V(t)$, subunits with concentration $S(t)$ and aggregates with size distribution $u(x,t)$, where $x > 0$. The processes we consider are illustrated by Figure 3.1. The aggregates evolve following the Nucleated Polymerization model with a uniform fragmentation process of rate β and a nucleus size x_0, where the subunits S play the role of the monomers. Using moment closure we restrict ourselves to tracking the first two moments of the aggregate distribution $U(t)$ and $P(t)$. The formulation for this part of the model is then given by the last two equations of (1.8), substituting V by S. The polymerization rate is still denoted as τ and the degradation rate of aggregates as μ. The monomers are produced with speed λ and degraded with rate γ. The subunits are reverted to monomers with rate ω and they are degraded with rate δ. We add the reasonable assumption that subunits are degraded more slowly than monomers $\delta \leq \gamma$. All chemical constants are assumed to be positive. The subunits themselves interact with monomers in order to convert them, and they do so with a non-linear efficiency. To be precise, the conversion speed is $\rho V f(S)$ with f representing the concentration-dependent efficiency of subunits in converting monomers. Our choice of function is

$$f(S) = S\frac{S}{K+S}.$$

This means that the conversion speed is at most ρVS as given by a first order reaction scheme with rate ρ, but at low concentrations of subunits compared to the threshold value K, the kinetic order is of 2. This is known as a mixed-order reaction. A mechanistic justification for this choice would be the effect of a cooperative mechanism in subunit formation. Indeed the function we choose is a Michaelis-Menten scheme, which is common in enzyme reactions along with Hill functions [Weiss, 1997]. So far there is no experimental support for this mechanistic process, but there is no conflicting results either. The mathematical motivation for this choice becomes clear when realizing an equilibrium analysis for the model. The full ODE system we obtain is written as follows:

$$\begin{cases} \frac{dV}{dt} = \lambda - \gamma V - \rho V f(S) + \omega S, \\ \frac{dS}{dt} = \rho V f(S) - \omega S - \delta S - \tau S U + \beta x_0^2 U, \\ \frac{dU}{dt} = -\mu U + \beta P - 2\beta x_0 U, \\ \frac{dP}{dt} = \tau S U - \mu P - \beta x_0^2 U. \end{cases} \tag{3.1}$$

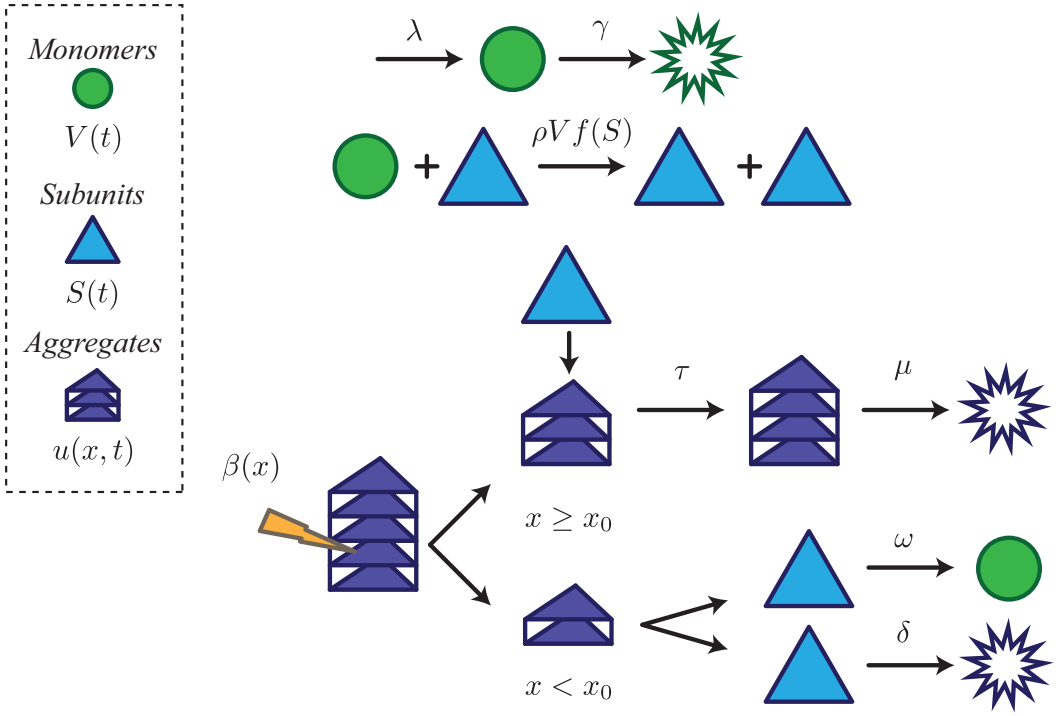

Figure 3.1 – **Illustration of the processes considered in the Template Assistance model.**

Similarly to the Nucleated Polymerization model, the System (3.1) has a unique positive solution. In particular, we prove the following Lemma.

Lemma 3.1. *When the parameters $\lambda, \gamma, \beta, \tau, \mu, x_0, \rho, \omega, \delta, K$ are all positive, the system (3.1) admits an unique positive solution for each initial condition taken in*

$$X = \{(V, S, U, P) \in \mathbb{R}^4 : V, S, U, P - x_0 U \geq 0\}.$$

Proof. It is simple to verify that X is positively invariant. Furthermore, for $t > 0$, $V(t) + S(t) + P(t)$ is bounded between 0 and $\frac{\lambda}{\epsilon} + (V(0) + S(0) + P(0))e^{-\epsilon t}$, with $\epsilon =$

$\min\{\gamma, \delta, \mu\}$. The proof is concluded as in [Prüss et al., 2006]. □

3.1.2 Equilibrium analysis

We now investigate the existence and, when possible, the linear stability of the steady-states of our system. Because it is useful in our analysis, we state here the Jacobian matrix of System (3.1) for clarity

$$\mathbf{J}(V,S,U,P) = \begin{pmatrix} -\gamma-\rho f(S) & \omega-\rho V f'(S) & 0 & 0 \\ \rho f(S) & \rho V f'(S)-\omega-\delta-\tau U & -\tau S+\beta x_0^2 & 0 \\ 0 & 0 & -\mu-2\beta x_0 & \beta \\ 0 & \tau U & \tau S-\beta x_0^2 & -\mu \end{pmatrix}.$$

The disease-free equilibrium. The first steady-state to consider is the the one with no misfolded proteins, meaning no subunits and no aggregates. The following proposition is verified.

Proposition 3.1. *The disease-free equilibrium exists for any choice of positive parameters, and is given by*

$$(V,S,U,P) = \left(\frac{\lambda}{\gamma}, 0, 0, 0\right).$$

It is locally stable if and only if

$$\frac{\lambda}{\gamma} f'(0) < \frac{\omega+\delta}{\rho}.$$

In particular when $f'(0) = 0$, as with the choice $f(S) = S^2/(K+S)$, the disease-free equilibrium is locally stable for any choice of positive parameters.

Proof. A straightforward calculation yields the eigenvalues of the Jacobian matrix at this point $\{-\gamma, -\mu-\beta x_0, -\mu-\beta x_0, \frac{\lambda}{\gamma} f'(0) - \omega - \delta\}$. For positive parameters, the local stability depends only on the last one, and it is negative when the condition expressed above is verified. □

The local stability of the disease-free equilibrium is the novel feature, as compared to the classical Nucleated Polymerization model, that will enable co-stability of different equilibria. Any other function verifying $f'(0) = 0$ would also yield the same property, but our choice was to introduce as few parameters as possible. On the contrary, a linear templating rate would not provide co-stability, as explained at the end of this section.

The subunits-only equilibria. A second type of steady-state is possible, when subunits are present but no aggregates.

Proposition 3.2. *There exists at most two subunits-only equilibria, and they are given by*

$$(V, S, U, P) = \left(\frac{\lambda}{\gamma} - \frac{\delta}{\gamma}S_{\pm}, S_{\pm}, 0, 0\right)$$

with

$$S_{\pm} = \frac{1}{2}\left(\frac{\lambda}{\delta} - \frac{\omega+\delta}{\rho}\frac{\gamma}{\delta}\right) \pm \sqrt{\left(\frac{1}{2}\left(\frac{\lambda}{\delta} - \frac{\omega+\delta}{\rho}\frac{\gamma}{\delta}\right)\right)^2 - \frac{\omega+\delta}{\rho}\frac{\gamma}{\delta}K}.$$

These equilibria are feasible (real positive values for V and S) if and only if

$$\frac{\lambda}{\gamma} > \frac{\omega+\delta}{\rho} + 2\frac{\delta}{\gamma}\sqrt{\frac{\omega+\delta}{\rho}\frac{\gamma}{\delta}K}.$$

The equilibrium associated with S_- is always locally unstable. The equilibrium associated with the higher value is locally stable if and only if

$$S_+ < \frac{(\mu+\beta x_0)^2}{\beta\tau}.$$

Proof. If we impose $U = 0$ and $P = 0$, the remaining two equations on V and S lead to

$$\begin{aligned} V =& \frac{\lambda}{\gamma} - \frac{\delta}{\gamma}S, \\ \rho\big(\frac{\lambda}{\gamma} - \frac{\delta}{\gamma}S\big)f(S) =& (\omega+\delta)S. \end{aligned}$$

With the choice $f(S) = S^2/(K+S)$, the equation on S simplifies to $S^2 + \left(\frac{\omega+\delta}{\rho}\frac{\gamma}{\delta} - \frac{\lambda}{\delta}\right)S + \frac{\omega+\delta}{\rho}\frac{\gamma}{\delta}K = 0$. The solutions are real if and only if $\left(\frac{1}{2}\left(\frac{\lambda}{\delta} - \frac{\omega+\delta}{\rho}\frac{\gamma}{\delta}\right)\right)^2 > \frac{\omega+\delta}{\rho}\frac{\gamma}{\delta}K$, and they are positive if and only if $\frac{\lambda}{\delta} > \frac{\omega+\delta}{\rho}\frac{\gamma}{\delta}$. Combining these two conditions gives the feasibility inequality as stated in the proposition. The linear stability results are a consequence of the slightly more general Lemma 3.2 below, noticing that $f(S) = S^2/(K+S)$ verifies the assumptions of the Lemma. □

Lemma 3.2. *Suppose the function $f : \mathbb{R}_+ \to \mathbb{R}_+$ verifies the following assumptions*

- *f is continuous and positive-valued on $\mathbb{R}_+^*$,*
- *$f(0) = 0$,*
- *$f'(0) = 0$,*
- *f is monotonically increasing,*
- *f admits at most one inflection point.*

Then the system admits at most two subunits-only equilibria

$$(V, S, U, P) = \left(\frac{\lambda}{\gamma} - \frac{\delta}{\gamma}S_{1,2}, S_{1,2}, 0, 0\right).$$

Moreover, if the two equilibria are feasible ($0 < S_{1,2} < \frac{\lambda}{\delta}$) and are ordered as $S_1 \leq S_2$, then the one associated to S_1 is unstable and the one associated to S_2 is locally stable if and only if $S_2 < \frac{(\mu+\beta x_0)^2}{\beta\tau}$.

Proof. We look for feasible steady-state solutions with $U = P = 0$ distinct from the disease-free equilibrium, meaning $V \geq 0$ and $S > 0$. The first equation of the system gives a linear relation $V = \frac{\lambda}{\gamma} - \frac{\delta}{\gamma}S$. The equation on S rewrites as $H(S) = (\omega + \delta)S$, with

$$H(S) = \rho\big(\frac{\lambda}{\gamma} - \frac{\delta}{\gamma}S\big)f(S).$$

Finding feasible subunits-only equilibria comes down to solving this equation on $]0, \frac{\lambda}{\delta}]$, as illustrated by Figure 3.2. Note that $H'(S) = \rho\big(\frac{\lambda}{\gamma} - \frac{\delta}{\gamma}S\big)f'(S) - \frac{\delta}{\gamma}f(S)$. The hypotheses on f imply $H(0) = 0$, $H'(0) = 0$, $H(\frac{\lambda}{\delta}) = 0$, $H'(\frac{\lambda}{\delta}) < 0$, and $H(S) > 0$ for S in $]0, \frac{\lambda}{\delta}[$. This means that H has a maximum value on $]0, \frac{\lambda}{\delta}[$, and since f is monotonically increasing, this maximum is unique. Furthermore, H' also admits a maximum value on $]0, \frac{\lambda}{\delta}[$ and since f has at most one inflection point, this maximum is also unique. This means that, geometrically the curves $H(S)$ and $(\omega + \delta)S$ may interesect at most twice, once with H crossing from under the line, and once with H crossing from above the line. To be precise, the equation $H(S) = (\omega + \delta)S$ admits two solutions as soon as there exists $\bar{S}$ such that $H'(\bar{S}) = \omega + \delta$ and $H(\bar{S}) > (\omega + \delta)\bar{S}$. Without giving an analytical expression for f, this condition is not tractable any further.

However, the stability of the equilibria, when they exist, is tractable. Indeed, if the two solutions are numbered as $S_1 < S_2$, then S_1 is necessarily the solution corresponding to H crossing the line from under since H starts with a horizontal tangent in 0, as is clearly illustrated by Figure 3.2. In other words, we have $H'(S_1) > (\omega + \delta)$. Similarly we have $H'(S_2) < (\omega + \delta)$. Writing the Jacobian matrix at one of these two points yields two pairs of eigenvalues. The first pair is given by the roots of the polynomial

$$\chi^2 + \left(\omega + \delta + \rho f(S_{1,2}) - \Big(\frac{\lambda}{\gamma} - \frac{\delta}{\gamma}S_{1,2}\Big)f'(S_{1,2}) + \gamma\right)\chi \\ - \gamma\left(\rho(\frac{\lambda}{\gamma} - \frac{\delta}{\gamma}S_{1,2})f'(S_{1,2}) - \rho\frac{\delta}{\gamma}f(S) - \omega - \delta\right),$$

which is also written as

$$\chi^2 + \Big(\omega + \delta - H'(S_{1,2}) + \gamma + \rho f(S_{1,2})\big(1 - \frac{\delta}{\gamma}\big)\Big)\chi - \gamma\big(H'(S_{1,2}) - \omega - \delta\big).$$

We immediately conclude that S_1 is locally unstable because $H'(S_1) > \omega + \delta$ and so one eigenvalue always has a realpositive part. Since $H'(S_2) < \omega + \delta$, and with the assumption that $\delta \leq \gamma$ (added when the parameters were introduced), these two eigenvalues have negative real parts for S_2. In order to conclude on its stability we need to investigate the other two eigenvalues.

The second pair of eigenvalues of the Jacobian matrix at $S_{1,2}$ is given by $\Big(-\mu - \beta x_0 \pm \sqrt{\tau\beta S_{1,2}}\Big)$. Consequently they are negative as soon as $S_{1,2} < \frac{(\mu+\beta x_0)^2}{\beta\tau}$ and this concludes the proof. □

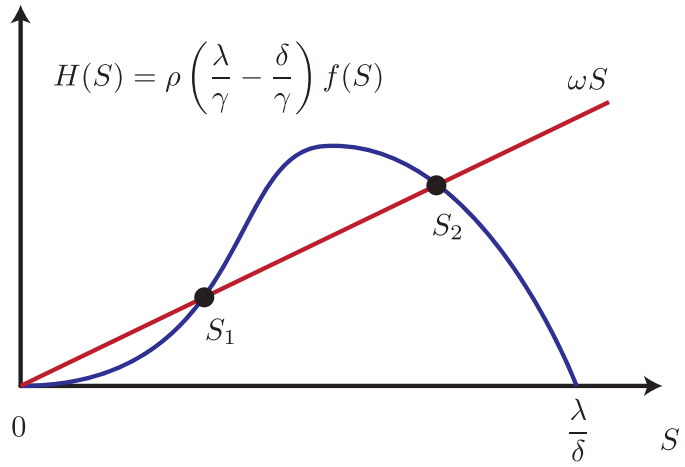

Figure 3.2 – **Geometric illustration of the subunits-only equilibria conditions.** The conditions for existence of the two subunits-only equilibria as presented in Lemma 3.2 are illustrated. The shape of the function H depends on the hypotheses on f which are listed in the Lemma.

This result shows that the two subunits-only equilibria emerge through a saddle-node bifurcation, and that only the one associated with a higher subunit concentration might be stable. This behavior is not strictly reliant on the choice of function f, and we propose a minimal set of assumptions it must verify in Lemma 3.2. These assumptions are reasonable considering $f(S)$ represents the chemical activity of the subunits.

The endemic equilibrium. Finally, there exists a steady-state solution where all species are present.

Proposition 3.3. *The endemic steady-state* (V^*, S^*, U^*, P^*) *is defined by the following relations*

$$\begin{aligned} S^* =& \frac{(\mu+\beta x_0)^2}{\beta\tau}, \\ V^* =& \frac{\lambda+\omega S^*}{\gamma+\rho f(S^*)}, \\ U^* =& \frac{1}{\tau S^* - \beta x_0^2}(\rho V^* f(S^*) - \omega S^* - \delta S^*), \\ P^* =& \frac{\mu+2\beta x_0}{\beta} U^*. \end{aligned}$$

This equilibrium is feasible (positive values) when

$$\rho\Big(\frac{\lambda}{\gamma} - \frac{\delta}{\gamma}S^*\Big) f(S^*) > (\omega+\delta)S^*.$$

Proof. The feasibility mainly relies on $U^* > 0$, which with the value of V^* reduces to the condition expressed above (noticing that $\tau S^* - \beta x_0^2 = \mu(\mu+2\beta x_0)/\beta > 0$). □

Recalling the conditions of existence of the two subunits-only equilibria, we note that the endemic steady-state exists when the associated subunit density S^* is comprised between the two subunits-only values $S_\pm$ (which implies that these solutions exist in the first place). These values are indeed the solutions to the equality associated with the condition expressed in Proposition 3.3. The local stability of the endemic equilibrium is not tractable analytically, and we investigate it numerically through a bifurcation analysis in the next section.

Remark. *Although we cannot show analytically that the condition* $f'(0) = 0$ *is necessary for co-stability of different equilibria, we can show that when* f *is linear co-stability is not possible. Indeed, if* $f(S) = S$*, which is equivalent to* $K = 0$ *in all the developments above, there is only one subunits-only equilibrium associated with the subunit density* $\hat{S} = \frac{\lambda}{\delta} - \frac{\omega+\delta}{\rho}\frac{\gamma}{\delta}$*. The stability condition for the disease-free equilibrium is reduced to* $\frac{\lambda}{\gamma} < \frac{\omega+\delta}{\rho}$ *or equivalently* $\hat{S} < 0$*, which shows that these two equilibria cannot be both feasible and stable at the same time. The subunits-only equilibrium is in turn stable as long as* $\hat{S} < \frac{(\mu+\beta x_0)^2}{\beta\tau} = S^*$ *(with the notation of Proposition 3.3. However, the feasibility condition of the endemic equilibrium is now reduced to* $V^* > \frac{\omega+\delta}{\rho}$ *(*V^* *defined in Proposition 3.3) or equivalently* $\frac{\lambda}{\delta} - \frac{\omega+\delta}{\rho}\frac{\gamma}{\delta} = \hat{S} > S^*$ *after simplification. This proves that the subunits-only equilibrium and the endemic equilibrium cannot be both feasible and stable at the same time. Overall, when* f *is linear there are only three possible equilibria and they appear through a series of transcritical bifurcations, thus there can be no co-stability.*

3.1.3 Numerical bifurcation analysis

As shown in Subsection 3.1.2, the subunits-only steady-states appear through a saddle node bifurcation (Proposition 3.2). The endemic steady-state appears when the associated subunit concentration S^* crosses one of the two branches S_+ or S_- (Proposition 3.3). If it appears through the higher branch, the high subunit only steady-state S_+ is stable at first, and then becomes unstable. If the endemic steady-state instead appears through the lower branch, none of the subunit only steady-states will be stable (see conditions in Subsection 3.1.2). These two scenarios are illustrated in Figure 3.3. As the monomer source rate λ increases, we can see the saddle-node bifurcation followed by the emergence of the endemic steady-state. This is a numerical illustration of the results proved in the previous section.

When the endemic steady-state exists, it is either locally stable or unstable. Numerical exploration shows that it undergoes a Hopf bifurcation. This is illustrated with a numerical two-parameter bifurcation analysis in Figure 3.5. We show dependence on two key parameters: the monomer synthesis rate λ and the polymerization rate τ. The bifurcation analysis is based on the properties of the Jacobian matrix at the endemic steady-state, and we characterize the presence of a Hopf bifurcation as when one eigenvalue crosses the imaginary axis with a non-zero imaginary part. Figure 3.5 illustrates regions of qualitatively distinct dynamics and the boundaries between these regions correspond to different bifurcation events. The endemic steady-state is only stable in Region 4, and the Hopf bifurcation occurs at the transition between Regions 4 and 5. In Region 5, only the disease-free equilibrium is locally stable. The solutions can either be attracted by this equilibrium or undergo stable oscillations. Figure 3.4 illustrates this behavior in a case where the endemic equilibrium is unstable, but a stable cycle orbits around it (with oscillations at multiple time scales). The exact nature of these oscillations is not known analytically, but the most important qualitative result here is that by crossing this Hopf bifurcation an aggregate population may be destabilized. The fact that oscillations have been observed experimentally is another reason for interest in that behavior, see for instance [Doumic et al., 2019]. Overall, the complexities of bifurcations in our model demonstrate that the addition of the polymerization intermediate with a non-linear autocatalysis enriches the model with a wide variety of behaviors.

3.2 Coexistence of strains and non-trivial interactions

3.2.1 Two-strain case and equilibrium analysis

As we have emphasized throughout, our primary motivation in developing the Template Assistance model is to explore the system when multiple prion strains are present. We generalize our model to two strains, as illustrated in Figure 3.6. The corresponding generalization to System (3.1) is the following:

Table 3.1 – **Parameter definitions and values used for numerical simulations of the Template Assistance model** (unless specified otherwise). The values are chosen arbitrarily, with magnitudes consistent with values from [Masel et al., 1999], where time is expressed in *days*. The aggregate-associated quantities are in fibril number per volume unit

Parameter	Definition	Value	
λ	Monomer source rate	1500	
γ	Monomer degradation rate	5	
		Strain 1	Strain 2
ρ	Conversion rate of normal monomers to subunits	5	1
ω	Reconversion rate of subunits	1	1
K	Threshold concentration for the conversion kinetics	500	100
δ	Degradation of subunits	2	2
τ	Polymerization rate of subunits	0.1	0.2
β	Fragmentation rate of polymers	0.0003	0.1
μ	Degradation rate of polymers	0.04	0.04
x_0	Nucleus size	6	6

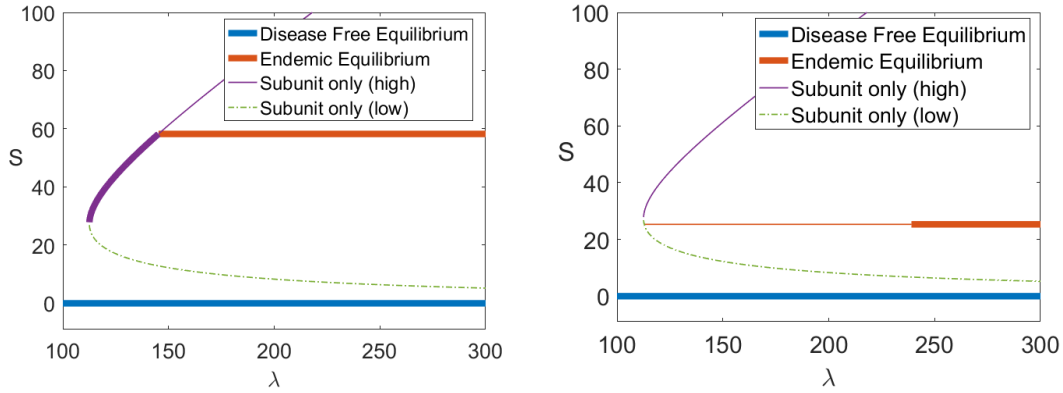

(a) $\tau = 0.1$ (b) $\tau = 0.23$

Figure 3.3 – **Bifurcation diagram obtained for Template Assistance model.** The steady-state subunit density S is tracked when the monomer source, λ, varies for two values the polymerization rate τ. The other parameters are set as in Table 3.1 (Strain 1). The four different equilibria are depicted (disease-free equilibrium, endemic equilibrium, higher subunit only equilibrium (S_+), lower subunit only equilibrium (S_-)). A thin line indicates an unstable equilibrium, whereas a bold line indicates a locally stable equilibrium.

$$\begin{cases} \dfrac{dV}{dt} = \lambda - \gamma V - \rho_1 V f_1(S_1) + \omega_1 S_1 - \rho_2 V f_2(S_2) + \omega_2 S_2, \\ \dfrac{dS_i}{dt} = \rho_i V f_i(S_i) - \omega_i S_i - \delta_i S_i - \tau_i S_i U_i + \beta_i x_i^2 U_i, \quad i = 1, 2, \\ \dfrac{dU_i}{dt} = \beta_i P_i - \mu_i U_i - 2\beta_i x_i U_i, \quad i = 1, 2, \\ \dfrac{dP_i}{dt} = \tau_i S_i U_i - \mu_i P_i - \beta_i x_i^2 U_i, \quad i = 1, 2. \end{cases} \tag{3.2}$$

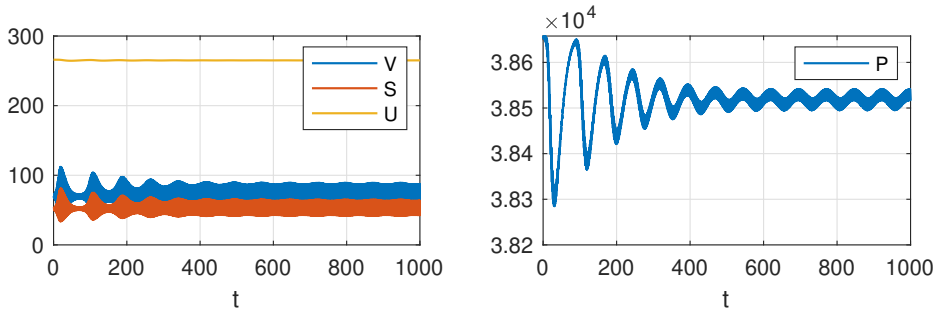

(a) Slow oscillations

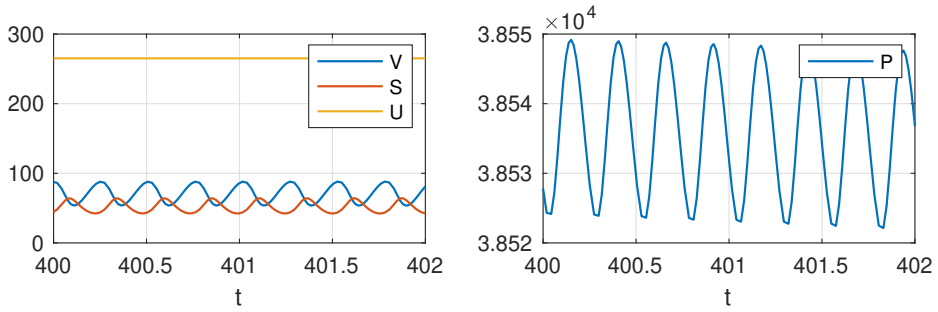

(b) Fast oscillations

Figure 3.4 – **Sustained oscillations of the Template Assistance model.** Simulations are shown for $\tau = 0.1125$ and $\lambda = 2000$, the rest of the parameters are set as in Table 6.1. The initial condition is the endemic steady-state (which is unstable in this case), disturbed by a slight increase in the subunit concentration S. The oscillations are sustained on different time scales, as emphasized by the different horizontal axis in both panels.

The interaction functions, f_i, are the same as in System (3.1), but now with a strain specific value of K_i: $f_i(S) = S^2/(K_i + S)$.

Coexistence is possible analytically. The behavior of this System (3.2) is dramatically different from that of the multi-strain Nucleated Polymerization model (System (2.1) presented in Subsection 2.2.1). Our new system allows for coexistence of prion strains. Each strain may exist in the same conditions as single strains do, see Subsection 3.1.2. Furthermore, two strains may coexist under different configurations: both as subunits only, or one endemic and the other as subunits only (we will refer to this case as semi-endemic) or both endemic (with aggregate populations). We note that subunit only coexistence is impossible for general values of the parameters, with the same argument that was used to rule out coexistence equilibria in the multi-strain Nucleated Polymerization model in Subsection 2.2.1. Finally, numerical results suggest that semi-endemic coexistence is very unlikely to occur.

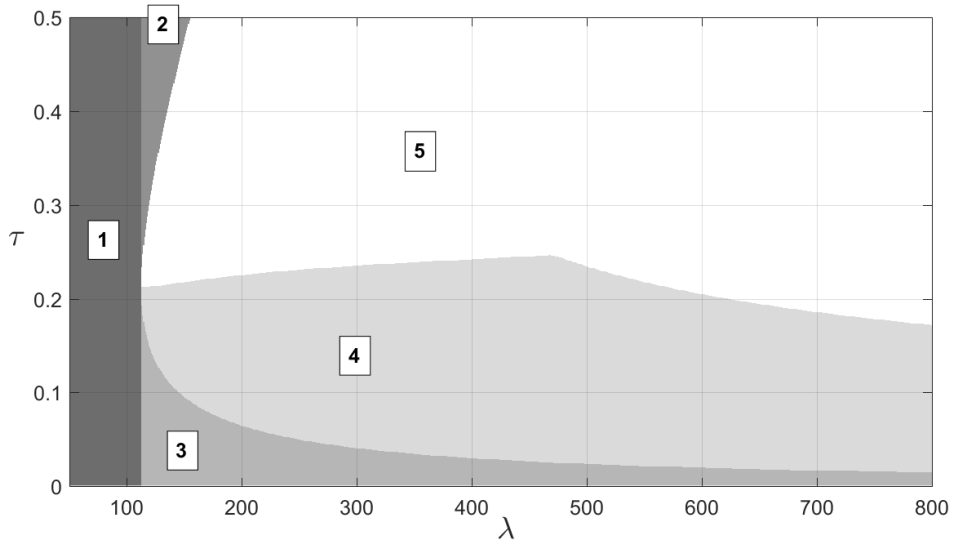

Figure 3.5 – **Two-parameter bifurcation diagram for the Template Assistance model.** The diagram is obtained by varying the monomer source rate λ and the polymerization rate τ, when the other parameters are described in Table 3.1 (Strain 1). The vertical line delimits the apparition of the subunit only equilibria, left of that line (**Region 1**) only the disease-free equilibrium exists and it is then globally stable (not proved). The branches delimit the existence of the endemic equilibrium. In **Region 2**, the subunit only equilibria exist but neither is stable. In **Region 3**, the subunit only equilibria exist and the higher one (S_+) is locally stable. In-between the branches, the endemic steady-state exists, but it is only locally stable in **Region 4**. In **Region 5**, the endemic steady-state is unstable. The boundary between **Regions 4** and **5** corresponds to a Hopf bifurcation.

The coexistence steady-state for two strains is given by

$$\begin{aligned}
S_i^* =& \frac{(\mu_i + \beta_i x_i)^2}{\beta_i \tau_i} \text{ for i =1,2,} \\
V^* =& \frac{\lambda + \omega_1 S_1^* + \omega_2 S_2^*}{\gamma + \rho_1 f_1(S_1^*) + \rho_2 f_2(S_2^*)}, \\
U_i^* =& \frac{1}{\tau_i S_i^* - \beta_i x_i^2} (\rho_i V^* f_i(S_i^*) - \omega_i S_i^* - \delta_i S_i^*) \text{ for } i = 1, 2, \\
P_i^* =& \frac{\mu_i + 2\beta_i x_i}{\beta_i} U_i^* \text{ for i =1,2.}
\end{aligned}$$

Notice $\tau_i S_i^* = \mu_i(\mu_i + 2\beta_i x_i)/\beta_i > 0$. Similarly to the single-strain case, this equilibrium

exists when all values of the variables are positive yielding the conditions

$$\rho_i V^* f_i(S_i^*) > (\omega_i + \delta_i) S_i^* \text{ for i} = 1, 2.$$

While we were unable to simplify these conditions, they are easily verified for a given combination of parameters. In particular, we note that for any choice of kinetic rates for prion strains $(\beta_i, \tau_i, \omega_i, \rho_i)$, the coexistence steady-state can always be made to exist by increasing the monomer source rate λ enough to satisfy the above conditions (because increasing λ increases V^* without changing the values of S_1^* and S_2^*).

Multiple steady-states are co-stable. The second improvement of our System (3.2) over the multi-strain Nucleated Polymerization is that it allows for co-stability. As is the case with a single strain, the disease-free equilibrium is always locally stable (easily proved with the Jacobian matrix). Again as in the single-strain case, the co-stability of different types of equilibria (single-strain steady-states and coexistence steady-states) could not be proved analytically but is be observed through numerical exploration. As such, the outcome depends on the initial conditions and a numerical investigation gives some insight into this behavior.

3.2.2 Numerical results

In this section we provide a detailed numerical study of the behavior of the Template Assistance model we developed in the previous section. We first verify that the behavior in the single strain case remains similar to the original Nucleated Polymerization model. We next study the dependency on initial condition when multiple steady-states are locally stable by numerically investigating the basins of attraction. Notice that in the different time evolution figures we produce, the evolution of P, the first moment of the aggregates distribution *i.e.* the total mass or number of aggregated monomers, is not displayed because it is very similar to the evolution of U, the zero-th moment of the distribution *i.e.* the total number of aggregates. However, P is on a different scale of values than the other variables so for the sake clarity we do not show it.

The dynamics of the Nucleated Polymerization model are conserved. Because of its broad acceptance, it is crucial that the qualitative behavior of the Nucleated Polymerization model be maintained after modification. A generic study case is presented in Figure 3.7, comparing the dynamics of the classical model with our model. One can see the overall dynamics of aggregate formation are qualitatively and quantitatively very similar for long times. Even though it is not shown, the evolution of $P(t)$ also coincides with the one observed in the Nucleated Polymerization model for long times. The behavior during early times is dramatically different, because a new species is introduced. Our focus here is not on transient dynamics because we lack the data to study them, but it could be a potential way to discriminate between different models. This shows that our model brings new possibilities without eliminating previously supported behavior [Greer

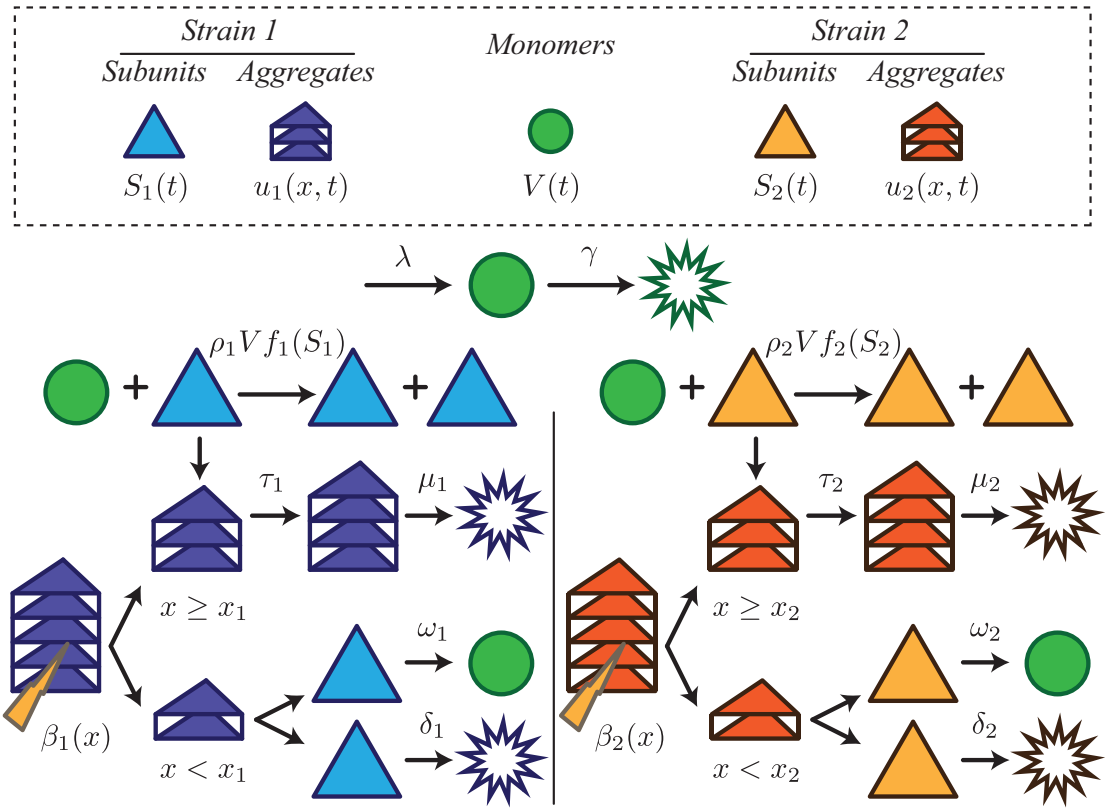

Figure 3.6 – **Template assistance mechanism illustrated with two different strains.** The strains compete for normal monomers through the interaction with subunits (with rates ρ_1 and ρ_2). The dynamics of each strain taken individually are then described as in Figure 3.7.

et al., 2006, Prüss et al., 2006, Masel et al., 1999], especially on aggregate formation, size and numbers.

The Template Assistance model exhibits co-stability. Even though the Nucleated Polymerization dynamics can be reproduced, our model offers a new variety of behaviors even for the single strain case. Because the disease-free equilibrium remains locally stable, our system exhibits dependency on the initial conditions. Figure 3.8 represents the basins of attraction of the endemic steady-state and the disease-free steady-state, for the case studied in Figure 3.7. This helps to visualize the complexity and the diversity of behaviors allowed by our model. A biological interpretation for the shape of the basins plotted in Figure 3.8 would be that an outbreak of prion propagation is possible only by having a specific initial mix of subunits and aggregates. In particular, starting off with too many aggregates ($U(0)$ high) would prevent the subunits pool from successfully building up.

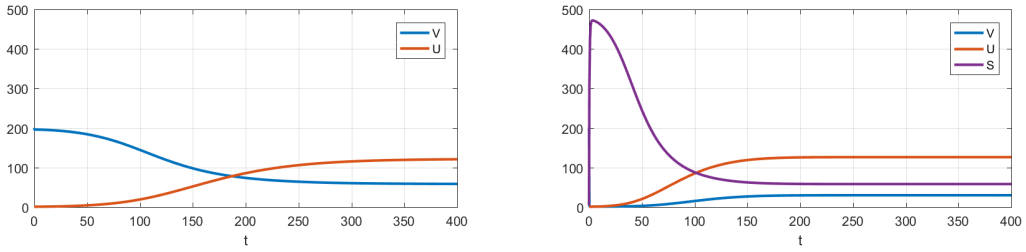

Figure 3.7 – **Numerical simulation using the Nucleated Polymerization model (a) and the Template Assistance model (b).** The parameters used are described in Table 3.1 (Strain 1). The initial condition is given by $V(0) = \frac{\lambda}{\gamma} = 200, U(0) = 0.1, P(0) = (2x_0 + \frac{\mu}{\beta})U(0), S(0) = 0.2$.

We want to stress out that the important aspect of Figure 3.8 is the shape of the basins, the precise values for the borders are irrelevant due to the arbitrary choice in parameters. Furthermore, this shape is subject to change when modifying the parameters, although so far we have no way of predicting these changes analytically. A numerical investigation could be undertaken, but in order to make biologically relevant predictions we require experimental observations or experimentally derived biochemical parameter values (see Subsection 3.3.2).

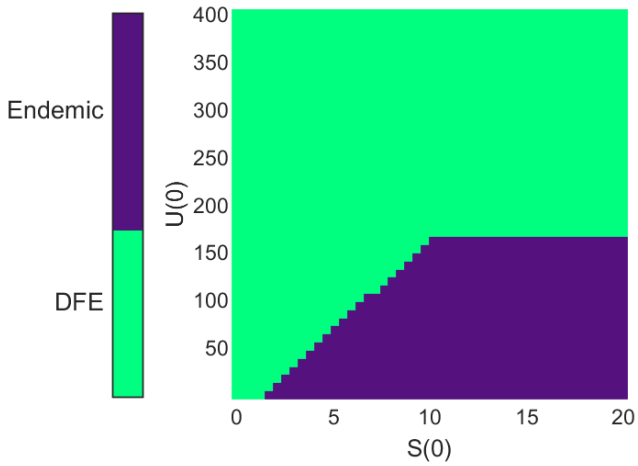

Figure 3.8 – **Representation of the basins of attraction of the Template Assistance model.** The basins of the endemic steady-state (dark color) and the disease-free steady-state (lighter color) are represented, according to the initial condition. The horizontal axis represents the initial number of subunits, and the vertical axis represents the initial number of aggregates. The parameters used are these of Strain 1 in Table 3.1, the initial value for V is set to λ/γ (disease-free value), and the initial value for P is set to $(2x_0 + \mu/\beta)U(0)$ (steady-state mean size).

The two-strain case exhibits coexistence and co-stability. To support the analytical results on strain coexistence (Subsection 2.1.1) and give numerical evidence of co-stability we show some simulations with two strains. Figure 3.9 illustrates the different possible outcomes, depending on the initial conditions. The set of parameters used (see Table 3.1) allows for four different equilibria to be co-stable (disease-free equilibrium, two single strain equilibria and coexistence equilibrium). Depending on the initial mass of each strain, the outcome can be the takeover of one strain or the stable coexistence of both, or the extinction of both. The shapes of the different basins of attraction are complex and non-intuitive. Indeed, in some cases increasing the initial amount of one prion strain can lead to its extinction (see the right-hand side of Figure 3.9). Although such behavior seems highly complex, we note that coexistence and co-stability are phenomena supported by experimental studies on mammalian prions [Langenfeld et al., 2016].

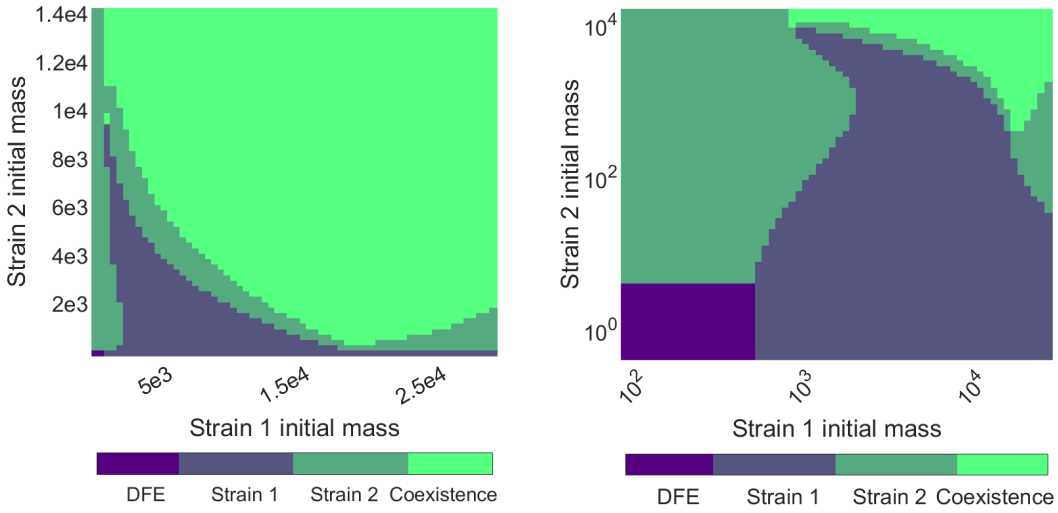

(a) Linear scale

(b) Logarithmic scale

Figure 3.9 – **Representation of the basins of attraction of the different equilibria in the two-strain case, in linear scale and logarithmic scale.** The parameters used are described in Table 3.1. Each strain is initialized with its steady state proportions (see Subsection 3.1.2) and diluted with a specific rate (between 1 and 1.10^{-5}), and V is initialized to the disease-free value λ/γ. The axes represent the initial mass of each strain, *i.e.* the initial value of $P + S$ for each strain (Strain 1 on the horizontal axis, Strain 2 on the vertical axis). The colors represent the outcome of the simulation (with the colorbar above), one strain only or the two strains stably coexisting. Notice that the disease-free equilibrium is observed only in the bottom left corner.

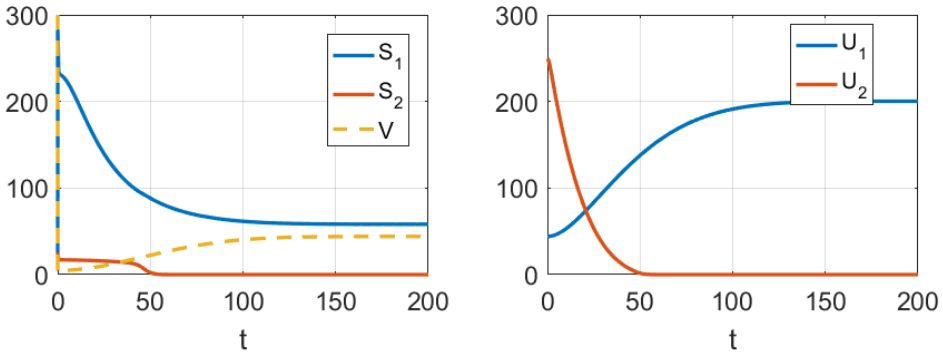

(a) $(S_1(0), U_1(0), P_1(0)) = (12.8, 44.0, 6398)$ and $(S_2(0), U_2(0), P_2(0)) = (4.5, 249.5, 3095)$

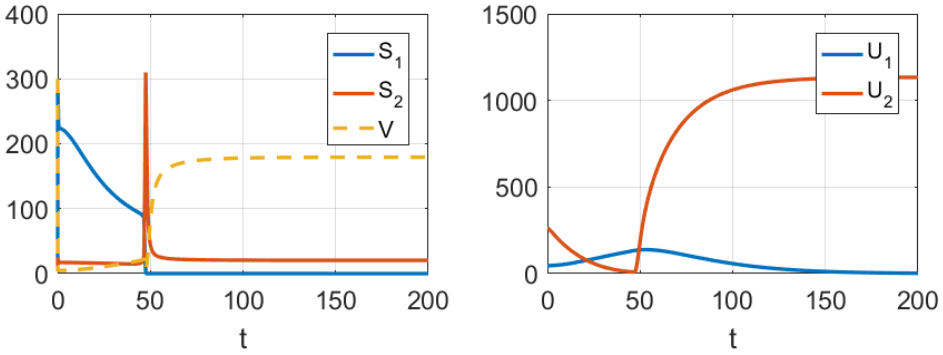

(b) $(S_1(0), U_1(0), P_1(0)) = (13.4, 46.0, 6689)$ and $(S_2(0), U_2(0), P_2(0)) = (4.7, 260.9, 3235)$

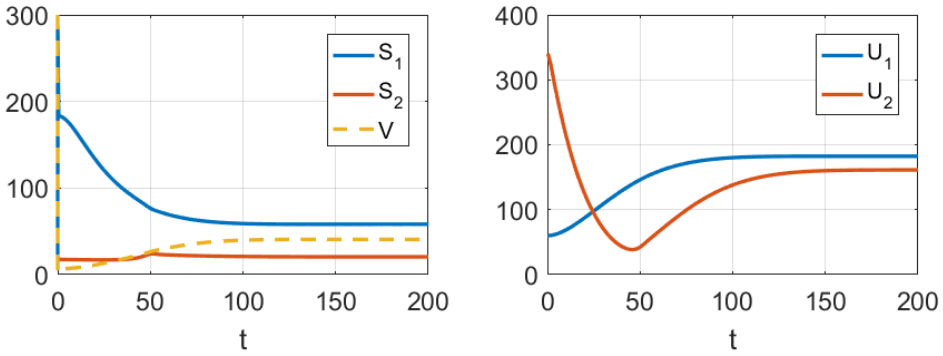

(c) $(S_1(0), U_1(0), P_1(0)) = (17.5, 60.0, 8725)$ and $(S_2(0), U_2(0), P_2(0)) = (6.1, 340.3, 4220)$

Figure 3.10 – **Illustrations of typical cases from the diagram shown in Figure 3.9,** representing the time evolution of the two strains (blue line is Strain 1, orange line is Strain 2). The parameters used are shown in Table 3.1. In each case, V is initialized to the disease-free steady-state λ/γ, and the strains are initialized with the specified conditions. The top panel (a) shows takeover of Strain 1, the middle panel (b) shows takeover of Strain 2, whereas the bottom panel (c) shows asymptotic coexistence of both strains.

3.3 Discussion and perspectives

In this work, we have developed a novel model of prion aggregate dynamics which, in contrast to the traditional model in the field, is capable of supporting recent biological observations in mammalian prions systems [Le Dur et al., 2017, Langenfeld et al., 2016]. While a lack of detailed experimental findings have made precise quantitative comparisons impossible, the qualitative analysis of our model provides insight into a number open problems of prion phenomena as we discuss below.

3.3.1 Insight into open problems in prion biology

The interplay between structural diversity and pathogenesis. The model we introduce here suggests one implementation of structural diversity into the classical modeling framework. In particular, the idea is to add an intermediate step in the polymerization pathway, between normal monomers and prion aggregates. This allows us to separate templating (conformational change of monomers) and polymerization (formation of aggregates). Furthermore, we emphasize on the importance of adding a non-linearity in the templating process, since it is crucial in order to observe co-stability and to have dependency on the initial conditions. The additional species in the model inevitably increases the number of parameters, complicates the analysis and confuses the interpretation. However it suggests clues to explain some perplexing results, such as the decorrelation between measured aggregation and infectivity. Indeed experimental studies have reported that the infectivity, the potential to cause disease upon transmission to a healthy host, rises before any aggregated species is detected in the organism [Rubenstein et al., 1991, Mays et al., 2015]. This is referred to as the "infectivity plateau", and it is most likely related to the lag-time that limits *in vitro* polymerization experiments. This lag-time was evidenced and studied with the introduction of micelles [Hingant et al., 2014], a model very similar to ours. Overall this suggests that structural diversity has a strong impact on infectivity and pathogenesis. This is also supported by recent cross-species studies [Igel-Egalon et al., 2019b], where reducing the structural diversity of a strain makes it less apt at crossing the species barrier. Thus the question arises: What is the infectious agent? Since there are multiple aggregate species co-evolving, which ones are driving the propagation and the replication of the prions? Our model supports the idea that the driving species would be the smaller, soluble and amorphous species, not detectable as aggregates.

Structural diversity enriches prion strain interactions. As our model illustrates, introducing diversity in the prion populations is a way to allow for different strains to interact in intricate ways. In particular, they can coexist in robust settings (for wide parameter ranges), which is a result supported by many observations (see Subsection 2.1.1). They can also interact in unpredictable ways (as suggested by the puzzling shapes of the basins of attraction in Figure 3.8 and Figure 3.9). This qualitatively concurs with

experimental results of co-infection studies and cross-species transmission (see Subsection 2.1.1). Overall this emphasizes how important the concept of structural diversity is in understanding the phenomenon of strains. Many questions remain, because we do not know the exact structural composition of different strains, the dynamics of their formation and their interactions.

Co-stability and the influence of the inoculum. The second feature that our model introduces is co-stability, through the addition of a non-linearity in the templating of monomers. This allows the asymptotic outcome to depend on the initial conditions, which is crucial in order to reproduce experimental results (even qualitatively). This relates to co-infection studies, dependency on the monomer expression level, cross-species transmission, strain adaptation, among other results (see Section 2.1). It concurs with the idea that structural diversity plays critical a role at the very early stages of the infection [Igel-Egalon et al., 2019b], and non-linearities come into play at this point. It is a radically different approach from the one classically used in modeling prion diseases. The usual idea is to use epidemiology models, but those models are (for the most part) global models, for which the asymptotic outcome only depends on a function of the parameters (the basic reproduction rate) and a linearization around the disease-free equilibrium. Our results emphasize the importance in turning to different approaches, by including non-linearities and co-stability. So far we have no mechanistic justification for the model we proposed, but we think that, from a mathematical standpoint, it includes the right elements.

3.3.2 Challenges and limitations

In order to compare the numerical results we observe with *in vivo* behavior, we must be able to infer realistic values for the model parameters. Few studies have investigated parameter inference before [Masel et al., 1999, Derdowski et al., 2010], and then only in the case of a single strain. Refining parameter values requires detailed experimental studies, when *in vivo* experiments are long and costly.

However, before we can hope to fit parameters, it must be clear how to link biological observable markers (i.e., prion phenotypes) with quantities in our mathematical model. What biologists observe and quantify are global properties related to the disease (incubation time, deposition pattern, molecular density distribution, migration patterns, see [Morales, 2017] for a detailed description), but it is not clear how these properties are linked to the bio-chemical kinetics of aggregate formation. Mounting evidence suggests that phenotypes (disease properties) are not necessarily linked to prion strains (conformational states of the protein) in a one-to-one relation. Some phenotypes could potentially be composed of a mixture of different strains, and in some cases, strains are propagated "silently" (not influencing the phenotype) [Le Dur et al., 2017]. This makes it even more complicated to determine each strain's characteristics.

By introducing a novel species (prion subunits) we have contributed to complicate the

question of what is the **infectious agent** of prion phenotypes. It is not clear what causes disease and what causes the onset of symptoms. Some insight from our primary study would be that infectivity might be optimal when the inoculum consists of a specific mix of aggregates and subunits. Disturb these proportions and the propagation fails. Our work also suggests that these proportions are strain-specific, and dependent on the environment or on the presence of other strains.

Finally, we emphasized the importance to introduce a mechanism to account for the non-linearity in the templating rate of subunits, yet we have no justification or evidence for such a mechanism *in vitro* or *in vivo*. Understanding the dynamics of prion assemblies at the very early stages of the disease, before detection of any aggregated species is detectable, is crucial but very challenging. Interestingly, we reach a very similar conclusion in our contributions to yeast prions in Part II but from completely different biological results.

3.3.3 Parallel with ecology

The coexistence of strains allowed by our model is similar to the phenomenon of "predation-mediated coexistence" in ecology.[1] First, in the basic model (Subsection 1.2.3) the aggregates, **predators**, compete for the same resource, **monomers**. As such, they cannot coexist which is coherent with the competitive exclusion principle in ecology. In our model (Section 3.1), the aggregates are still predators but they do not compete for the same subunits, the equivalent of **preys**. These subunits do compete for a shared resource, but the predation limits their proliferation and thus their resource uptake. This allows different strains of subunits to coexist (as long as they are in presence of aggregates). This type of coexistence was exhibited in some ecological systems, for instance the *Daphnia* planktons [Declerck and Meester, 2003, Gliwicz and Wrzosek, 2008].

Judging from this rationale, other ideas could potentially yield the same outcomes, namely coexistence and co-stability. One idea would be to bound the monomer uptake of aggregates by including a non-linear aggregation rate in the equations of the Nucleated Polymerization model (Subsection 1.2.3). Indeed if the polymerization speed saturated with high numbers of aggregates, we could potentially obtain coexistence. It could for example model the fact that the aggregates are in a constrained volume and their probability to encounter free monomers goes to 0 as their numbers grow. In the case of mammal brains or yeast cells, the aggregate densities at play are very low and the available volume is not limiting. This hypothesis is not relevant in our biological context, and this is why we do not develop it here.

[1] This side note is based on a comment we received during the review process for [Lemarre et al., 2018]. I found it interesting for general culture and chose to keep it in the final manuscript.

3.3.4 Conclusion

The model we introduce in this chapter suggests a way to explain how structural diversity impacts the behavior of prions. The range of behaviors exhibited by this model is far more extended than for the Nucleated Polymerization model, or any other classical model. However it is still far from reaching the level of complexity that prion processes display *in vivo*, but it emphasizes two essential components. Structural diversity, in particular intermediate steps in the polymerization pathway, is a key element to study prion strains and prion pathogenesis in general. The second key aspect is multi-stability, which allows for dependency on the inoculum and could be related to many puzzling results such as strain adaptation and selection. However, we have no proposition of a mechanistic model that supports this multi-stability, and no biological clue into the non-linearity we have empirically introduced in our model.

Chapter 4

Early oligomers and the genesis of structural diversity

This chapter is dedicated to the study of PrP oligomers formed *in vitro* which are, in some cases, precursors of infectious prion assemblies. These oligomers exhibit the same depth of structural diversity as prion aggregates observed *in vivo*, with different levels of organization and complex interactions. The onset of this diversity happens in a matter of minutes following thermal treatment of monomers, and so far no kinetic model accounts for the complete spectrum of structures formed in these early moments. We present here detailed biological results concerning OvPrP oligomers, emphasizing the signs of structural diversity. We use these clues to build a relevant kinetic model which

reproduces a number of specific experimental results and, in particular, the oscillatory behavior observed during depolymerization of H190A $P1$ oligomers.

4.1 The complexity of OvPrP oligomers

4.1.1 OvPrP spontaneously assembles into a diverse set of structures

Multiple subpopulations. As previously reported by different groups, OvPrP monomers spontaneously assemble into oligomers when incubated at elevated temperatures (at least 50°C) and at sufficient concentrations (above $3\mu M$) [Eghiaian et al., 2007,Chakroun et al., 2010]. Monitoring oligomerization experiments with Size-Exclusion Chromatography (SEC) reveals the presence of multiple subpopulations. SEC is an experimental tool which separates macromolecules depending on their size, by transporting them through a porous gel. Coupled with a spectroscopic method, it allows measurement of the amount of protein depending on the elution volume, which is directly related to the size of the assemblies. This gives a representation of the size distribution in the studied sample. In the case of OvPrP oligomers, a typical chromatogram is shown in Figure 4.1. The axis of ordinates is the absorbance at a set wavelength (here 280 nm), which is proportional to the concentration of PrP monomers for the corresponding elution volume. This means that the curve represents the distribution of the first-order moment over size, in other words it represents the percentage of PrP (monomers) in each size compartment. The relation between elution volume and size is inferred by calibration experiments, see [Armiento et al., 2017] for more details. The two peaks observed in Figure 4.1 (in addition to the monomer peak) were notably decorrelated as three underlying distributions by [Eghiaian et al., 2007], but this interpretation is mostly artificial, and we only consider two subpopulations. We refer to these as $P1$ and $P3$. $P3$ is centered around sizes of about 9-mers, and $P1$ ranges from 20-mers up to about 60-mers. Noticeably, $P1$ is the only subpopulation that is a precursor to prion fibrils as it condensates into infectious aggregates upon ultra-centrifugation. The properties of these distinct assemblies were assessed by various following experiments, including changing incubation conditions (concentration, temperature) and using different mutants of PrP [Eghiaian et al., 2007, Chakroun et al., 2010]. Figure 4.2 presents an overview of the effect of concentration on the dynamics of formation of these oligomers: both $P1$ and $P3$ appear within 2 minutes of incubation, but the growth of $P1$ and its shift towards larger sizes happens at a much slower pace. Remarkably, at low concentrations, $P1$ reaches larger sizes of assemblies than at high concentrations (the distributions shifts further to the left on the chromatograms).

Genetic manipulations reveal further levels of diversity. The most compelling evidence that these different structures interact is the fact that various point-mutations affect the balance between $P1$ and $P3$. As explored in [Chakroun et al., 2010], some mutants favor the formation of $P3$ or $P1$ or do not self-oligomerize at all. In partic-

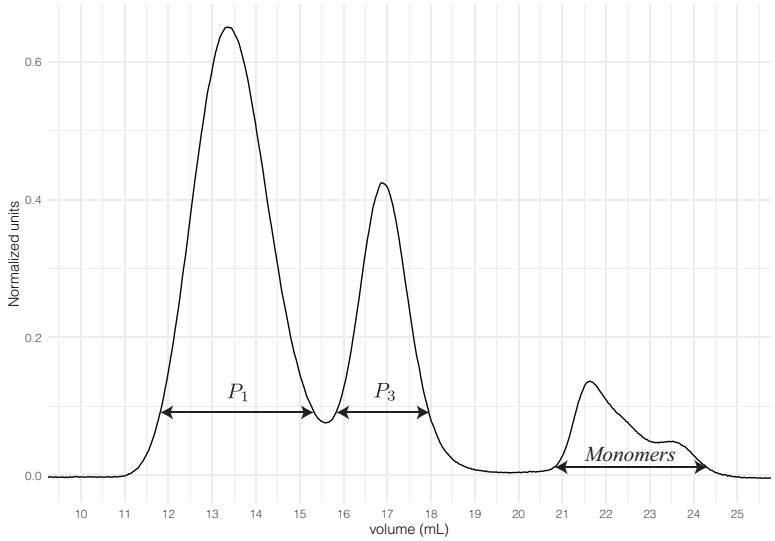

Figure 4.1 – **Size-exclusion chromatography of OvPrP oligomers.** Normalized absorbance at 280 nm versus elution volume, in the case of wild-type OvPrP oligomers formed by incubation of monomers at $100\mu M$ and 48 °C for 90 minutes. Data from [Eghiaian et al., 2007] and provided by H. Rezaei.

ular, the mutant H190A mostly accumulates under the $P1$ peak, as illustrated by the chromatograms in Figure 4.3. Since $P1$ is the only subpopulation that may lead to infectious prions, this mutant drew attention in previous studies [Armiento et al., 2017], and we investigate its behavior in detail in Subsection 4.1.2. To go even further in the investigation of point-mutations, co-polymerization experiments were led (unpublished data, H. Rezaei). It was observed that non-self-polymerizing variants of PrP are efficiently incorporated into existing $P1$ oligomers of wild-type or H190A PrP. Even more striking is the case of hetero-polymerization with subcritical concentrations of wild-type PrP. Subcritical refers to the case when the concentration of PrP is not elevated enough so that oligomers are formed in reasonable time (a few hours). Surprisingly, incubating subcritical wild-type monomers along with non-self-polymerizing monomers leads to the formation of full oligomer distribution and diversity, when neither of these reactants alone produce oligomers. This data is still under investigation and is yet unpublished, but it suggests that there is a conformational change which happens prior to accumulation of large assemblies, at least without accumulation of structures that may be distinguished from monomers with the resolution of SEC. This does not strictly exclude the possible accumulation of dimers or trimers. The precise role of this subcritical conformational change is unclear, but it does allow oligomerization of OvPrP mutants which do not aggregate in isolation. In our modeling approach (see Section 4.2) we propose a system that directly includes this property.

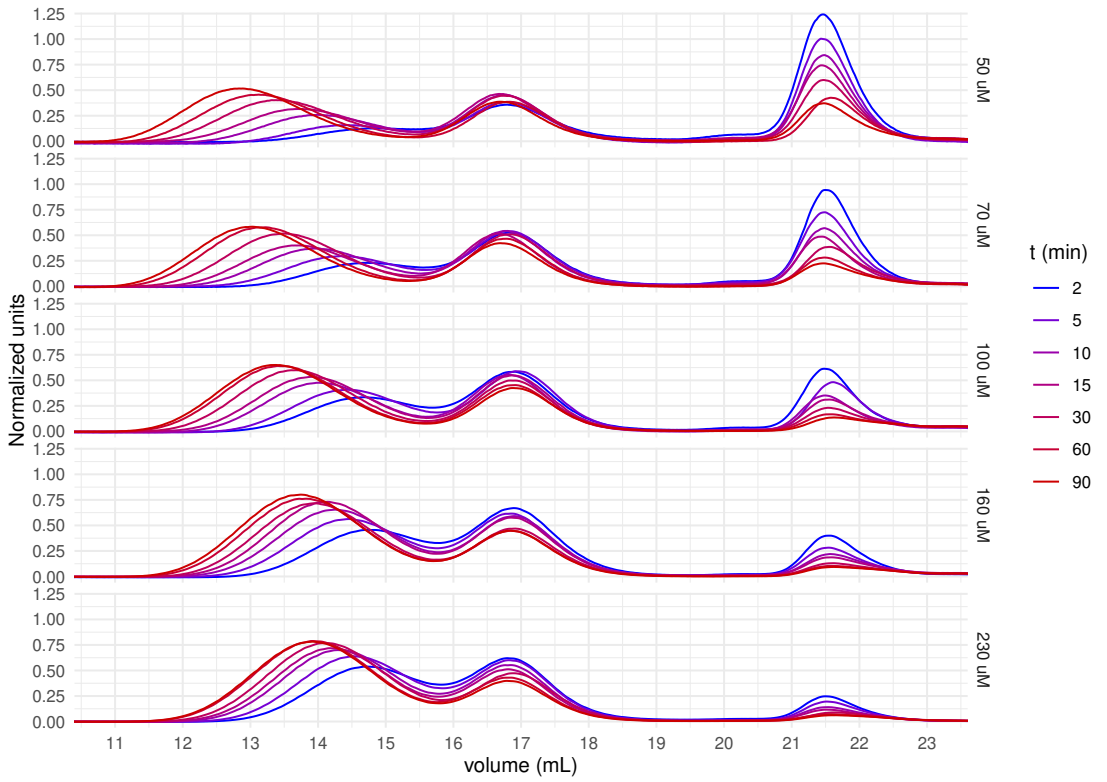

Figure 4.2 – **Dynamics of formation of wild-type OvPrP oligomers.** Size-exclusion chromatograms taken at various times (indicated by color) during incubation at 48°C and for various initial concentrations of wild-type OvPrP monomers (corresponding to rows). (data from [Eghiaian et al., 2007]).

Diversity of the $P1$ subpopulation. In order to explore the specific structure of $P1$, another experimental approach was suggested (which was not yet available at the time of [Chakroun et al., 2010]). Atomic Force Microscopy (AFM) allows the direct observations of molecules at the scale of a few nanometers. The setup consists of a scanning needle or tip, which probes the surface of the sample [Dufrêne et al., 2017]. The surface is typically made of crystal, such as mica, which is very flat, on which molecules have been deposited. The tip end is as sharp as a single atom, and moves vertically as the probe scans the sample surface. The vertical inclination is directly measured using a laser and a reflective cantilever. This experiment produces images in which each pixel contains a number corresponding to the height of the sample at this point, revealing information on the shape of the structures observed. A typical AFM image of $P1$ oligomers is shown in Figure 4.4. It reveals that the $P1$ subpopulation contains different types of elements, even though it appears as a unimodal distribution in chromatograms. At least two types of elements are identified and illustrated in Figure 4.4, namely the large spheres which

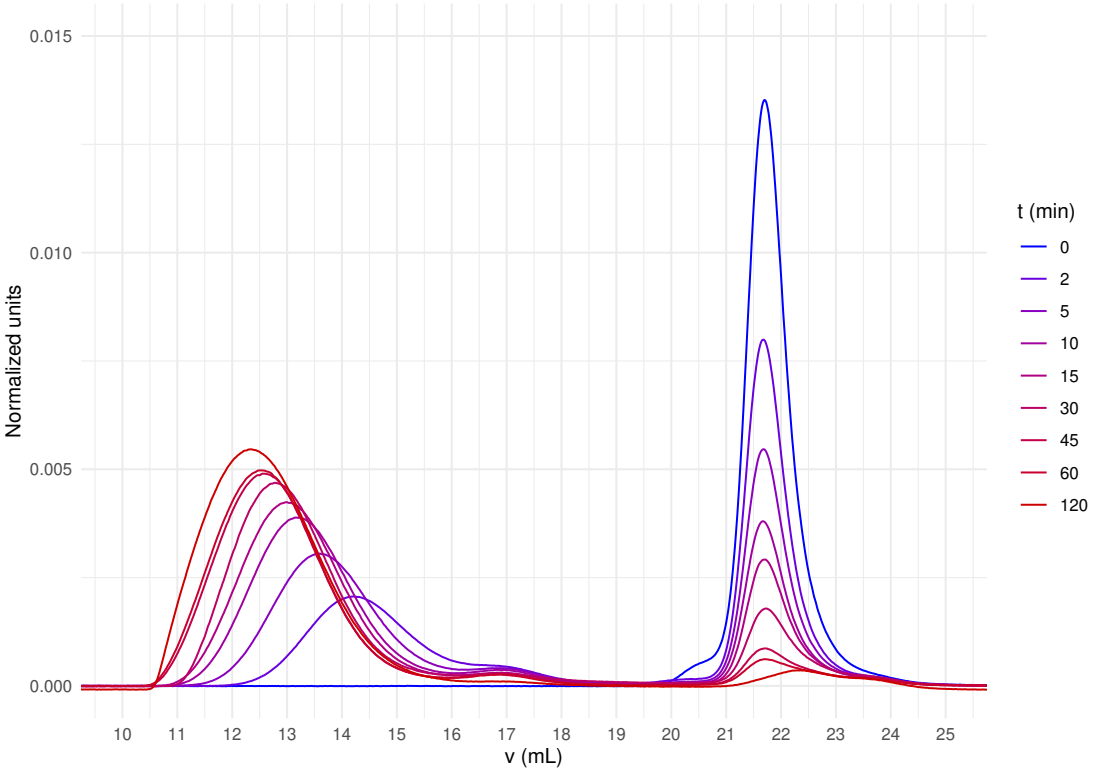

Figure 4.3 – **Dynamics of formation of H190A OvPrP oligomers.** Size-exclusion chromatograms taken at various times (indicated by color) during incubation at 48°C and for an initial concentration of 80μM of H190A OvPrP (H. Rezaei, unpublished).

we denote as S elements, and the straight extensions which we refer to as E elements. It has been suggested that S acts as a base for E to grow upon, although this is yet to be confirmed. AFM images are taken after isolating $P1$ oligomers (using a size-exclusion process) from the rest of the system which means that monomers are not present when the images are captured. Note that OvPrP oligomers are inactive and immobile at room temperature, hence they do not move during the AFM process.

4.1.2 Depolymerization experiments and the case of H190A

Static Light Scattering as non-invasive monitoring technique. One approach to investigate the properties of the different subpopulations identified through SEC or AFM imaging is to subject these structures to thermal treatment in order to destabilize them. These experiments, generally referred to as depolymerization experiments, are often monitored using a technique called Static Light Scattering (SLS). SLS is based on the principle of Rayleigh diffusion by objects smaller than the wavelength [Hulst and van de Hulst, 1981]. A laser beam is focused on the sample, and the scattered light intensity at a cer-

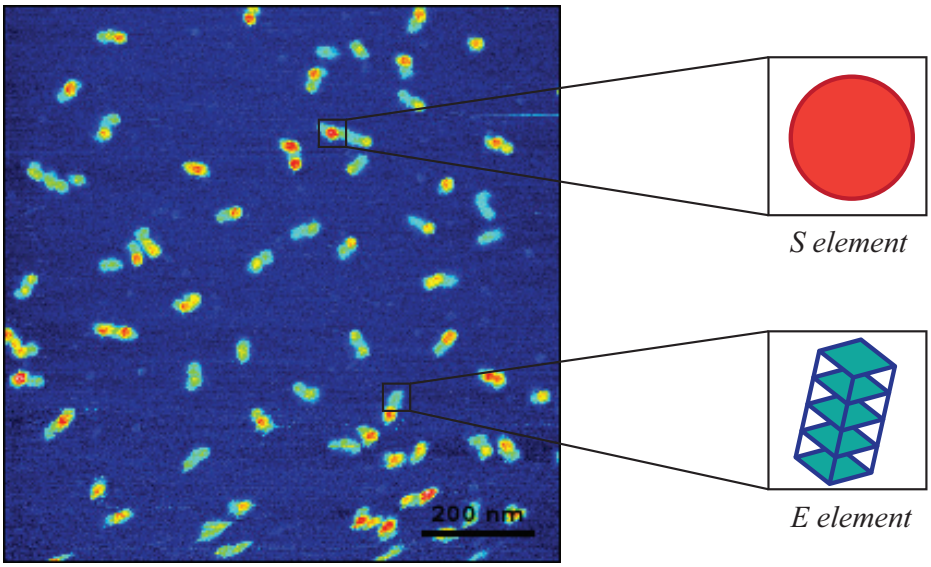

Figure 4.4 – **Typical AFM image of wild-type $P1$ oligomers.** (Left) The color codes for the height of the objects, from 0 (blue) to 8 nm (red). (Right) Schematic representation of the different types of elements identified in the $P1$ subpopulation. (H. Rezaei, unpublished).

tain angle is measured continuously as the chemical system evolves. At each time point, the incident intensity and the scattered intensity are proportional. The ratio depends on calibration parameters, the wavelength of the laser, the total concentration of the sample, but also on the molecular weight of the assemblies in the sample. In fact, it is directly proportional to weight-average molecular weight of the sample $\langle M_w \rangle$ (as opposed to the number-average molecular weight). If the index i denotes the size of the objects in the sample (in terms of number of monomers) and $C_i(t)$ denotes the concentration of objects of size i at time t, this quantity writes as

$$\langle M_w \rangle (t) = \frac{\sum_{i=1}^{\infty} i^2 C_i(t)}{\sum_{i=1}^{\infty} i C_i(t)}.$$

During an experiment monitored by SLS, the reaction happens in a vial and the system is closed, which means the total concentration of monomers in the system $\sum_{i=1}^{\infty} i C_i(t)$ does not change. In this case, the SLS signal is directly proportional to the order two moment of the size distribution of elements in the solution $\sum_{i=1}^{\infty} i^2 C_i(t)$. It is thus an averaged and non-linear evaluation of the size of the objects in real time. The timescale of such a measurement is of about $10s$. Consequently, monitoring a reaction by SLS gives insight into the underlying dynamics of the system in a way that is not achievable

with SEC or AFM. Indeed, even if multiple chromatographies are realized at different time points, it is not reasonable to aim for a time-resolution of less than a few minutes. For our purposes here, we do not go into further detail regarding the SLS measurement and the physics of light scattering (we redirect the interested reader to [Hulst and van de Hulst, 1981] for more information).

Depolymerization of wild-type $P1$ reveals the transfer from one subpopulation to another. The depolymerization of wild-type $P1$ was studied in detail by [Armiento et al., 2017]. The $P1$ subpopulation was isolated (with a process similar to SEC), diluted to a given monomer-equivalent concentration and then subjected to thermal treatment at 70°C. The SLS monitoring of these experiments revealed that, above a certain concentration of about $7\mu M$, the depolymerization of $P1$ was followed by the slow accumulation of large species, as illustrated in Figure 4.5. This was confirmed by taking SEC chromatograms at various time points (see [Armiento et al., 2017]). These chromatograms showed no sign of accumulation of an intermediate between $P1$ and the monomer during the depolymerization phase or the re-polymerization phase. The objects formed after unfolding and refolding were observed to be even larger than the objects initially present in the sample. An explanation was suggested, a simple one-way transition of mass between two underlying subpopulations, and a mathematical model was proposed, which reproduced the results with satisfying agreement.

The case of H190A depolymerization. As mentioned above and illustrated in Figure 4.3, H190A was identified as a mutant which favors the formation of mostly $P1$ [Chakroun et al., 2010]. Upon investigation with AFM, H190A $P1$ oligomers appear similar to wild-type $P1$ (not shown). However, depolymerization of H190A $P1$ reveals complex and unaccounted for behavior. In these experiments, H190A OvPrP was first incubated at $100\mu M$ and 55°C for 5 hours, then $P1$ was isolated using size-exclusion chromatography. It was diluted to the desired monomer-equivalent concentration and then subjected to constant heating at 70°C. The SLS signal obtained during depolymerization at various concentrations is shown in Figure 4.6. The different observations start with the same initial composition of objects, the only difference being the dilution of these objects. This explains why the SLS curves overlap at the beginning[1]. The difference with the depolymerization of wild-type $P1$ is striking. A few features are worth pointing out. First we observe an initial exponential decrease. This initial phase does not seem to depend on concentration, which suggests an order 1 reaction. However the slow oscillations that follow are extremely dependent on concentration. The depolymerization seems particularly accelerated at the specific concentration of $1\mu M$. This nonmonotonic variation with concentration is likely the result of an intricate kinetic scheme, with multiple orders of reaction involved. The second noticeable behavior is the fast spiking observed at the

[1]The calibration was also kept identical through all the different experiments with H190A, which was not the case for the wild-type depolymerization experiments shown in Figure 4.5.

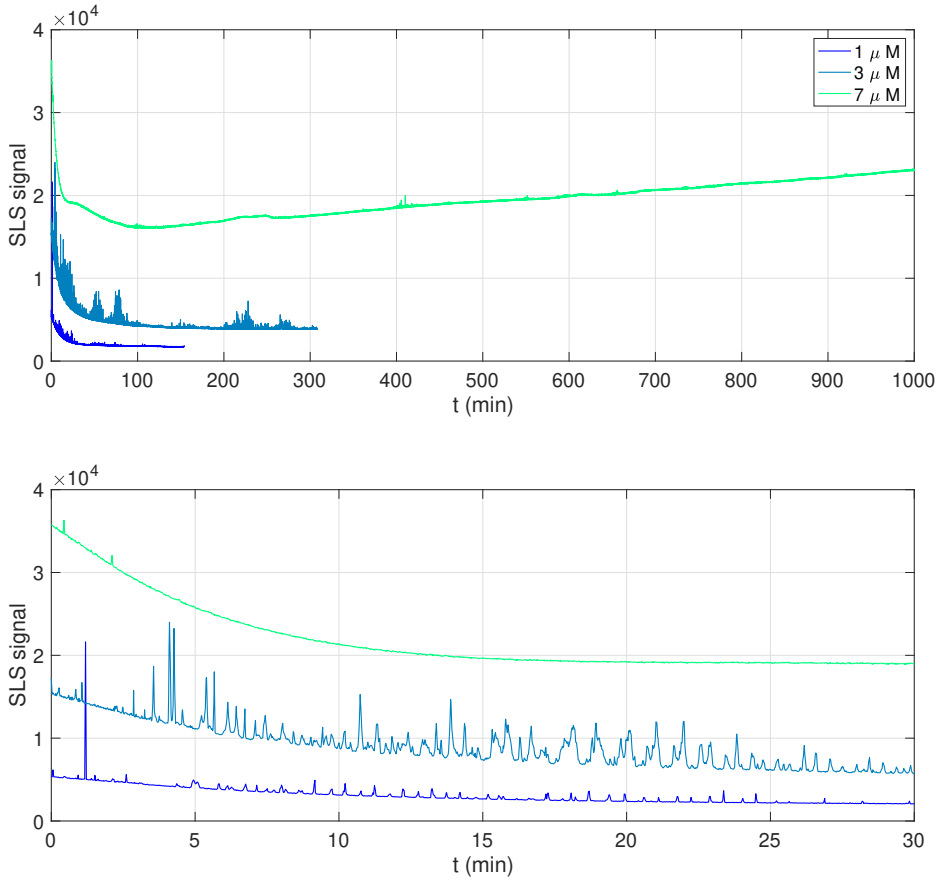

Figure 4.5 – **SLS monitoring of the depolymerization of wild-type** $P1$**.** The depolymerization of isolated $P1$ subpopulation at 70 °C was monitored by SLS, at different monomer-equivalent concentrations, in function of time. (Top) Full time range of experiment. (Bottom) First 30 minutes. (data from [Armiento et al., 2017]).

scale of a few minutes. These spikes are most likely not experimental artefacts, because further experiments revealed that they were highly reproducible (data not shown). Instead the spiking behavior suggests that there are multiple time scales involved in the dynamics of this system. In fact similar spiking is also observed in the case of the wild-type $P1$ (see Figure 4.5), even though it was dismissed in earlier studies [Armiento et al., 2017].

4.1.3 Objective and modeling hypotheses

The detailed investigation of OvPrP oligomers unveiled a surprising amount diversity and complex interactions. Although it is a simple experimental system in practice (a

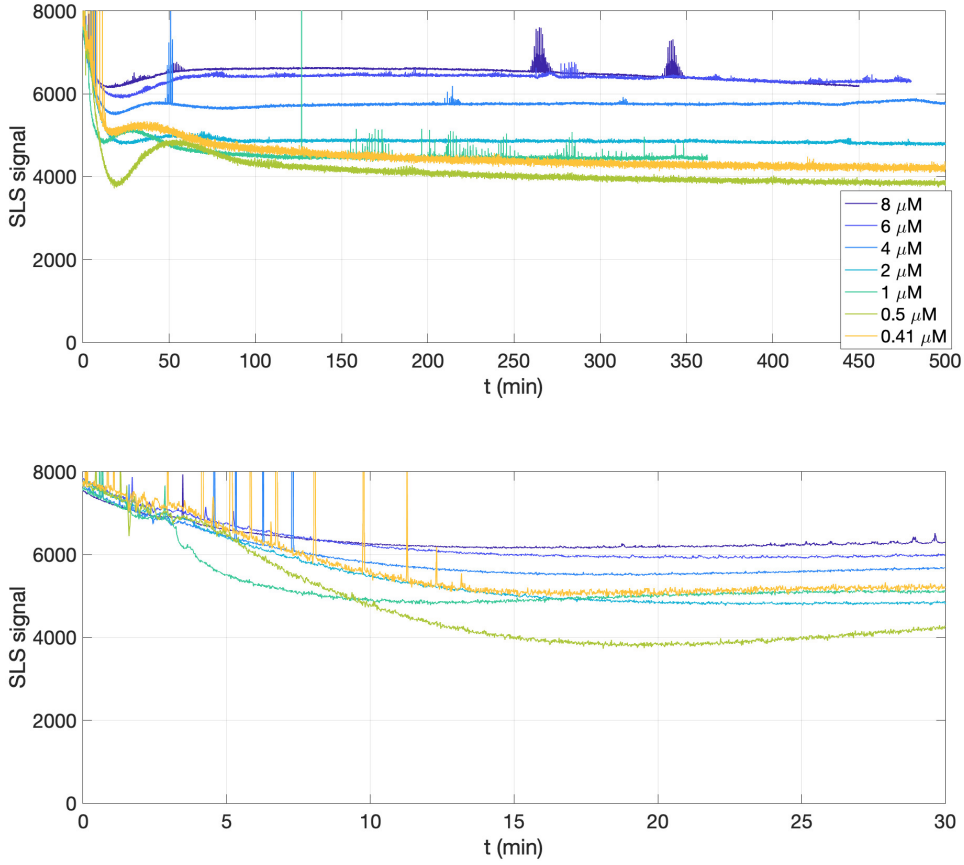

Figure 4.6 – **SLS monitoring of the depolymerization of H190A** $P1$**.** The depolymerization of isolated $P1$ subpopulation from H190A oligomers at 70°C was monitored by SLS, at different monomer-equivalent concentrations, in function of time. (Top) Full time range of experiment. (Bottom) First 30 minutes. (H. Rezaei, unpublished).

single protein, taken in isolation and subjected to thermal treatment), it requires an intricate kinetic model in order to be successfully reproduced. For the sake of clarity and efficiency, we reduce the problem to a few questions of interest and we propose a set of relevant hypotheses to frame our approach.

Depolymerization of H190A $P1$**: non-linear concentration effects and multiple timescales.** The particular problem we focus on for the rest of this chapter is the depolymerization of $P1$ oligomers formed from H190A OvPrP mutant. The curves presented in Figure 4.6 show intricate behavior, with the interlacing of reactions at different timescales. The nonmonotonic effect of concentration on the order two moment is in-

triguing and no classical model reproduces this behavior. Indeed with classical models of growth-fragmentation, the only order two kinetic rate is usually the polymerization reaction. This reaction thus outscales the others as concentration increases, and the effect on the order two moment is monotonic (increasing). To the best of our knowledge, no published model allows for an accelerated drop in size at a specific concentration. A novel process must be introduced, and we suggest one in Section 4.2. Our aim is to reproduce the qualitative behavior of the curves in Figure 4.6, both the concentration effects and the spiking. Although we focus on depolymerization experiments, we strive to build a model that also allows representing oligomerization experiments.

Working hypotheses. In order to be biologically relevant and to limit the modeling possibilities, we define a set of framing hypotheses. The studied system is closed and no degradation of PrP monomers happens during the length of the experiment, which means our model should verify mass conservation (in terms of monomers). The system is fairly purified and the only chemical species in action is PrP. For this reason, we restrict ourselves to mass-action kinetic rates based on mechanistic interactions of the objects. We artificially impose some kinetic scaling orders, but without overstepping the threshold of a total kinetic order of 3 for a single reaction. This means that our modeling approach does not include activation functions, enzyme-substrate dynamics or other complex non-linearities. Indeed our goal is to identify key processes and a minimal set of non-linear interactions to obtain the qualitative behavior described earlier.

4.2 Introducing a kinetic model of H190A oligomers

We propose here a kinetic model for the dynamics OvPrP oligomers, built from experimental observations and reasonable assumptions, within the framing hypotheses described in Subsection 4.1.3. Our specific goal here is to reproduce the qualitative behavior of depolymerization experiments of $P1$ oligomers from H190A.

4.2.1 From biological observations to model design

Introducing a transient dimer species. As mentioned in Section 4.1, a conformational change happens prior to accumulation of large species, and this change is a necessary intermediate in the polymerization pathway of $P1$. We suggest the existence of a transient dimeric (size 2) species T which forms spontaneously from monomers M with a rate α, autocatalyses with a rate ρ and disassembles back into monomers with a rate ω. This corresponds to the following reactions

$$\begin{aligned} \mathrm{M} + \mathrm{M} &\xrightarrow{\alpha} \mathrm{T}, \\ 2 \cdot \mathrm{M} + \mathrm{T} &\xrightarrow{\rho} 2 \cdot \mathrm{T}, \\ \mathrm{T} &\xrightarrow{\omega} 2 \cdot \mathrm{M}. \end{aligned}$$

Evidence for an intermediate species was suggested in oligomerization experiments (unpublished, H. Rezaei), where it prevents the formation of assemblies by mutants that do not form this transient species. The spontaneous formation rate α is assumed to be much lower than the autocatalytic replication rate ρ, so that α only influences the early stages of oligomer formation.

Modeling $P1$ oligomers as a base S and an extension E. Based on the observations of AFM images of $P1$ oligomers (see Figure 4.4), we describe these objects using two types of constituting elements. The S element acts as a building pedestal for the extension E to grow. This assumes that S elements appear first during the oligomerization, and form the initial $P1$ peak observed in chromatograms (see Figure 4.3 and Figure 4.2). The shift of this peak towards larger sizes then corresponds to the growth of E extensions on the already formed S elements. This hypothesis is still under investigation, in particular via algorithmic image analysis of AFM pictures (see Subsection 4.4.2). We describe E extensions with a discrete size-distribution of elements E_i, $i \geq 0$. By convention E_0 corresponds to a single S element. We consider that the growth of E_i into E_{i+1} corresponds to the addition of two monomers at the end, with rate τ. These two monomers are assembled together at the moment of polymerization into the aggregate E_i to form a dimeric subunit. On the other hand, E_{i+1} releases a dimer T when depolymerizing to E_i, which happens at rate δ. In terms of modeling, the size-distribution of E follows a modified Becker-Döring system, where the polymerization reaction depends on the monomer concentration at the order 2. The asymmetry between the polymerization and depolymerization reactions is essential in order to obtain oscillating behavior and instabilities in the model. A similar asymmetry in a Becker-Döring model is proposed and investigated in [Doumic et al., 2019]. We note that this hypothesis has not been confirmed or contradicted by experimental evidence yet. The polymerization and depolymerization reactions for E_i, $i \geq 0$ are given as follows, for $i \geq 0$

$$\begin{aligned} \mathrm{E}_i + 2 \cdot \mathrm{M} &\xrightarrow{\tau} \mathrm{E}_{i+1}, \\ \mathrm{E}_{i+1} &\xrightarrow{\delta} \mathrm{E}_i + \mathrm{T}. \end{aligned}$$

E_0 corresponds to a single S element, which is of size n_S. E_i corresponds to a base S with an extension of i subunits, which makes it size $n_S + 2i$.

Autocatalysis of S elements. The formation of base elements S is different from E elements because they seem to be homogoneous in size (see Figure 4.4). Furthermore, the assembly of S elements happens very rapidly at the beginning of oligomerization experiments and reaches a plateau after a few minutes, without accumulation of any intermediates (see Figure 4.3). Consequently, we propose an autocatalyzed mechanism for the formation of S. In particular, we consider that S is formed of 6 dimers which makes it a 12-mer ($n_S = 12$). We assume that the kinetic rate β of S formation depends

on the concentration of S at the order 2, which implies a cooperative mechanism. This is a strong hypothesis that is difficult to support with experimental data. However, mathematically speaking, it introduces a variety of behavior to the model that is not otherwise possible. We also include an order 3 reaction with rate σ which creates an S from T subunits. The rate σ is assumed to be much lower than the catalyzed rate β, so that the dynamics of depolymerization are driven by β but the oligomerization from a pool of monomers only is still be possible via σ (and α). This is formalized by the following reactions

$$6 \cdot \mathrm{T} + 2 \cdot \mathrm{S} \xrightarrow{\beta} \mathrm{S} + 2 \cdot \mathrm{S},$$
$$6 \cdot \mathrm{T} \xrightarrow{\sigma} \mathrm{S}.$$

Sequential depolymerization of S elements. In order to reproduce the intricate depolymerization behavior observed in Figure 4.6, we introduce a special depolymerization mechanism for S elements. We suggest that an S element first disassembles partially with rate μ into two transient objects W of size $n_W = 6$. These objects are exetremely unstable and have multiple ways of disassembling. They either spontaneously dismantle with rate γ into T elements, or they react with each other with rate λ to release monomers. The final hypothesis we make about W objects is that they destabilize S and lead to its fragmentation into two W with rate k. This catalyzed depolymerization is essential in order to reproduce the accelerated drop in the SLS signal observed at $1\mu M$. The multiple depolymerization pathways of W allow cycling to occur, depending on the concentration. Indeed when T is released directly then it favors the formation of new S objects, however when monomers are released it rather favors the growth of E objects. These assumptions are summarized in the following set of reactions

$$\mathrm{S} \xrightarrow{\mu} 2 \cdot \mathrm{W},$$
$$\mathrm{W} \xrightarrow{\gamma} 3 \cdot \mathrm{T},$$
$$\mathrm{W} + \mathrm{W} \xrightarrow{\lambda} 12 \cdot \mathrm{M},$$
$$\mathrm{S} + \mathrm{W} \xrightarrow{\mathrm{k}} 2 \cdot \mathrm{W} + \mathrm{W}.$$

The global kinetic system we propose and use is summarized in Figure 4.7. The mathematical expression of this model, as well as the choice of parameters, is detailed in Section 4.3.

4.2.2 Mathematical formulation

The model introduced in Subsection 4.2.1 is now formulated as a system of ordinary differential equations. It considers the concentration of transient dimers T, of base elements S, of depolymerization intermediates W, of extensions E_i and of monomers V.

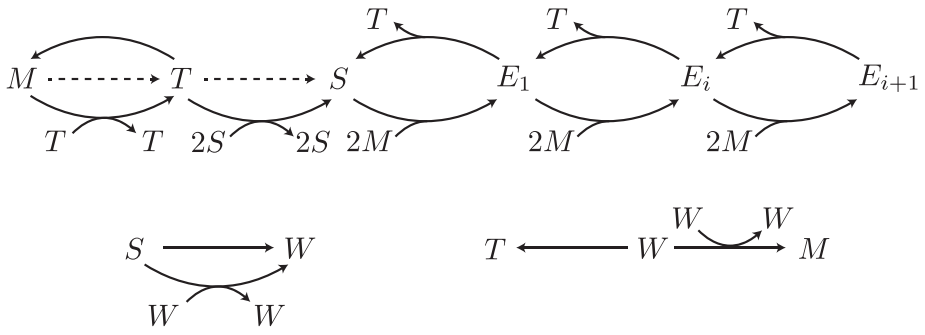

Figure 4.7 – **Kinetic scheme proposed to model H190A** $P1$ **oligomers.** Tangent arrows indicate a catalyzed reaction, and joining arrows indicate a reaction between multiple reactants. Dashed-line arrows indicate a slow reaction.

The initial monomer-equivalent concentration in the system is denoted by C_0. This system is formally of infinite dimension because we consider E_i sizes for all $i \geq 1$. The reactions introduced in Subsection 4.2.1 are transcribed into System (4.1).

$$\begin{cases} \dot{T} = \alpha V^2 + \rho V T - \omega T - \dfrac{n_S}{n_T}(\sigma T^3 + \beta S^2 T) + \delta \displaystyle\sum_{i\geq 1} E_i + \dfrac{n_W}{n_T}\gamma W, \\ \dot{S} = \dot{E}_0 = \sigma T^3 + \beta S^2 T - \mu S - kSW - \tau S V^2 + \delta E_1, \\ \dot{W} = \dfrac{n_S}{n_W}(\mu S + kSW) - \gamma W - \lambda W^2, \\ \dot{E}_i = \tau E_{i-1} V^2 - \delta E_i - (\tau E_i V^2 - \delta E_{i+1}),\ i \geq 1 \\ V = C_0 - n_T T - n_W W - n_S S - \displaystyle\sum_{i\geq 1}(n_S + i n_T) E_i, \\ n_T = 2,\ n_W = 6,\ n_S = 12. \end{cases} \tag{4.1}$$

The well-posedness of this system is justified by Proposition 4.1.

Proposition 4.1. *Assume all parameters of System* (4.1) $\alpha, \rho, \omega, \sigma, \beta, \mu, k, \gamma, \lambda, \tau, \delta, C_0$ *are positive. For an initial condition* $(T_0, S_0, W_0, (E_{0,i})_{i\in\mathbb{N}^*})$ *chosen in*

$$X_+ = \{(Y_k)_{k\in\mathbb{N}} : \forall k \geq 0, Y_k \geq 0\},$$

and which verifies

$$n_T T_0 + n_W W_0 + n_S S_0 + \sum_{i\geq 1}(n_S + i n_T) E_{0,i} \leq C_0,$$

the system admits a unique global solution.

Furthermore, for all $t \geq 0$, $(T(t), S(t), W(t), (E_i(t))_{i\in\mathbb{N}^*})$ *is in* X_+ *and*

$$n_T T(t) + n_W W(t) + n_S S(t) + \sum_{i\geq 1}(n_S + i n_T)E_i(t) \leq C_0.$$

Proof. The autonomous ordinary differential system defined by (4.1) is C^1 since all terms are polynomial, and is thus locally-Lipschitz. The Cauchy-Lipschitz theorem gives the existence and uniqueness of a maximal solution. Next, we note that the last equation of the system is equivalently replaced by the following ordinary differential equation on V

$$\dot{V} = n_T(-\alpha V^2 - \rho V T + \omega T - \tau V^2 S - \tau V^2 \sum_{i\geq 1} E_i) + n_W \lambda W^2,$$

as long as the initial condition verifies

$$V_0 + n_T T_0 + n_S S_0 + n_W W_0 + \sum_{i\geq 1}(n_S + i n_T)E_{i,0} = C_0.$$

With this formulation, it is straightforward to verify that X_+ is positively invariant for the modified system. This allows us to conclude that the maximal solution (for an initial condition in X_+) remains positive over all its definition interval. Recalling now that the system conserves mass (and switching back to the formulation (4.1)), the positivity of the solution implies that it is bounded as stated in the Proposition. In consequence there is no explosion in finite time and the solution is global. □

As of yet, the analytical results on the model are limited to Proposition 4.1 and further analytical study is planned for future work. We now proceed with a numerical investigation of its behavior. One important remark is that in our model, the order two moment of the distribution (the weight-average molecular weight) is expressed as

$$\langle M_w \rangle = \frac{1}{C_0}\left(V + n_T^2 T + n_W^2 W + n_S^2 S + \sum_{i\geq 1}(n_S + i n_T)^2 E_i\right). \tag{4.2}$$

4.3 Results

4.3.1 Model scaling and parameter choice

Dealing with infinite sizes. The system introduced Section 4.2 is infinite, but in practice we consider a finite size-distribution. In the simulations, a size threshold N is defined and System (4.1) is truncated by considering the last equation

$$\dot{E_N} = \tau V^2 E_{N-1} - \delta E_N.$$

The approximation of the full system is acceptable as long as the buffer compartment E_N does not accumulate mass. For all our simulations the threshold is set at $N = 100$, which corresponds to a physical maximal size of $n_S + N \times n_T = 212$ (in terms of monomers). In the experiments, the largest $P1$ oligomers observed are approximately of size 70 [Armiento et al., 2017]. As long as our model verifies this order of magnitude on the size, the threshold $N = 100$ is sufficiently large.

Parameter choice and scaling. Choosing the parameters for such a complex model is a problem in itself. We focus here on reproducing qualitative behavior observed in the experiments, but we do not propose a quantitative fit of the data. However, physical constraints have to be respected for the parameters to be relevant biologically. In particular, catalyzed reactions are limited by the so called diffusion-limit [Alberty and Hammes, 1958], which takes into account the geometry of molecules and their interactions through simple diffusion. It implies that the upper bound for second order constant rates is $10^9 M^{-1}s^{-1}$. This estimation goes up to $10^{10}M^{-1}s^{-1}$ by taking into account the effect of force fields [Kuo-Chen and Shou-ping, 1974]. In general, enzymes are not kinetically perfect and typical constant rates are around $10^6 - 10^7 M^{-1}s^{-1}$. Judging from the concentrations studied experimentally and the typical timescales involved, we choose the concentration scaling of $1\mu M$ and the time scaling of 1min. The diffusion-limit upper bound becomes approximately $10^5 \mu M^{-1}\text{min}^{-1}$ and reasonable constant rates lie within the range $10^1 - 10^2 \mu M^{-1}\text{min}^{-1}$ (this corresponds to the parameters α, ρ, λ, k in the model). This approximation is extended to order three reaction rates by adding a concentration estimation to one of the species involved. In our case, we consider that the concentrations involved in order three reactions (rates σ, β which involve T and S, and rate τ which involves V and E_i) are of the order of $1\mu M$. This means that reasonable values for the order three constant rates are within the range $10^1 - 10^2 \mu M^{-2}\text{min}^{-1}$. Finally, for first order reactions the rates are limited by the vibration properties of proteins which gives a range of $10^{-2} - 10^1 \text{min}^{-1}$ (parameters $\omega, \mu, \gamma, \delta$ in the model). The parameters involved in our model, as well as the default values used for the simulations are summarized in Table 4.1. The default values correspond to the case which we are interested in, the depolymerization of $P1$ oligomers at 70 °C. At such an elevated temperature, the Arrhenius equation predicts an significant increase of rate constants compared to room temperature [Arrhenius, 1889]. This justifies setting some constants on the upper edge of the reasonable range of $10^1 - 10^2 \mu M^{-1}.\text{min}^{-1}$.

4.3.2 Numerical results

The modeling hypotheses are verified. Before investigating the depolymerization of $P1$ oligomers with our model, we make sure that our working hypotheses (as expressed in Subsection 4.1.3 and Subsection 4.2.1) are verified in the simulations. Figure 4.8 shows a simulation of the model in the context of oligomerization of H190A OvPrP. It is designed to represent oligomerization at $100\mu M$ and $55°C$ during 5 hours, which are the condi-

Table 4.1 – **Parameter definitions and values used for numerical simulations in the model of H190A OvPrP $P1$ oligomers.** The default values correspond to the depolymerization case (70 °C). See Subsection 4.3.1 for details on the parameter choice.

Parameter	**Value** at 70°C (55 °C)	**Unit**	**Description**
α	10^{-3}	$\mu M^{-1}\text{min}^{-1}$	Spontaneous T formation rate
ρ	0.8	$\mu M^{-1}\text{min}^{-1}$	Autocatalysis of T
ω	0.1	min^{-1}	Disassembly of T
n_T	2	-	Size of T
σ	10^{-3}	$\mu M^{-2}\text{min}^{-1}$	Spontaneous S formation rate
β	130	$\mu M^{-2}\text{min}^{-1}$	Autocatalysis of S
μ	0.01	min^{-1}	Disassembly of S
n_S	12	-	Size of S
γ	8	min^{-1}	Disassembly of W into T
λ	35	$\mu M^{-1}\text{min}^{-1}$	Self-disintegration of W into V
k	100	$\mu M^{-1}\text{min}^{-1}$	Catalyzed depolymerization of S by W
n_W	6	-	Size of W
τ	1	$\mu M^{-2}\text{min}^{-1}$	Polymerization of V by E_i
δ	0.7	min^{-1}	Depolymerization of E_i into T and E_{i-1}
C_0	0.1-10 (100)	μM	Total OvPrP concentration in the system
N	100	-	Numerical maximal size for the system

tions used to form $P1$ before depolymerization as shown in Figure 4.6. We use the last time point ($t = 300$ min) of Figure 4.8 as an initial condition for our depolymerization simulations (see next paragraph). This first simulation is relevant because it shows that the dynamics of the model are similar to these observed experimentally. The formation of base elements S happens within the first 2 minutes of the experiment. The later stages correspond to the slow evolution the distribution of E_i towards larger sizes. We note that the depolymerization intermediate W stabilizes at around 0.01% of the PrP mass. This is correlated with the limited accumulation of peak $P3$ during oligomerization of H190A (see Figure 4.3). Furthermore, the distribution obtained after 5 hours is restricted to sizes smaller than 80, which is in agreement with the sizes observed in the experiments. This justifies the approximation used which limits the maximal size of objects (see Subsection 4.3.1). However, these simulations are not entirely satisfactory as compared to Figure 4.3, as discussed in Subsection 4.4.2. We next examine the depolymerization behavior of the model.

Nonmonotonic and non-linear effect of concentration. The simulation of depolymerization of H190A $P1$ oligomers is shown in Figure 4.9. We plot the evolution of the second order moment, as expressed in Equation (4.2), versus time and depending on concentration. The numerical conditions are designed to mimic the experiment illustrated in Figure 4.8. In particular, the initial condition corresponds to the isolated distribution of E_i objects from the oligomerization simulation shown in Figure 4.8 (at $t = 300$ min).

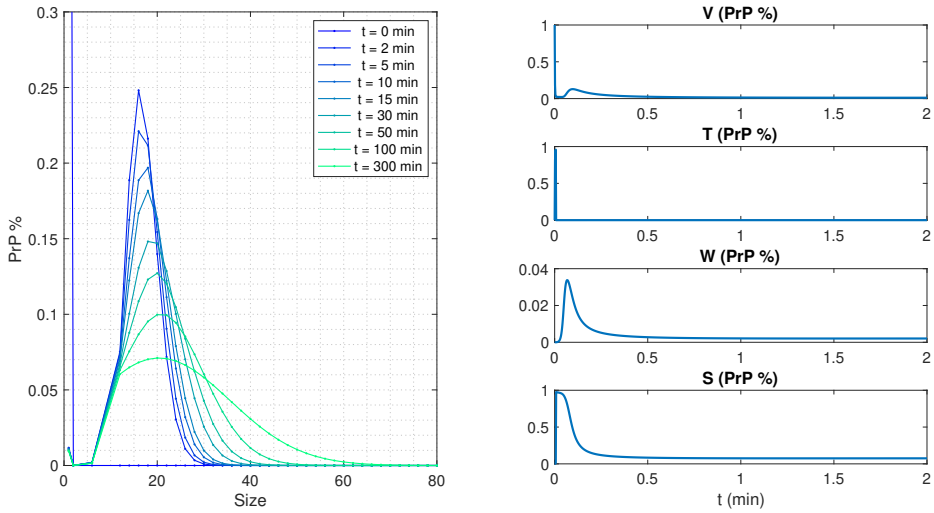

Figure 4.8 – **Model simulation in the context of H190A oligomerization.** The initial condition correponds to a concentration of $100\mu M$ of pure monomer, and the parameters are set to the default values (see Table 4.1), except $\gamma = 5$ min$^{-1}, \tau = 0.1\ \mu M^{-2}min^{-1}, \delta = 0.1$ min$^{-1}, k = 10\ \mu M^{-1}$min^{-1}. (Left) Evolution of the size-distribution at different times. (Right) Detailed evolution of the PrP proportion in V (monomers), T (transient dimers), W (depolymerization intermediate) and S (base elements) during the first 2 min of the oligomerization.

These curves illustrate the nonmonotonic effect of concentration. Just as observed in the experiment, for a certain concentration (about $1\mu M$) the order two moment drops faster and to a lower value than at other concentrations. The depolymerization is slowed at high concentrations and at low concentrations, but for different reasons. This effect is explained in our model by the balance between instability of W and catalyzed depolymerization of S (by W). As concentration increases, W is increasingly unstable, but its effect on S is stronger. With a suitable choice of parameters, there is a concentration at which the destabilization of S is maximal. The qualitative nonmonotonic effect of concentration clearly depends on the presence of a catalyzed depolymerization process in the kinetic scheme.

Interaction between different timescales. A feature exhibited both in the simulations (Figure 4.9) and the experiments (Figure 4.6) is the interaction between at least two timescales. The slow oscillations (at the scale of dozens of minutes) are coupled with very fast oscillations (at the scale of a few seconds). This spiking behavior is explained in our model by the possible cycling during the depolymerization of S elements. The multiple successive autocatalyzed reactions (formation of S, depolymerization of S into W) allow fast excursions to occur without seemingly affecting the slow behavior of E_i el-

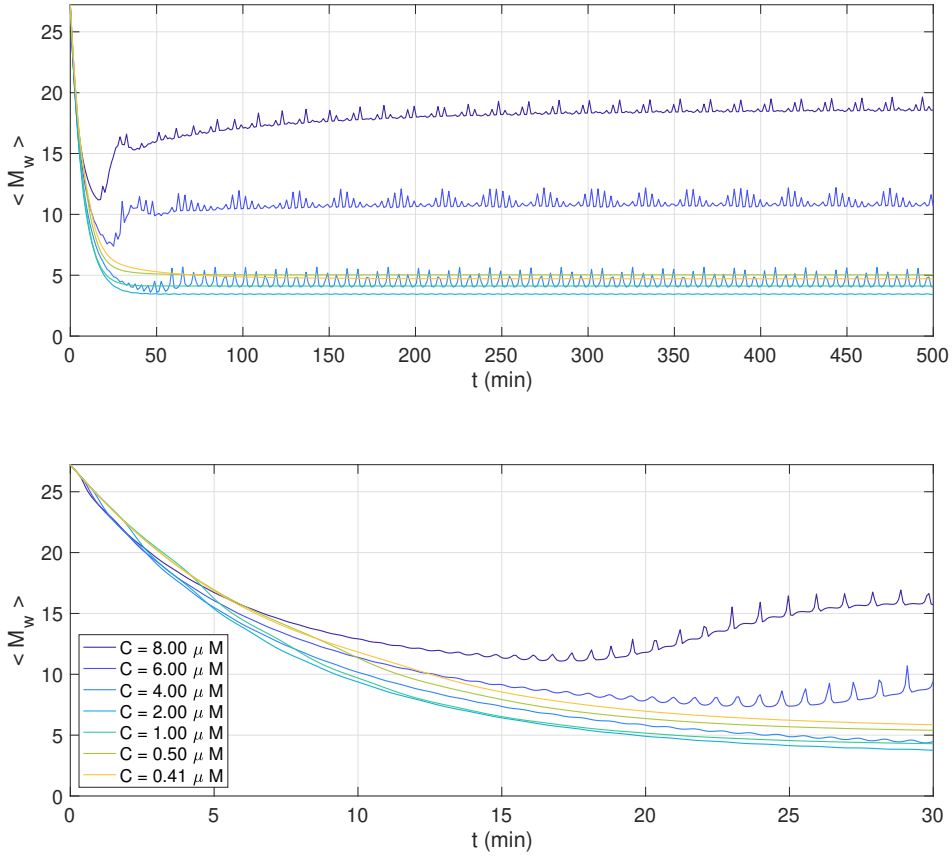

Figure 4.9 – **Model simulation in the context of H190A depolymerization.** The conditions are designed to represent the experiment shown in Figure 4.6. The initial condition correponds the simulated distribution after $t = 300$ min shown in Figure 4.8. The parameter values are detailed in Table 4.1. (Top) Full time range of simulation. (Bottom) First 30 minutes.

ements. This results in complex periodic cycling behavior, which resemble the transient spike trains observed in the experiments. However, in the simulations the oscillations seem stable which does not correlate with the sudden and brief oscillatory behavior of experimental curves. Another issue, in the experiments, spikes are observed even at the lowest concentration $C_0 = 0.41\mu M$, but our model does not reproduce this behavior. Despite these issues, this is the first model of prion oligomers which exhibits complex oscillations and multiple timescale interactions.

4.4 Discussion

4.4.1 Insight into prion biology

On the importance of structural diversity. Even though the global scheme we introduce in Section 4.2 and investigate in Section 4.4 is complex, it is in fact almost minimalist. The nonmonotonic effect of concentration and the spiking observed during the depolymerization could not be reproduced by simpler models. This does not prove that our model is the right model, but it shows how important structural diversity is in the formation of prion oligomers. In order to represent the complex evolution of a single subpopulation of oligomers, we are required to introduce at least 5 different species in the kinetic scheme. This is suprisingly diverse for objects that form spontaneously in a few minutes, but every recent piece of information points in this direction.

Unprecedented interactions. The architecture of the kinetic scheme we suggest (see Figure 4.7) is novel and unprecedented in prion modeling. In particular, catalyzed depolymerization appears critical in reproducing the effects of concentration on the evolution of the order two moment. This opens new considerations in terms of prion modeling in general, as catalyzed depolymerization might be occuring more generally during the aggregates replication. Note that a similar process was suggested in [Doumic et al., 2019] for the study of the oscillatory behavior of PrP^{Sc} aggregates *in vitro*. In fact, catalyzed depolymerization might be at the heart of secondary nucleation, in a sort of modified fragmentation process.

4.4.2 Model limitations and potential improvements

Transient spikes. In the results presented in Subsection 4.3.2, the behavior of our model is not entirely satisfactory, even in terms of qualitative agreement. In particular, the spiking observed in the simulations is not transient but sustained. In the experiments however, the spike trains are very brief and isolated from each other (Figure 4.6). This is a sign that our model, even though it captures the possibility of spiking, is missing a key phenomenon. This transient spiking is reminiscent of the concept of transient chaos, in particular in the context of closed chemical systems [Scott et al., 1991]. In fact, the model presented in [Scott et al., 1991] was an inspiration for our model of H190A oligomers, specifically the depolymerization scheme. The fact that this simple kinetic model presents bursts of transient chaos is a good indication that our model is close to exhibiting this behavior, and might even do so under parameter configurations that we have not explored yet. The problem is that our model is too complex to be studied analytically in as much depth as [Scott et al., 1991].

Hypothesis support and parameter fitting. Many hypotheses were made in the conception of the model, but few of them are supported by experimental evidence. In particular, we have no proof that S elements act as pedestals for E extensions to grow, and that these extensions grow by addition of monomer pairs. These mechanistic hypotheses

could potentially be confirmed by in-depth analysis of AFM images of $P1$ oligomers. So far these images have only been used qualitatively or as illustrations. However, using algorithmic segmentation and image processing tools would allow us to build statistical datasets from these images. Multiple images in different conditions and at different timepoints would then lead to detailed physico-chemical information (size of particles, interactions between particles, types of elements) which is not otherwise available. This project is ongoing, and was started during Thomas Pierron de Mondesir's internship in our team (Spring 2020).

Oligomerization conditions. As we mentioned in Section 4.3, the oligomerization behavior of our model is not satisfactory. In particular, the shape of the size-distribution obtained after 5 hours of growth does not resemble the one observed experimentally (see Figure 4.3 and Figure 4.8). Directly related to this issue is the fact that the monomer pool is almost entirely depleted during the first few minutes in our simulations, whereas in the experiments, the chromatography shows that there is still a large proportion of monomers in the system even after 10 minutes. This might be a problem of parameter choice, but it could mean that we are missing essential kinetic properties in our scheme. Recall that our model was built using simple reactions and non-linearities. In reality, biology involves complex enzyme catalyses which are often represented with activation functions or sigmoids. Before we decide how to improve the model regarding oligomerization conditions, more data will be required, combining multiple chromatograms, SLS measurements and AFM images.

4.4.3 The case of wild-type OvPrP

The problem of $P3$ oligomers. The main reason we chose to focus on H190A is that it only forms $P1$ oligomers. When considering wild-type OvPrP, the formation of $P3$ during oligomerization cannot be dismissed (see Subsection 4.1.1). These oligomers have their own diversity, and examined under AFM they prove to be formed of different coexisting types of elements. Recent experiments studied the depolymerization of $P3$ oligomers isolated from wild-type OvPrP (unpublished data, H. Rezaei). In particular, as opposed to what was stated in previous studies [Eghiaian et al., 2007], the depolymerization of $P3$ assemblies is not complete. Quite the contrary, new and larger assemblies are created during these depolymerization experiments, and these assemblies prove to be $P1$ oligomers. This suggests that $P3$ objects are a precursor of $P1$ objects in the case of wild-type PrP. However, recall that during depolymerization of $P1$, no $P3$ objects are accumulated even when the objects grow larger than initially [Armiento et al., 2017]. This means that $P1$ objects are able to grow and replicate without the need for the intermediate $P3$. The properties of this system are reminiscent of a bi-stable system, and the accumulation of $P3$ objects is attractive only when the system starts from a composition of pure monomers. We have no model that reproduces this behavior yet.

Multiple wavelength SLS measurements. The depolymerization of $P3$ objects revealed an interesting feature of the SLS measurements. Indeed, these experiments were monitored by static light scattering with different lasers simultaneously (purple - $407nm$, blue - $473nm$ and green - $530nm$). Strikingly, the SLS signals at different wavelengths do not seem correlated with each other. In particular, in some cases spikes or drops are capture with one wavelength, whereas the others only reveal a smooth evolution. It is important to keep in mind that scattered light intensity depends on the wavelength λ with a factor λ^{-4} [Hulst and van de Hulst, 1981]. This means that the higher the wavelength, the lower the scattered intensity. More importantly, it means that for large wavelengths, a filtering is applied on the SLS signal such that only the largest contributions are significant enough to be detected. Decorrelation between the signal at a low wavelength (purple) and at a large wavelength (green) potentially indicates that there are changes in the composition of the system which conserve the total order two moment of the distribution, but only changes its variance. This suggests that there is yet another level of diversity and interactions that we have not yet considered in the modeling approach. This data is still under investigation.

4.4.4 Conclusion and perspectives

The work presented in this chapter is still in preliminary stages, since the model is not yet entirely statisfactory and it only provides relatively acceptable qualitative agreement with the data. However, it showcases an important aspect of the modeling approach, which is the model design. Starting off from a few hypotheses and perplexing data, we propose a set of equations and reactions that reproduce some of the features observed in the experiments. Even though the model is not finished yet, it provides insight into the processes the drive OvPrP oligomer replication. It gives us indications of how to find further clues, what experiments could help understanding the system better and what type mechanisms the model should include.

Part II

Yeast prions: multi-scale models of prion propagation

Chapter 5

Introduction to yeast prions

Before presenting our contributions in the field of yeast prions, a detailed introduction is required. Yeast prions are similar to mammalian prions in the general concepts (as introduced in Chapter 1), as they follow the same types of autocatalytic reactions, they exist in different strains and a variety of structures. However the yeast system exhibits specific properties and unique problems, that call for dedicated modeling approaches.

5.1 Biological context and open problems

5.1.1 A versatile system for studying prion processes

Epigenetic memory and bet-hedging strategy. The yeast species *Saccharomyces Cerevisiae* naturally synthesizes about a dozen different proteins that behave like prions [Liebman and Chernoff, 2012]. In yeast, prions are usually not deleterious and it has been suggested that they were selected through evolution for their role in heat-shock adaptation and memory [Chernova et al., 2017]. They allow yeast cells to store information and change their phenotype in a fast and reversible way when faced with extreme conditions. As opposed to genetic changes (mutations), this epigenetic transformation happens in a matter of hours and forms a real bet-hedging strategy for yeast populations.

The scope and extent of yeast prions. Understanding how natural yeast prions are propagated and the chemical processes that drive their replication would advance knowledge in the field of prions in general. It could offer some insight into other self-aggregating mechanisms such as mammalian prions. Further than that, yeast offer a much broader ranger of opportunities to study prions, amyloids and prion-like processes. Indeed, yeast is a highly controlled biological system, one of the first organisms to be fully genetically sequenced, and bio-chemical and genetic engineering are extremely efficient. In particular, yeast cells have been engineered to harbour different self-aggregating proteins, including mammalian proteins involved in neurodegenerative diseases [Chernova et al., 2019]. These artificial systems are useful for drug discovery and testing, and they are much simpler to study *in vivo* than mammals.

The $[PSI^+]$ prion. One prion protein of particular interest, Sup35, causes a simple and detectable phenotypical change in yeast cells when it changes conformation and aggregates. It changes the color of cells from dark red to white, see an illustration in Figure 5.1. This phenotype is termed $[PSI^+]$ (white cells), as opposed to the non-prion phenotype $[psi^-]$ (red cells).[1] The Sup35 protein is a translation release factor, an enzyme involved the recognition of stop-codons. If cells harbour the ade1-14 mutant allele, which contains a premature stop codon, and if Sup35 is functional then the non-sense mutation impairs adenine synthesis. A red intermediate is accumulated and $[psi^-]$ appear red. However, if Sup35 is aggregated in these cells, the non-sense mutation is not detected and adenine synthesis is successful, consequently $[PSI^+]$ cells appear white [Sindi and Serio, 2009]. This property makes the Sup35 prion a very convenient study system, because the aggregation state of the protein is detected by a simple color assay. As mentioned above, yeast synthesize other proteins that behave like prions such as Ure2, associate with the prion phenotype $[URE3]$, and Rnq1, associated with the prion phenotype $[PIN^+]$. Our study focuses on Sup35 and $[PSI^+]$ because it has concentrated the most efforts over the years and offers the most extensive literature.

5.1.2 A multi-scale system

From intra-cellular processes to colony phenotype. One striking difference between mammalian prions and yeast prions is the medium of propagation. Mammalian prions are propagated inside the brain around the neurons, as PrP is extra-cellular. Yeast prions are propagated inside cells that are constantly growing and dividing. The phenotype is indeed transmitted, just like a prion infection may be transmitted, by transfer of aggregated proteins from the mother cell to the daughter cells. Molecular processes of aggregate replication are thus coupled with the cellular mechanisms of growth and division, to create observable phenotypes at the scale of yeast colonies (at least $10^5 - 10^6$

[1] This notation comes from the genetic field, where yeast prions were historically first described as non-Mendeleian phenotypes. An uppercase name and a plus sign indicate the dominant version of the phenotype.

cells), as is illustrated by Figure 5.1.

Prion transmission is asymmetrical. The propagation of aggregates throughout an entire colony relies upon faithful transmission from mother to daughter, but aggregate transmission tends to be biased [Derdowski et al., 2010]. Indeed in experimental conditions, yeast cells are budding. A mother cell grows a bud on its membrane, and transmits some of its inner material (mostly proteins) before the bud detaches and becomes a new cell. This new cell cannot reproduce immediately, it needs to mature in order to become a mother cell whereas a mother cell can form a new bud in a shorter time. The transmission of the prion phenotypes happens at the moment when mother and daughter are connected through the bud-neck. Because of the volume difference between mother and daughter, the extended maturing time for a new daughter cell, and the possible size-threshold directly imposed by the geometry of the bud-neck, the transmission usually favors retention of large aggregates in the mother cell [Derdowski et al., 2010]. This asymmetry has important implications on the phenotype as observed at the scale of colonies. This is one essential aspect of yeast prion biology that needs to be dealt with in detail using mathematical modeling.

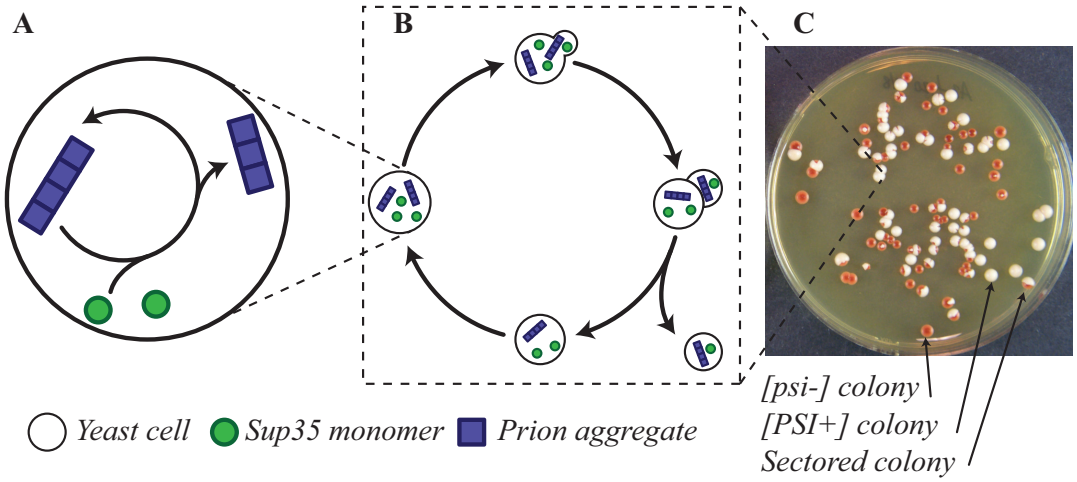

Figure 5.1 – **Interplay between different scales in the yeast prions system.** (A) molecular scale at which the chemical reactions are taking place. (B) Cellular scale with growth and asymmetrical division. (C) Macroscopic scale and phenotype observations (courtesy of T. Serio). Each circle is a yeast colony.

5.1.3 Prion stability and curing

Yeast prions are reversible. Colonies can acquire or loose a prion phenotype following various physico-chemical treatments [Tuite and Cox, 2003]. Experiments that de-stabilize a prion are referred to as "curing" experiments. The study of curing dynamics is a widespread approach to characterize strains. In the case of $[PSI^+]$, strains are qualified

as "strong" or "weak" depending on their resistance to certain treatments [Cox et al., 2007]. This nomenclature correlates with the intensity of the associated phenotype, *i.e.* the color change [Tanaka et al., 2006]. Indeed stronger strains are usually associated with a more contrasted color change of the yeast colonies (they are of a whiter shade). The reversible character of yeast prions contrasts with mammalian prions, since there is no *in vivo* evidence for a potential reversion in the progress of neurodegenerative diseases. It emphasizes how, even though they are similar processes, yeast prions and mammalian prions behave differently at the molecular level. Curing and prion stability are intimately related to cell-to-cell transmission of aggregates. One evidence is that growing colonies may be partially cured of $[PSI^+]$. When a cell looses the phenotype, and thus does not transmit it to its daughters, a whole branch of the colony becomes $[psi^-]$. Such colonies appear as sectored between red and white (sometimes referred to as myriad colonies) [Wegrzyn et al., 2001], as illustrated in Figure 5.1(C).

The role of cellular machinery in prion propagation and stability. One main characteristic of yeast prions is that they interact with many other proteins and chaperones. Indeed, since they are cytoplasmic, they are potential targets and substrates for the cellular machinery. Once again this contrasts with mammalian prions which evolve extra-cellularly. In particular in eukaryotic cells, a whole family of proteins is dedicated to "protein quality control". These chaperones are responsible for dealing with misfolded proteins, and they use different strategies in doing so. They can degrade the misfolded proteins, force them to refold properly or deliver them to other agents that will sequester them [Chen et al., 2011]. Prions are a primary target for this quality control system. In particular the Heat-Shock Protein (Hsp) family, and more precisely chaperones Hsp104, Hsp70 and Hsp90, are crucial in the propagation of yeast prions [Romanova and Chernoff, 2009]. The technical details of their action on prions are presented in Subsection 5.1.4. The main point so far is that they are essential for the faithful propagation of most yeast prions, including $[PSI+]$ [Jones and Tuite, 2005]. Disrupting the chain of action of the Hsp family often leads to de-stabilization of prion phenotypes. This includes introducing point mutations in Hsp-associated genes, modifying gene expression, or treating cells with agents interfering with these chaperones [Wegrzyn et al., 2001]. This leads to either complete or partial curing (sectoring).

GdnHCl-mediated curing and the concept of propagon. One particularly important treatment is Guanidine Hydrochloride (GdnHCl). This chaotropic agent interferes with the fragmentation of aggregates (as we detail in Subsection 5.1.4). It is strongly supported that during GdnHCl treatment, aggregates can no longer increase in numbers [Eaglestone et al., 2000] (remarkably they still increase in size, see Subsection 5.1.4). As such, they get separated in cells when they divide and the colony eventually looses the phenotype and becomes red. Remarkably, there is a number of cells that remain $[PSI^+]$ during GdnHCl treatment and this number reaches a plateau when the experiment runs

for long enough [Cox et al., 2007]. This strongly supports the idea that aggregates have stopped fragmenting and their number is fixed. The final number of $[PSI^+]$ revertants, *i.e.* cells that grow back into $[PSI^+]$ colonies when plated onto medium free of GdnHCl, then corresponds to the number of aggregates initially present in the colony at the start of the experiment [Eaglestone et al., 2000]. This interpretation of the GdnHCl curing experiment is illustrated in Figure 5.2. It led to the definition of the propagon [Cox et al., 2003], as the minimal transmissible entity capable of inducing the change from $[psi^-]$ to $[PSI^+]$. In later studies, the GdnHCl curing was used repeatedly to produce propagon counts, and statistics on these propagon counts are still a primary type of data used in yeast prion biology. We emphasize that this interpretation relies on two hypotheses. First that GdnHCl treatment completely blocks aggregate replication or fragmentation. Second it implies that the transition of a cell from $[PSI^+]$ to $[psi^-]$ corresponds to the threshold between one and zero aggregate. These hypotheses facilitate the interpretation of the experiment in terms of propagon counting (see Subsection 5.2.1), but they are in fact limiting and we question them in Chapter 6.

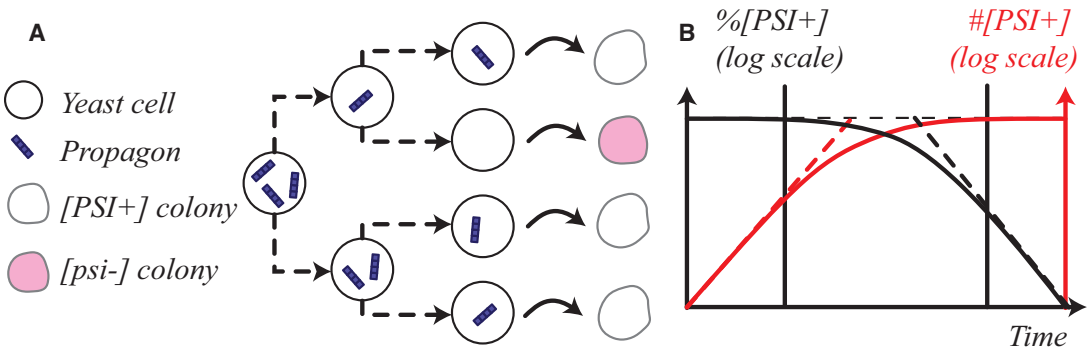

Figure 5.2 – **Classical interpretation of the GdnHCl curing experiment and illustration of the propagon counting.** (A) Under GdnHCl treatment, propagons cannot replicate and are segregated among the cells of the colony as it keeps growing. After about 10 generations, each cell either has one or zero aggregate. (B) The associated curves, with the fraction of $[PSI^+]$ cells in the colony (black), and the number of $[PSI^+]$ cells (red). The latter reaches a plateau, which corresponds to the number of propagons in the founder cell. This is a schematic depiction of experimental curves such as the ones presented in [Cox et al., 2007].

5.1.4 The dual role of Hsp104

Hsp104 mediates aggregate fragmentation. It has been shown that moderate levels of Hsp104 are required to sustain Sup35 prion aggregates, and impairment or knock-out of this chaperone leads to a progressive loss of the $[PSI^+]$ phenotype [Wegrzyn et al., 2001, Park et al., 2012]. The hypothesis commonly accepted is that Hsp104 acts as

a fragmenting agent on Sup35 aggregates by directly withdrawing monomers one at a time along their lengths, breaking the fiber in two parts [Kryndushkin et al., 2003]. This action is led in collaboration chaperones Hsp70 and Hsp40, which act as targetting markers on prion aggregate [Shorter and Lindquist, 2008]. Hsp104 recognizes this marker and brings an energy input, through ATP-hydrolysis, to break hydrogen bonds and extract the targetted monomer [Winkler et al., 2012]. This is the main role of Hsp104 in prion propagation, and it is impaired as soon as the chaperone's ATP-hydrolysis capability is tampered with. This causes the prion phenotype to be eliminated from growing colonies, because the number of aggregates cannot increase anymore, even though they can still increase in size [Ness et al., 2002, Satpute-Krishnan et al., 2007]. This is the case under GdnHCl treatment but also when point mutations are introduced in specific sites of Hsp104's sequence, when Hsp104 is completely deleted (gene knock-out) or when an impaired mutant is over-expressed [Shorter and Lindquist, 2006]. Some of these treatments have slightly different curing dynamics than GdnHCl, but it may be related to the fact that they induce stress. The expression of the Hsp chaperones, and in particular Hsp104, are greatly enhanced by stress (as their primary function is to respond to heat shocks). Over-expressing Hsp104 during these experiments may bias the interpretations, especially considering the point that follows.

The paradox of Hsp104 over-expression. One of the most puzzling result is that over-expression of Hsp104 also cures colonies of the $[PSI^+]$ phenotype [Ness et al., 2017] (this is not true for other yeast prions). However this type of curing follows different dynamics than these obtained by impairing Hsp104, more precisely it happens at a faster rate. It could be argued that this is the result of excessive fragmentation, that would destroy aggregates. Nonetheless, multiple results oppose this idea. It seems that during Hsp104 over-expression, the size of aggregates does not necessarily decrease as would be the consequence of enhanced fragmentation [Kryndushkin et al., 2003]. In fact it has been proposed that in conditions of over-expression, the effect of Hsp104 on Sup35 aggregates is not fragmentation. Different hypotheses are still being tested and the question of Hsp104's role in prion propagation is still an open problem [Greene et al., 2018]. On one hand it has been suggested that elevated levels of Hsp104 can directly "trim" aggregates and destroy them by collaborating with the ubiquitination machinery [Park et al., 2014, Zhao et al., 2017], as inspired by the role of Hsp104 on thermal stress-induced protein amyloids [Bösl et al., 2006]. On the other hand some results indicate that elevated levels of Hsp104 tend to increase the propagation bias of aggregates from mother cell to daughter cell [Ness et al., 2017]. So far neither can be eliminated or confirmed (and they are not exclusive), and no kinetic model can explain both how $[PSI^+]$ is cured by both impairment and over-expression of Hsp104.

The dual role of Hsp104. Overall, the curing experiments combined with various types of data support the idea that Hsp104 plays a dual role in the propagation of $[PSI^+]$.

Structural data revealed two possible interaction modes for Hsp104 with Sup35 aggregates, one "productive" and one "non-productive" [Cox and Tuite, 2018]. The productive mode involves recruitment by Hsp40 and Hsp70, and is the one related to the fragmentation activity of Hsp104. The other binding mode, more stable, does not induce fragmentation, and does not require hydrolysis of Adenosine Triphosphate (ATP) (yet it requires ATP-binding). This role might be related to the effect Hsp104 has on heat-induced misfolded proteins, which is a role of anchoring to the actin skeleton. This would corroborate the idea that in conditions of Hsp104, aggregate transmission from mother to daughter is strongly biased [Ness et al., 2017]. This double role of Hsp104 was also observed *in vitro*, with two different identifiable effects on prion fibril formation [Shorter and Lindquist, 2006]. On one hand Hsp104 reduces the lag-phase (time before observing any aggregated species in the sample), which requires only ATP-binding (similarly as the non-productive binding type). On the other hand it reduces assembly time (time required to convert all the available monomers), but this effect requires ATP-hydrolysis (similarly as the productive binding type). The exact mechanisms of interaction between Hsp104 and Sup35 aggregates are still not precisely understood, and it is the paradox of Hsp104 over-expression curing is controversial in the biologist community.

5.2 Mathematical models of yeast prions

As emphasized in the previous section, the specificities of yeast prions call for modeling approaches and concepts that do not apply to mammalian prions. In particular, the multi-scale aspect and the interplay between molecular mechanism and cell division mechanisms is a crucial feature to consider and investigate. Another particularity is the interaction with chaperones, and their impact on the replication process.

5.2.1 Multi-scale models of prions in dividing cells

Discrete approach and propagon counting. In order to represent how aggregates are distributed between dividing cells, the first approach that was envisioned represented aggregates as discrete entities [Eaglestone et al., 2000, Cox et al., 2003]. Using this description, curing experiments were studied, in particular the GdnHCl curing experiment with the intent to count propagons (see Subsection 5.1.3 and Figure 5.1). Recall that this interpretation lies on two assumptions. First it is assumed that GdnHCl completely inhibits aggregate replication. The second assumption is that a cell looses the $[PSI^+]$ phenotype as soon as it is completely rid of aggregates. Using these two assumptions, coupled with an exponential model of cell growth and division, a simple and tractable model of aggregate propagation during GdnHCl curing was built [Cole et al., 2004]. This model predicts that the number of cells that remain $[PSI^+]$ during curing reaches a limit, which corresponds to the number of propagons in the founder cell of the colony. This model was used extensively to infer propagon counts in yeast colonies following various

treatments and in different growth conditions. However, the numbers predicted were too low as compared to the experiments, and some adjustments were suggested to the model. In particular, adding a bias in mother to daughter transmission aggregates helped increasing the predicted counts [Byrne et al., 2009]. The model was even further improved by introducing a size-threshold for the transmission of aggregates [Derdowski et al., 2010]. Most models describing aggregates as discrete quantities included a stochastic process or a probabilistic approach to represent cell division events [Sindi and Olofsson, 2013]. We emphasize the limitations of discrete models when it comes to studying molecular processes. Indeed such a description does not allow for the use of mass-action kinetics and chemical reaction schemes. They can only deal with empirical laws of evolutions for the aggregates.

Continuous approach and structured population. In order to tackle the multiscale aspect of aggregate propagation in yeast colonies, a continuous approach was also suggested. With this approach, propagon numbers are described as a continuous quantity. Cell populations are described as a density over the propagon number, with multiple compartments representing the different stages of cell maturation and generations. This produces partial differential equations models that are studied analytically [Banks et al., 2016,Banks et al., 2017]. In particular, when the inner "quantity" (the continuous number of propagons) follows a logistic growth law, the solution of the partial differential equation is derived analytically. This allows for a statistical study of propagon counts [Banks et al., 2017]. Even though those models describe propagon counts as a continuous variable, they do not offer the possibility of using mechanistically derived kinetic models. In particular they do not take into account the volume variations of the yeast cells as they grow and divide. Including a logistic growth for the number of propagons is thus still an empirical approach, that is difficult to relate to chemical reactions and kinetic rates. The statistics on those inferred amplification rates are useful because they allow the comparison between different strains for instance, but they are limited to a qualitative interpretation.

5.2.2 Applications of the Nucleated Polymerization model to yeast prions

The Enzyme-Limited Nucleated Polymerization model . The only mathematical model that explicitly investigated the role of Hsp104 in $[PSI^+]$ propagation was introduced in [Davis and Sindi, 2016]. The model is based on the discrete Nucleated Polymerization model (see Subsection 1.2.3). It includes Hsp104 as an additional species, that catalyzes fragmentation of the aggregates. In this model Hsp104 can bind to the links between two monomers in an aggregate. When it is bound, it has a probability of causing the aggregate to fragment. Overall the properties of this model are similar to these of the Nucleated Polymerization model. It is still a global model, with an adjusted value of the basic reproductive number R_0. Interestingly, this model habors novel behavior

that is not supported by the classical Nucleated Polymerization model. It predicts an increase of the mean size of aggregates with the level of monomers production, which is a result observed experimentally [Derdowski et al., 2010]. The model predicts prion de-stabilization by Hsp104 impairment (fragmentation inhibition). It does not predict de-stabilization by over-expression (at least not under reasonable parameter choices), which corroborates the idea that in conditions of Hsp104 over-expression, another effect of the chaperone is at play.

The influence of nucleus size on amyloid clearance. The Enzyme-Limited Nucleated Polymerization model revealed the importance of the nucleus size to differentiate strains. This importance was further investigated and emphasized by [Villali et al., 2020]. These results are based on the use of the classical Nucleated Polymerization model (without explicit modeling of Hsp104), combined to a probabilistic version of this model in order to tackle the case of low aggregate densities. What is referred to as the "persistence model" measures the probability that a single aggregate of minimal size (the nucleus size) injected into a yeast cell succesfully produces a new aggregate larger than the nucleus size before the cell divides. Evaluating this probability allows the authors to evaluate the stability of a prion strain, and to compare the effect of different treatments. They evidence that in order to reproduce experimentally observed differences in Hsp104 over-expression curing of weak and strong strain, these strains must have different nucleus sizes. The weak strain, having a larger nucleus size, is more susceptible to destabilization by enhanced fragmentation, even though it has a lower fragmentation rate in normal conditions. The explanation is that the persistence model predicts that a seed is more likely to be fragmented before it can grow enough to form a second seed. The authors provide experimental observations of aggregate size-distributions that support the idea that the weak strain has a larger minimal stable aggregate size. The conclusions drawn from the results are interpreted in the context of the Nucleated Polymerization model. The problem of the global stability of the Nucleated Polymerization model is avoided by considering a probabilistic model for low aggregate densities.

The models introduced above are specific to yeast prions, in that they tackle one aspect of their propagation that is unique. Two main characteristics of yeast prions call for specific modeling efforts. On one hand the multi-scale interactions between molecular processes and cellular division are difficult to tackle and extremeley important regarding prion stability. On the other hand, the effect of cellular chaperones is essential and complex, and requires building dedicated kinetic schemes. Our contributions to this field in Chapter 6 fit in context, as we investigate prion stability and transmission using a multi-scale framework.

Chapter 6

Using impulsive differential equations to model yeast prions

Chapter 6 is adapted from published work [Lemarre et al., 2020]

We introduced the specificities and open problems related to yeast prions in Chapter 5. The main aspect that calls for specific modeling approaches is the multi-scale interplay between molecular processes and cellular division. We propose an attempt at tackling this problem by introducing a novel framework in the field of yeast prions. We then use this framework to build a minimal yet functional model of the propagation of $[PSI^+]$.

6.1 Introducing a multi-scale model of yeast prions

6.1.1 A novel framework: modeling budding yeast with impulsions

Theoretical framework. We use impulsive differential equations in order to model the cellular processes of yeast colony growth, and their effects upon the intra-cellular

contents. In order to define an impulsive system, we define a sequence of systems of ordinary differential equations $\frac{dZ}{dt} = F_k(Z,t)$ for $k \in \mathbb{R}^n$ and $Z \in \mathbb{R}^n$, along with an initial condition $Z_0 \in \mathbb{R}^n$. Given a sequence $(t_k)_{k\in\mathbb{N}}$ of time points, and a sequence of functions $(G_k)_{k\in\mathbb{N}}$, we define the impulsive system

$$\begin{cases} \frac{dZ}{dt} = F_k(Z,t), & \text{for } t_k \leq t < t_{k+1}, k \in \mathbb{N} \\ Z(t_k^+) - Z(t_k^-) = G_k\big(Z(t_k^-)\big), & k \in \mathbb{N}^*, \\ Z(0) = Z_0. \end{cases}$$

The solution to this system, if it exists, is a piece-wise continuous function Z on $]t_k, t_{k+1}]$ for $k \in \mathbb{N}$ (we assume $t_0 = 0$ with no loss of generality). This requires that the sequence of impulse moments $(t_k)_k$ is strictly increasing, and $\lim_{k\to\infty} t_k = \infty$. Existence, uniqueness and asymptotic behavior of these solutions is studied in the general case [Lakshmikanthanm et al., 1989, Samoilenko and Perestyuk, 1995], and depends on the regularity of the impulsion functions G_k. One important criterion is injectivity of the functions G_k so as to prevent the crossing of different solutions in phase space. Different cases may be studied, where the impulse moments are random, or depend on the state of the system (state-dependent impulsive differential equations) [Stamova, 2009]. Specific asymptotic properties are more readily obtained in the case of a periodic system (in terms of impulsion index k) [Bainov and Simeonov, 1993]. These equations are used in various fields, including population dynamics (where they are combined with delay equations) [Liu and Takeuchi, 2007], epidemiology [Gao et al., 2007], and more recently cell-fate determination [Girel and Crauste, 2018].

Application of impulsions to the case of dividing yeast. In the case of yeast prions, the trajectory Z represents the concentrations of internal material we are tracking in the cells. The systems of ordinary differential equations as defined by $(F_k)_k$ contain the kinetic information about the molecular processes at play. They also include the physical effects of cell volume variations on the internal concentrations. The impulse moments $(t_k)_k$ indicate the cell division events, and the functions G_k model the effect of cell division on the internal content, the transmission bias. Given the asymmetry of yeast budding, two types of biases are possible. First in the cell growth parameters depending on if the cell is a mother or a daughter, which will affect the system F_k. Secondly in the function G_k, which represents the transmission bias at division k. One sequence of impulsions $(t_k, F_k, G_k)_k$ represents one lineage in the colony. At each impulsion the cell can either be a mother or a daughter. If we track all possible lineages starting from one initial cell, the whole colony is modeled.

Exponential growth and asymmetrical division. We use the following model of yeast budding, which is illustrated in Figure 6.1. Cells are exponentially growing at a constant rate which depends only on whether they are mothers or newborn daughters.

This assumption is reasonable in terms of biology since in experiments cells are kept at sufficient nutrient levels so that they are growing exponentially. The difference in doubling times between mothers and daughters is measured experimentally [Satpute-Krishnan et al., 2007], and the cell-to-cell variations in these division times can be neglected in a first approximation. Cells divide as soon as they reach the maturity volume V_0. A division event produces a newborn daughter and a mother. The asymmetry is reflected in the volume of these cells. The mother cell conserves a fraction π of its volume, and the daughter is born with a fraction $1-\pi$. Experimentally, this ratio is known to be approximately $\pi = 0.6$ [Byrne et al., 2009]. After the division, both cells grow until they reach the volume V_0 again, the mother grows at rate γ_M and the daughter at rate γ_D. Since cells are growing exponentially and the maturity volume is fixed, the doubling times for mother and daughter, T_M, and T_D respectively, are constrained by the following relations

$$e^{-\gamma_M T_M} = \pi, \tag{6.1}$$

$$e^{-\gamma_D T_D} = 1-\pi. \tag{6.2}$$

In practice, the doubling times T_M and T_D are measured experimentally [Satpute-Krishnan et al., 2007], as well as the volume ratio after division [Byrne et al., 2009], which allows us to define the growth rates using the above relations. With this simple model of yeast budding we set up an impulsive system, where each impulsion is of duration T_M or T_D depending the type of the cell, and the growth rate γ_M or γ_D is included in the ordinary differential system as a dilution term.

Transmission bias from mother to daughter. In order to establish a complete impulsive system, we must define the transmission bias at the moment of division. Recall that the quantities we are tracking are concentrations, which means they are affected by the variation in volume. Consider a mother cell which is about to divide (volume V_0), and an internal component of mass M_0. The concentration in the mother cell is thus $C_0 = \dfrac{M_0}{V_0}$. Without transmission bias, the internal contents are diffused rapidly between mother and daughter before they are separated. In this case the contents are distributed with the same ratios as the volumes and the concentration is unchanged. We introduce a bias ε in this transmission, considering that the mother cell retains a mass $M_M = (\pi+\varepsilon)M_0$ and the daughter receives $M_D = (1-\pi-\varepsilon)M_0$. In order to ensure that mass remains positive, we require

$$-\pi < \varepsilon < 1-\pi.$$

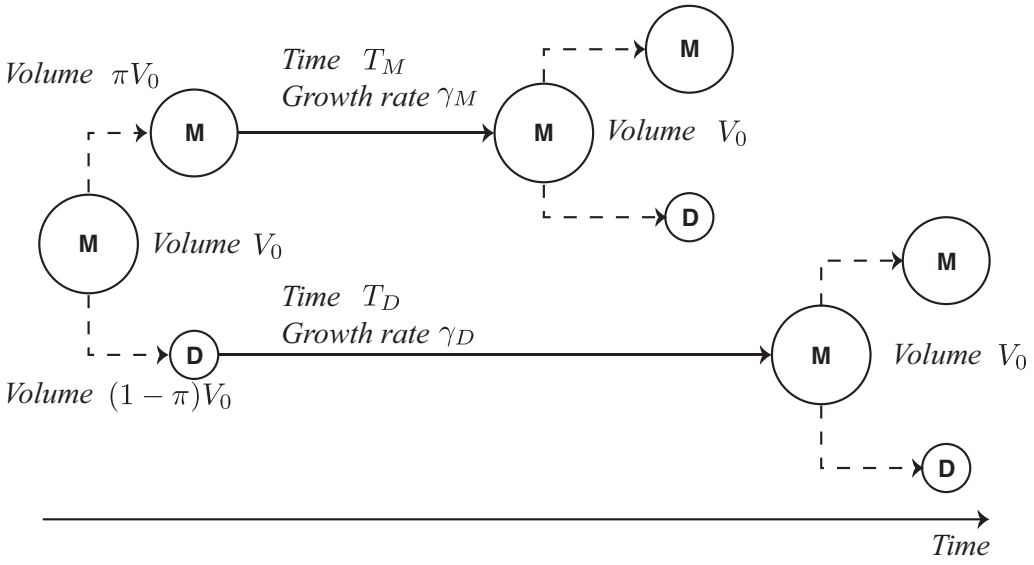

Figure 6.1 – **Illustration of the model used for yeast budding.** Cells are exponentially growing and divide when they reach the volume V_0. Division is assumed to be asymmetric, and a mother cell conserves a fraction π of its volume after division.

The concentration of internal contents in the mother cell and daughter cell after the division are thus

$$\begin{aligned} C_M =& (1+\alpha_M)C_0, \\ C_D =& (1+\alpha_D)C_0, \\ \text{where } \alpha_M =& \frac{\varepsilon}{\pi},\ \alpha_D = -\frac{\varepsilon}{1-\pi}. \end{aligned}$$

We do not consider the cases $\varepsilon = -\pi$ or $\varepsilon = 1-\pi$ which correspond to (respectively) full or null transmission from mother to daughter. The bias ε may depend on the chemical species considered, but it is assumed to be constant in time. With all these elements defined, we establish the impulsive differential equation system

$$\begin{cases} \dfrac{dZ}{dt} = F_k(Z,t), & \text{for } t_k \leq t < t_k + T_k, k \in \mathbb{N} \\ Z(t_k^+) - Z(t_k^-) = \alpha_k \cdot Z(t_k^-), & k \in \mathbb{N}^*, \\ Z(0) = Z_0. \end{cases}$$

By extension α_k denotes the vector of biases (one for each species considered in Z). At each impulsion k, the cell is either a mother M or a daughter D. The parameters are chosen accrodingly, for instance if the cell is a mother then $T_k = T_M$ (doubling

time), $F_k = F_M$ (kinetic system) and $\alpha_k = \alpha_M$ (transmission bias), and vice-versa for a daughter. With this definition of the impulsion functions (and the constraints on ε) and if the ordinary differential systems are well-posed, existence and uniqueness of solutions is ensured [Samoilenko and Perestyuk, 1995]. Note that the description of internal contents and the kinetic equations that drive their evolution are not specified yet, with the only assumption that we have defined a system of equations for mother cells and a system of equations for daughter cells.

6.1.2 Intra-cellular model of prion propagation

A bi-stable model of aggregate replication. We now introduce a model for the internal contents of cells in order to represent the propagation of the $[PSI^+]$ phenotype. In each yeast cell we track the concentration of soluble Sup35 (V) and the concentration of Sup35 aggregates (S). We do not give a size-structure to the aggregates for simplicity. The monomers are produced with a constant rate λ. Monomers and aggregates are diluted with rate γ which corresponds to the growth rate of the cell (depending on the type of cell). We assume there is no degradation of Sup35 (either soluble or aggregated) by the cells, which is acceptable as long the time scale of the simulations stays in the order of magnitude of its half-life (9.6 hours [Christiano et al., 2014]). Finally the aggregates replicate by interacting with monomers at a maximal rate ρ and with a non-linear efficiency. The efficiency is defined by a Hill function of threshold K and cooperativity order $n > 1$

$$f(S) = \frac{S^n}{K^n + S^n}.$$

The corresponding system of ordinary differential equations is given by

$$\begin{cases} \dfrac{dV}{dt} = \lambda - \gamma V - \rho V f(S), \\ \dfrac{dS}{dt} = \rho V f(S) - \gamma S. \end{cases} \tag{6.3}$$

The concentration-dependent replication rate of aggregates is introduced in an empirical way, by choosing a type of sigmoidal functions common in enzyme-ligand reactions [Weiss, 1997]. So far we have no experimentally supported justification for this term, but it means that the secondary nucleation is a cooperative reaction. Aggregates do not catalyze the formation of new aggregates unless the concentration is above the threshold K. Furthermore, when the concentration of aggregates is above the threshold the reaction saturates and the kinetic order becomes one, it only depends on the concentration of available monomers. We have no mechanistic justification for this hypothesis (see also Subsection 6.3.1), however it is essential in order to reproduce experimental results. More specifically the non-linear efficiency at low densities is necessary, as we detail in

Section 6.2.

Equilibrium analysis. Before combining the different scales of the model, we conduct an equilibrium analysis of the kinetic system in the absence of impulsions.

Lemma 6.1. *The disease-free equilibrium* $(V, S) = \left(\frac{\lambda}{\gamma}, 0\right)$ *exists for any choice of positive parameters. It is locally stable as long as* $f(0) = f'(0) = 0$. *In particular it is locally stable if* f *is a Hill function of order* $n > 1$.

Proof. The jacobian matrix at this point is written as

$$\mathcal{J}\left(\frac{\lambda}{\gamma}, 0\right) = \begin{pmatrix} -\gamma - \rho f(0) & -\rho\frac{\lambda}{\gamma} f'(0) \\ \rho f(0) & \rho\frac{\lambda}{\gamma} f'(0) - \gamma \end{pmatrix}.$$

When f verifies $f(0) = f'(0) = 0$, this matrix has a double eigenvalue $(-\gamma)$. If $f(S) = \frac{S^n}{K^n + S^n}$ and $n > 1$, then $f'(S) = \frac{n}{S} f(S)(1 - f(S))$ and so $f(0) = f'(0) = 0$. □

Lemma 6.2. *Suppose* f *verifies the following assumptions*

- f *is non-negative and strictly increasing on* $\mathbb{R}_+$,
- f *has at most one inflection point,*
- $f(0) = f'(0) = 0$.

then there exists at most two steady-states with non-zero aggregate concentrations $0 < S_1 < S_2 < \frac{\lambda}{\gamma}$, *and soluble Sup35 concentrations* $V_1 = \frac{\lambda}{\gamma} - S_1$ *and* $V_2 = \frac{\lambda}{\gamma} - S_2$. *When they exist,* S_1 *is unstable and* S_2 *is locally stable. In particular this is true when* f *is a Hill function of order* $n > 1$.

Proof. The steady-state conditions lead to $V + S = \frac{\lambda}{\gamma}$ and

$$\rho f(S)\left(\frac{\lambda}{\gamma} - S\right) = \gamma S.$$

This is similar to the proof led in Lemma 3.2. Define $H(S) = \rho f(S)\left(\frac{\lambda}{\gamma} - S\right)$ and notice that the assumptions on f impose that $H(0) = H'(0) = H\left(\frac{\lambda}{\gamma}\right) = 0$. Furthermore, $H(S) > 0$ for $S \in]0, \frac{\lambda}{\gamma}[$ and H admits a unique maximum point on this interval (because f is strictly increasing). Since f admits at most one inflection point, it is also the case for H on the interval $]0, \frac{\lambda}{\gamma}[$. Overall, a geometric argument shows that the curve $H(S)$

and the line γS cross at most two times for $S \in]0, \frac{\lambda}{\gamma}[$. The specific conditions (existence conditions for the equilibria) are not analytically tractable for general values of $n > 1$.

However if two solutions exist $0 < S_1 < S_2 < \frac{\lambda}{\gamma}$, their linear stability is given. Indeed we have $H'(S_1) > \gamma$ and $H'(S_2) < \gamma$ (because H starts with a horizontal tangent in 0). The jacobian matrix at either of these points is written as

$$\mathcal{J}(V_{1,2}, S_{1,2}) = \begin{pmatrix} -\gamma - \rho f(S_{1,2}) & -\rho V_{1,2} f'(S_{1,2}) \\ \rho f(S_{1,2}) & \rho V_{1,2} f'(S_{1,2}) - \gamma \end{pmatrix}.$$

After some rearrangements, and using $H'(S) = \rho f'(S)\Big(\frac{\lambda}{\gamma} - S\Big) - \rho f(S)$, the characteristic polynomial of this matrix is written as

$$\chi^2 + \chi\big(2\gamma - H'(S_{1,2})\big) + \gamma\big(\gamma - H'(S_{1,2})\big).$$

This shows that S_1 is associated with an unstable equilibrium since $H'(S_1) > \gamma$ (the jacobian matrix always has an eigenvalue of positive real part). Similarly we have both $H'(S_2) < \gamma$ and $H'(S_2) < 2\gamma$ so S_2 is associated with a locally stable equilibrium. □

The system is bi-stable, with a prion-free equilibrium that exists and is locally stable under any choice of positive parameters. Two other equilibria appear with a saddle-node bifurcation, the one associated with a higher aggregate concentration S is locally stable and the other one is unstable. This is illustrated by a phase-plan diagram in Figure 6.2. It means that the outcome of the system depends on the initial conditions. This bi-stability is crucial for the study of curing experiments in the context of yeast prions, and it is transposed to the system with impulsions.

Remark. *Without considering protein degradation, the total mass of protein in the system $M = V + S$ follows a simple differential equation $\frac{dM}{dt} = \lambda - \gamma M$. The analytical solution to this equation given an initial condition $M(0)$ is $M(t) = \frac{\lambda}{\gamma} + \Big(M(0) - \frac{\lambda}{\gamma}\Big)e^{-\gamma t}$ for $t > 0$.*

6.1.3 The full model and preliminary results

Model formulation. Subsection 6.1.2 introduced all the constituents of our multi-scale model, we now establish the full formulation. In each cell, we track the Sup35 monomer concentration V and the aggregate concentration S. Between cell divisions, these chemicals evolve following the system of equations (6.3), where the parameter γ depends on the type of cell considered (it is either γ_M or γ_D). At each division event we consider that monomers are transmitted wihtout bias from mother to daughter, and aggregates

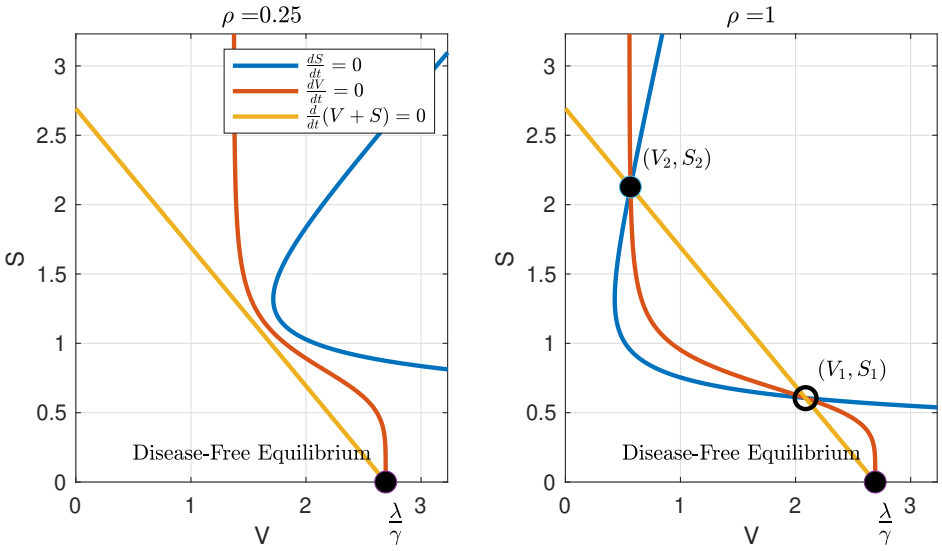

Figure 6.2 – **Phase-plan diagram for the bi-stable model of aggregate replication.** The parameters used are specified in Table 6.1 (with the choice $\gamma = \gamma_M$), and ρ is set to 0.25 (left) or 1 (right). A filled circle indicates a locally stable equilibrium and an empty circle indicates an unstable equilibrium.

are transmitted with a bias $\varepsilon > 0$ (favoring retention in the mother cell). By convention and wihtout loss of generality, the first impulsion is always taken as a mother cell that is about to divide and contains the inner material $V_0 > 0, S_0 > 0$. The whole impulsive system is written as

$$\begin{cases} \dfrac{dV}{dt}(t) = \lambda - \gamma_k V - \rho V f(S), \text{ for } t_k \leq t < t_{k+1}, \\ \dfrac{dS}{dt}(t) = \rho V f(S) - \gamma_k S, \text{ for } 0 \leq t < t_{k+1}, \\ V(t_k^+) = V(t_k^-), k \in \mathbb{N}^*, \\ S(t_k^+) = (1+\alpha_k) S(t_k^-), k \in \mathbb{N}^*, \\ V(0) = V_0, \\ S(0) = S_0. \end{cases} \tag{6.4}$$

Given the simple form of the impulsion functions (linear functions) and well-posedness of the ordinary differential equations system, this problem admits a unique solution [Samoilenko and Perestyuk, 1995]. Furthermore it is straightforward to verify that for positive initial conditions, the trajectory remains in the positive quadrant. The parameter values used in the simulations are detailed in Table 6.1. Biological data gives us estimates for the doubling times $T_M \approx 2hr$ and $T_D \approx 3hr$ [Satpute-Krishnan et al., 2007] and the

Table 6.1 – **Parameter definitions and values used for numerical simulations in the impulsive differential equation model of yeast prions** (6.4)**.** *: [Satpute-Krishnan et al., 2007].†: [Byrne et al., 2009].‡: [Ho et al., 2018]

Parameter	Value	Unit	Description
T_M	2^*	hr	Mother doubling time
T_D	3^*	hr	Daughter doubling time
π	$0.6^\dagger$	-	Mother/daughter volume ratio
ε	0.1	-	Mass transmission bias
α_M	$\frac{\varepsilon}{\pi}$	-	Mother concentration bias
α_D	$-\frac{\varepsilon}{1-\pi}$	-	Daughter concentration bias
γ_M	$-\frac{1}{T_M}\ln(\pi) = 0.26$	hr^{-1}	Mother growth rate
γ_D	$-\frac{1}{T_D}\ln(1-\pi) = 0.31$	hr^{-1}	Daughter growth rate
λ	$0.7^\ddagger$	$\mu M.\text{hr}^{-1}$	Sup35 monomer basal production rate
ρ	10	hr^{-1}	Maximal aggregate replication rate
K	1	μM	Replication efficiency threshold
n	5	-	Replication efficiency order

volume ratio after division $\pi = 0.6$. The prion-free concentration of soluble Sup35 is evaluated at $\frac{\lambda}{\gamma} = 2.5\mu M$ [Ho et al., 2018]. The transmission bias is set at $\varepsilon = 0.1$. The replication efficiency threshold is set at $K = 1\mu M$ and the order of cooperativity is set at $n = 5$. These values are chosen empirically in order to illustrate the qualitative behavior of the model. Finally, the maximal replciation rate ρ is used as an exploration parameter to study the model.

The periodic system and asymptotic behavior: a bi-stable impulsive system. In order to gain insight on the asymptotic behavior of the full impulsive system, it is fruitful to simplify the problem by considering periodic impulsions. This corresponds to studying periodic lineages in the colony. This is particularly interesting for the two extreme lineages, mother-only and daughter-only, as their behavior provides information on the whole colony. Consider one of these lineages, with γ, T and α fixed and the impulsion moments given by $t_k = kT, k \in \mathbb{N}$.

$$\begin{cases} \frac{dV}{dt}(t) = \lambda - \gamma V - \rho V f(S), \text{ for } kT \leq t < (k+1)T, \\ \frac{dS}{dt}(t) = \rho V f(S) - \gamma S, \text{ for } 0 \leq t < t_{k+1}, \\ V(kT^+) = V(kT^-), k \in \mathbb{N}^*, \\ S(kT^+) = (1+\alpha)S(kT^-), k \in \mathbb{N}^*, \\ V(0) = V_0, \\ S(0) = S_0. \end{cases} \tag{6.5}$$

Since the system is periodic, it is relevant to look for periodic solutions. The behavior of this system is analogous to that of the non-impulsive case, although we do not yet have a mathematical proof of this statement. The following results are based on numerical evidence. We conjecture that the periodic system is bi-stable with a locally stable prion-free solution, and two other periodic solution that appear with a saddle-node bifurcation. One of them is locally stable, the other is unstable. The constant solution $V(t) = \frac{\lambda}{\gamma}, S(t) = 0$ is the analog of the disease-free equilibrum. Its local stability relies on the properties of the non-impulsive system, and more particularly the properties of f, namely $f(0)$ and $f'(0) = 0$. The two other periodic solutions are found numerically using the following property.

Lemma 6.3. *The solution $(V(t), S(t))$ for $t \in [0, T]$ of the ordinary differential system in (6.5) is a periodic solution of the full impulsive system if and only if the following equations are verified:*

$$V(0) + \frac{1/(1+\alpha) - e^{-\gamma T}}{1 - e^{-\gamma T}} S(0) = \frac{\lambda}{\gamma},$$
$$V(T) + \frac{1 - (1+\alpha)e^{-\gamma T}}{1 - e^{-\gamma T}} S(T) = \frac{\lambda}{\gamma}.$$

Proof. The equivalence relies on the evolution of the mass $M(t) = V(t) + S(t)$. Recall that $\frac{dM}{dt} = \lambda - \gamma M$, and so we have

$$M(T) = \frac{\lambda}{\gamma} + \Big(M(0) - \frac{\lambda}{\gamma}\Big)e^{-\gamma T}.$$

Suppose (V, S) is a periodic solution, then $V(T) = V(0)$ and $S(0) = (1+\alpha)S(T)$. The equation on the mass expressed in terms of $(V(0), S(0))$ only or in terms of $(V(T), S(T))$ only gives the two relations from the Lemma. Reciprocally, suppose (V, S) is a solution of the ordinary differential system that verifies the linear relations in the Lemma. Using the same equation on the mass $M(T) = \frac{\lambda}{\gamma} + \Big(M(0) - \frac{\lambda}{\gamma}\Big)e^{-\gamma T}$, expressed either in terms of $(V(0), V(T))$ only or in terms of $(S(0), S(T))$ only, we obtain that $V(0) = V(T)$ and $S(0) = (1+\alpha)S(T)$. □

This result gives a reduced space to numerically investigate the existence of periodic solutions. Indeed it is equivalent to find a periodic solution and to find a solution of the ordinary differential system that joins the two lines in the phase-plan. This allows us to numerically confirm our hypothesis that two non-trivial periodic solutions are possible, and they appear through a saddle-node bifurcation. The phase plan and the numerical approximation of the periodic solutions (for each periodic system) are shown in Figure 6.3.

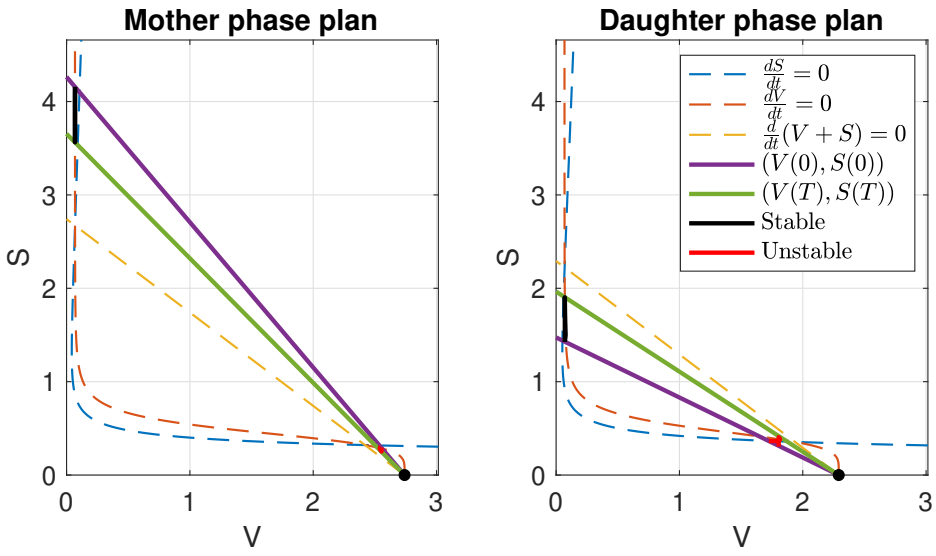

Figure 6.3 – **Phase-plan diagram of the bi-stable periodic systems and periodic solutions.** The two periodic impulsive systems are illustrated, on the left the mother-only system and on the right the daughter-only system. Each diagram shows the nullclines of the differential equation system, as well as the lines that constrain the position of periodic solutions, as given by Lemma 6.3. The periodic solutions of each system are also approximated through numerical exploration and plotted in black (stable periodic solution) or red (unstable periodic solution). The parameters used are described in Table 6.1.

Periodic lineages and full colony behavior. The periodic lineages are two lineages out of an exponentially growing number of cells, yet they provide insight on the behavior of the whole colony. The main reason is that the bias of cell division and aggregate transmission favors aggregate sustaining in mother cells. More precisely, the daughter-only lineage corresponds to the periodic system (6.5) with $\alpha = -\varepsilon/(1-\pi) < 0$ and $\gamma = \gamma_D$. The mother-only lineage corresponds to $\alpha = \varepsilon/\pi > 0$ and $\gamma = \gamma_M$. The transmission bias favors the presence of aggregates in mother cells since $\alpha_D < 0 < \alpha_D$ and the growth rate difference also favors aggregate replication in mothers since $\gamma_M < \gamma_D$ (see Table 6.1). Overall the daughter periodic system is the least favorable for aggregate replication, and the mother periodic system is the most favorable. Using this rationale, three possible outcomes are predicted for the system.

- If the mother-only lineage is $[psi^-]$ *i.e.* converges to the prion-free solution, then the whole colony also grows to be $[psi^-]$.
- If the daughter-only lineages is $[PSI^+]$ *i.e.* it converges to the prion periodic solution, then the whole colony is necessarily $[PSI^+]$.

- Intermediate cases where the daughter-only lineage is $[psi^-]$ and the mother-only is $[PSI^+]$ lead to partially $[PSI^+]$ colonies, which we refer to as sectored colonies.

These three different cases are illustrated by full colony simulations in Figure 6.4. Numerically predicting the colony phenotype is possible from simulating only two lineages (instead of an exponentially growing number of lineages as generations progress). This prediction is depicted in Figure 6.5, depending on the state of the founder cell. The different periodic solutions are also shown on this diagram, two periodic solutions for each of both periodic systems (mother-only and daughter-only).

6.2 Numerical results and interpretation

6.2.1 Aggregate replication is limited by a concentration threshold

The phenotype is reversible. In the context of $[PSI^+]$ curing (see Subsection 5.1.3), the reversibility of the prion phenotype is critical. In curing experiments, a yeast cell is scored as $[PSI^+]$ if, when plated onto normal medium (free of any de-stabilizing agent), it grows into a full $[psi^-]$ colony. This is conceptually possible if the phenotype colony indeed depends on the state of Sup35 in the founder cell. This is why our choice of a bi-stable model is inevitable in this framework. With a global model (such as the Nucleated Polymerization model for instance), as long as the initial cell contains a positive concentration of aggregates, it grows into a full $[PSI^+]$ colony. The problem is that with continuous concentration modeling and continuous transmission bias functions, even when replication is suppressed no cell in the colony ever reaches a null aggregate concentration (the concentration follows an exponential dilution process). For our framework to allow curing as a feasible behavior, bi-stability is necessary in the molecular scheme.

The case of sectoring. An interesting feature of curing experiments is that sectored colonies are often observed in the transient phases [Wegrzyn et al., 2001]. Our model exhibits sectoring as an intrinsic feature that emerges from the combination of the mother-daughter bias and the bi-stability of the intracellular kinetic model. Figure 6.5 shows how the behavior of the colony depends on the state of Sup35 in the founder cell. In particular, it shows that if a strain has a reduced replication rate, sectoring becomes a more likely phenomenon. This is consistent with experimental data [Cox et al., 2007], and links molecular parameters with phenotype observations. In the context of our framework and model, a weak strain is a strain with a low value of replication rate ρ, whereas a strong strain has a large value of ρ. The sectoring behavior is often dismissed in curing experiments. Sectored colonies are either counted as half $[PSI^+]$-half $[psi^-]$ or full $[PSI^+]$, [Wegrzyn et al., 2001, Tuite and Cox, 2003]. Our results reveal the importance of this phenomenon and its intimate link with the kinetic dynamics of aggregates, as well as the asymmetry between mothers and daughters.

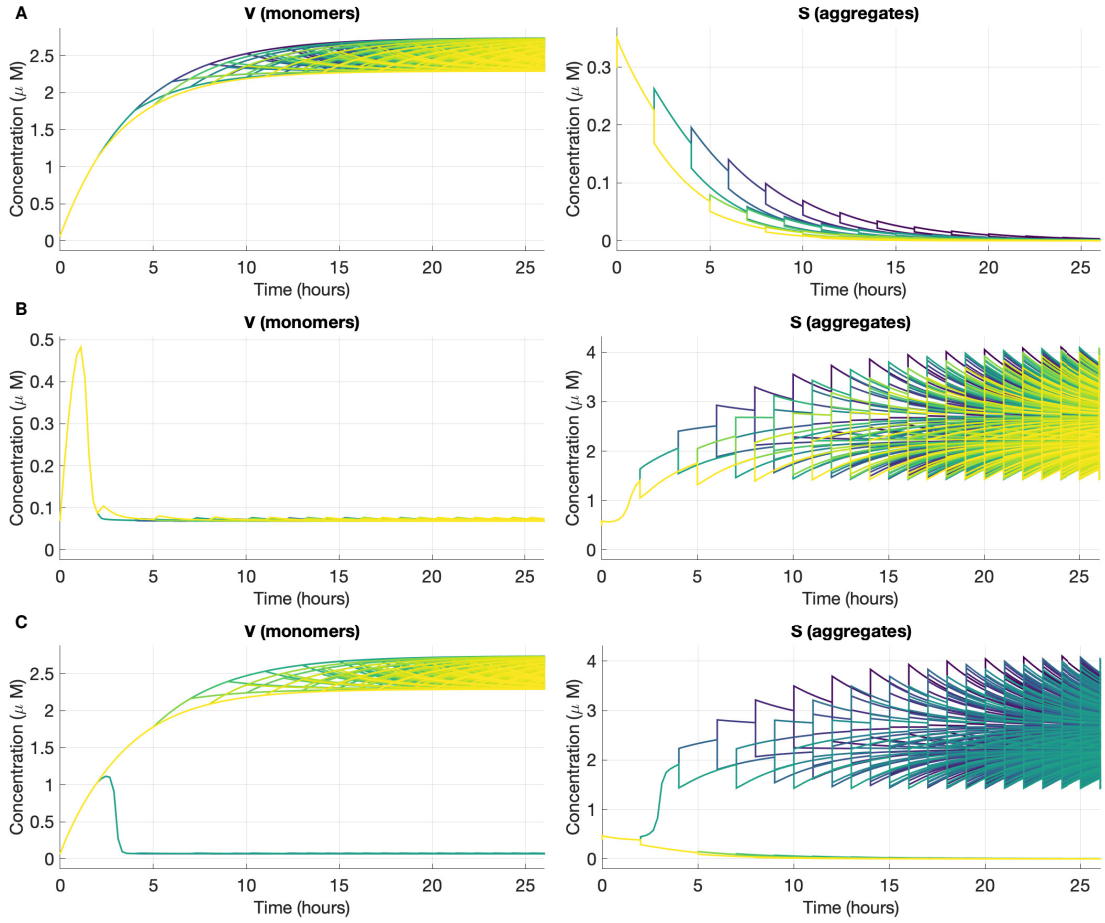

Figure 6.4 – **Simulations of three possible outcomes of the impulsive model for prion propagation.** Evolution of the aggregate S and monomer V concentration for three different initial conditions. Each trajectory shown corresponds to a different lineage. Because cells are dividing the number of trajectories plotted increases in time, as does the number of cells. The trajectories for S and V are shown in the same color for the same cell. The parameters used are described in Table 6.1. The initial conditions used are to be related with the attraction basin showed in Figure 6.5. (A) Completely cured ($[psi^-]$) colony ($V(0) = 0.07\mu M, S(0) = 0.3\mu M$) (B) Full $[PSI^+]$ colony ($V(0) = 0.07\mu M, S(0) = 0.5\mu M$) (C) Sectored colony ($V(0) = 0.07\mu M, S(0) = 0.4\mu M$).

6.2.2 GdnHCl and the concept of propagon

Reproducing the propagon count experiment. The GdnHCl curing experiment (as introduced in Subsection 5.1.3, Subsection 5.2.1 and Figure 5.2) is of particular importance in the field of yeast prions. During GdnHCl treatment, the number of $[PSI^+]$ cells in a colony reaches a plateau [Cox et al., 2007]. Our model reproduces this property

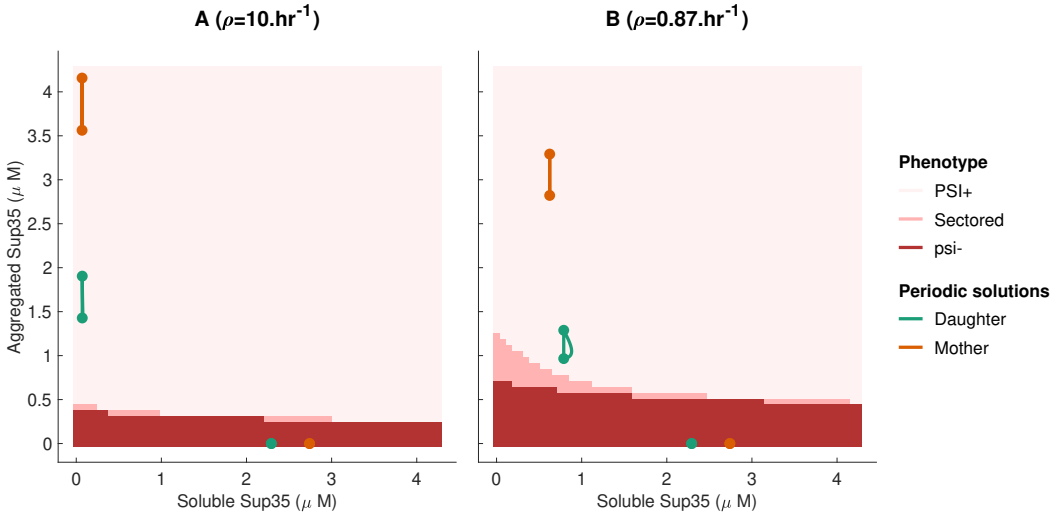

Figure 6.5 – **Predicting colony color phenotype.** Numerical prediction of colony phenotype based on the state of the founder cell, for two different strains. A cell is predicted to be $[psi^-]$ if the mother-only lineage converges to the prion-free solution. If the daughter-only lineage converges to the prion solution, the cell is scored as $[PSI^+]$. If the daughter-only lineage is cured of prion and the mother-only lineage is not, the cell is scored as sectored. The stable periodic solutions for the mother-only and daughter-only solutions are also shown. Each periodic solution is shown as two dots linked together by a trajectory of the differential equation system as well as a vertical line representing the effect of cell division. These elements may overlap due to the scaling. For each system (mother or daughter) a prion-free solution is visible on the horizontal axis, as well as a prion solution in the white region of the diagram. The parameters used for this diagram are described in Table 6.1. Panel (A) shows a strong strain with a maximal replication rate $\rho = 10\text{hr}^{-1}$ and panel (B) is a weak strain with $\rho = 0.87\text{hr}^{-1}$.

under specific parameter choices, as shown in Figure 6.6. In these simulations, cells are scored as $[PSI^+]$ as soon as the concentration of aggregated Sup35 is above a given threshold (we use a scoring threshold of $0.5\mu M$). However the qualitative result does not depend on the scoring method, because we know that a finite number of lineages in the colony are attracted by a solution with a positive concentration of aggregates. All the other lineages are attracted by the prion-free solution. This behavior is possible with our model but only if aggregates continue to replicate in GdnHCl conditions, which strongly contradicts former experimental studies [Eaglestone et al., 2000, Wegrzyn et al., 2001]. The hypothesis that GdnHCl interrupts all chemical activity of aggregates was nuanced in previous experimental work. Indeed it was shown GdnHCl does not stop aggregate growth [Wegrzyn et al., 2001, Ness et al., 2002, Satpute-Krishnan et al., 2007]. Furthermore, [Park et al., 2012] used fluorescent tagging to track aggregates during GdnHCl

treatment, and report a decrease in cells with foci slower than the halving predicted by the segregation hypothesis.

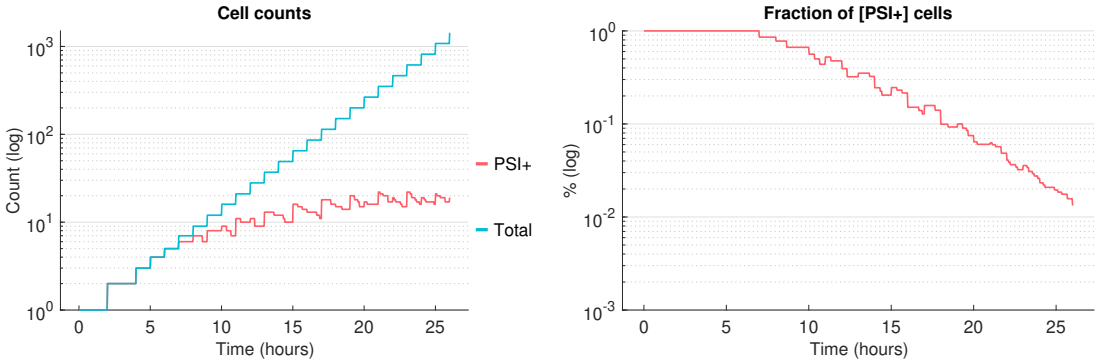

Figure 6.6 – **Reproducing the propagon count experiment with the impulsive model.** Evolution of the $[PSI^+]$ cells count and $[PSI^+]$ proportion simulated by our model, in the case of $\rho = 0.21\text{hr}^{-1}$ (all other parameters as in Table 6.1). Cells are scored as $[PSI^+]$ as soon as they contain a concentration of aggregated Sup35 higher than $0.5\mu M$.

GdnHCl conditions correspond to a very precise choice of parameters. Reproducing the propagon count experiment with our model requires very specific kinetic parameters for the replication reaction. These conditions are found numerically by studying the mother-only lineage in the model. Indeed when this lineage is attracted to the $[PSI^+]$ periodic solution but each of its daughters becomes $[psi^-]$, we are assured that the total number of $[PSI^+]$ cells in the colony reaches a plateau. These conditions are illustrated by Figure 6.7, where the system is initiated close to the periodic solution of the mother-only lineage. Each daughter born from this lineage creates a branch of the colony that looses aggregates and becomes $[psi^-]$. These conditions lead to the cell counts that reproduce the experiments as shown in Figure 6.6. Once again this is the consequence of bi-stability in the molecular model as well as the asymmetric division favoring aggregate retention by mother cells. The fact that thse conditions correspond to a very narrow parameter range is worth emphasizing and discussing further.

6.3 Discussion and perspectives

6.3.1 How to explain the kinetic threshold?

Taking into consideration the case of low aggregate densities. Our results show that the behavior of aggregates at low densities needs to be investigated further. In previous modeling studies (see Subsection 5.2.1) this behavior was usually dismissed, or assumed to be an exponential expansion rate. We suggest a modeling approach that

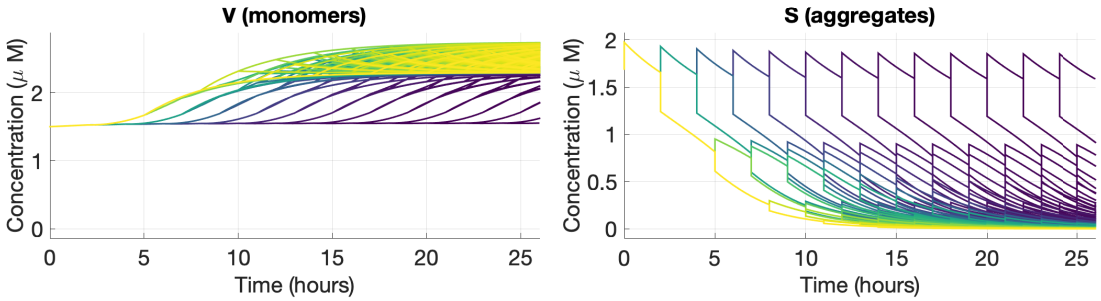

Figure 6.7 – **Simulation of a propagon in GdnHCl curing conditions.** Full colony simulation close to the periodic solution of the mother-only lineage, in the case of $\rho = 0.21\text{hr}^{-1}$ (all other parameters as in Table 6.1).

includes a non-linear reaction rate effective only at low concentrations of aggregates. This could be explained by a cooperative mechanism requiring the presence of multiple aggregates in order to catalyze the formation of a new one. Note that fragmentation is not such a mechanism, even when it is limited by the presence of a chaperone like Hsp104. So far we have no evidence for this type of mechanism other than the mathematical insight provided by our modeling.

A modeling choice. Another approach is possible to investigate the behavior of low densities of aggregates. In these conditions, probabilistic models become more reliable than deterministic models since the hypotheses of the law of mass-action are not strictly verified. This approach is used for instance in [Villali et al., 2020], as developed in Subsection 5.2.2. One interpretation of our model could be that the law of mass-action requires some adjustment in the conditions of low aggregate densities, and the non-linear terms would account for this adjustment.

6.3.2 On the role of GdnHCl and Hsp104, the concept of propagon

An uncovered mechanism? Our results question all previous assumptions made about the effect of GdnHCl. With our model, the propagon experiment is reproduced only if the chemical replication rates are chosen very carefully. This is potentially explained by two reasons. The first is that our model might be too simple to capture the possibilities of the full biological system. This would also explain why sectoring is reduced to such a narrow region in the phenotype map Figure 6.5. A second explanation is that our model may be missing an essential chemical process, which remains unaffected when GdnHCl is present. There is precedent for this assumption, because there is evidence that aggregates are still chemically active under GdnHCl treatment. First GdnHCl does not prevent aggregates from growing by polymerizing newly synthesized Sup35 [Kryndushkin et al., 2003, Satpute-Krishnan et al., 2007]. Furthermore, there is evidence for an action of Hsp104 that is not affected by GdnHCl, see Subsection 5.1.4. This brings up the

controversial question of the roles of Hsp104 in the propagation of $[PSI^+]$ and other yeast prions. The only conclusion our results bring is that GdnHCl curing is not explained by an exponential dilution model as suggested previously [Eaglestone et al., 2000, Byrne et al., 2009], because of the plateau of $[PSI^+]$ cells. Our study is a first step in the design of a more elaborate kinetic model that includes the effect of Hsp104.

Towards a re-definition of the propagon. With the perspective of our modeling framework, the concept of the propagon needs to be adjusted. Instead of defining the propagon as particulate entity, we define it as an asymptotic property of the system. One propagon corresponds to one lineage that remains $[PSI^+]$ in GdnHCl-treatment conditions, when all the subsequent daughters born from this lineage become $[psi^-]$. The number of propagons in a cell is intimately related to the initial state of Sup35 in this cell (at the start of the propagon count experiment). However, this relation is more complex than predicted by the model of random segregation (Figure 5.2). The propagon plateau is influenced by the kinetic replication model (in conditions of GdnHCl treatment), and this makes the interpretation more difficult. Nonetheless it offers the possibility to build a model which reproduces propagon counts more faithfully.

6.3.3 Conclusion and perspectives

We introduced a novel modeling tool to the field of yeast prions, with the major benefit of relating different scales in a controlled and rigorous way. From the molecular mechanisms, with a kinetic scheme built using mass-action kinetics, to the phenotypical traits at the colony level, this framework has the potential of taking into account every aspect of the system. In the case of the $[PSI^+]$ prion, we build a simple model with the primary goal to qualitatively reproduce experimental observations from the literature. We focus on curing experiments, and reproducing any curing experiment with our framework requires introducing a very particular characteristic into the molecular model. The kinetic scheme needs to be bi-stable, where the prion-free state and the prion state are both simultaneously stable, and the transition between the two of them is a bi-stable switch. This allows the possibility of curing, and it concomitantly explains the phenomenon of sectoring in a deterministic way. This phenomenon is often dismissed but is in fact instructive with regards to the molecular processes. By investigating in more detail the case of GdnHCl curing, we have reason to question the suggested effect of this agent. Indeed this experiment is reproduced by our model, but the fragmentation of aggregates must not be completely inhibited contrary to the commonly accepted effect of GdnHCl.

Overall, the framework of impulsive differential equations is versatile and could be adapted to many different cases. Studying the $[PSI^+]$ prion already revealed instructive, even though work is still in progress. In the future, we aim to use this framework to build and validate a complete model of aggregate replication including the role of Hsp104 and possibly its co-chaperones, a size-distribution of aggregates, stochasticity in the cell

division events. This would be done through hypothesis testing and close collaboration with biologists. Inferring parameters is a long-term goal, that first requires understanding the very structure of the molecular processes. In particular, it needs to be clear what is the mechanistic origin of the cooperativity in the replication of aggregates. Another use of the model is to extend it to other yeast prions and amyloid models, as yeast models are used to screen for anti-amyloid drugs, and a specific modeling framework would help interpreting these experiments.

Part III

Neurodegenerative diseases: spatio-temporal models of oligomer propagation

Chapter 7

Introduction to neurodegenerative diseases and their multi-scale propagation

This Part focuses on the investigation of protein misfolding processes in the context of neurodegenerative diseases. These diseases include mammalian prion diseases (see Part I), as well as Alzheimer's Disease (which we focus on in this Part), Parkinson's Disease and Huntington Disease. We are interested in the spatio-temporal evolution of protein misfolding and aggregation, and how they dictate the evolution of the degeneration. This chapter introduces state-of-the art knowledge concerning the propagation of Alzheimer's Disease in the brain, as well as the role of prion-like processes in the pathology. It also presents recent models of spatio-temporal propagation of protein aggregates in the brain.

7.1 Grasping the complexity of Alzheimer's Disease

7.1.1 The amyloid cascade hypothesis

Accumulation of amyloid plaques in the brain is one of the hallmarks of Alzheimer's Disease. These plaques are usually present in the brains of late-stage Alzheimer's patients, and detected upon autopsy. They were first hypothesized to be the main cause of the neurodegeneration, and they were the target of numerous yet unsuccessful therapeutic strategies. The plaques are composed mostly of Aβ protein, which is a protein peptide that results from the cleavage of Amyloid Precursor Protein (APP) by proteases. Depending on the position of the cut, a different length of Aβ is created ranging from 36 to 43 amino acids. The versions most involved in the development of the disease are Aβ40 and Aβ42. These proteins can indeed change conformation and assemble into long fibrils and plaques. The deposition pattern evolves in time on a scale of years and propagates from one region of the brain to another [Thal et al., 2002]. Although the precise involvement of Aβ deposition in neurotoxicity and the onset of symptoms is not clearly understood, it does partially correlate with brain atrophy and neuronal death [Soto, 2003]. This led to the formulation of the amyloid cascade hypothesis [Hardy and Selkoe, 2002].

A prion-like propagation. This dominant hypothesis in the field of Alzheimer's Disease and neurodegenerative diseases considers that the onset of the disease is related to an autocatalytic conformational change of Aβ. The amyloid cascade hypothesis is the theory that the entire pathogenesis is driven by the progressive misconformation and accumulation of Aβ. The very first steps in this process are stochastic and very rare, with multiple factors (genetic, environmental, other diseases) affecting the probability of a spontaneous nucleation happening [Rodrigue et al., 2013]. Once a seed is formed, the accumulation starts by forming small soluble oligomers, leading the way towards longer and more rigid fibrils, which may eventually coalesce into large plaques. Even though the amyloid protein assemblies are not the same as prion aggregates, the mechanisms are similar and the propagation of Aβ assemblies is indeed driven by a secondary nucleation process [Cohen et al., 2013, Olsson et al., 2018]. The amyloid cascade hypothesis had gained considerable support over the past two decades, but it has some limitations and requires some complimentary theories, see Subsection 7.1.3.

7.1.2 The role of structural diversity

From oligomers to plaques. The accumulation of Aβ produces a large range of structures, with different levels of organization and different pathological properties. Therapeutic research first focused on the large plaques because they were most clearly identified signs, but amyloid-clearance strategies have yet to prove successful in reducing the disease progression [Hardy and Selkoe, 2002]. More advanced imaging and bio-chemical characterization techniques allowed the identification of smaller, more soluble, aggre-

gated species formed of Aβ. The propagation of these smaller species in the brain is much more likely than the propagation of large plaques and tangles. It is not clearly understood whether oligomers are an intermediate for the formation of larger plaques or an alternate polymerization pathway [Cohen et al., 2015], but what is now commonly accepted is that they are the most impactful aggregated species in the disease's propagation.

The most toxic species. It is now believed that the most toxic Aβ self-assembled structures are small oligomers [Haass and Selkoe, 2007, Sengupta et al., 2016]. The plaques act as end products of the amyloid formation chain, but are largely immobile and inactive. The smaller species however propagate easily throughout the brain and have a direct toxic effect on the neurons [Dean et al., 2016, Sowade and Jahn, 2017]. Indeed it has been shown that they induce an inflammatory response from neuronal cells [Sondag et al., 2009]. This sheds light onto the importance of structural diversity in the amyloid formation pathway, and how crucial this diversity is in the onset and propagation of the disease. Understanding how different structures are formed and interact between themselves is a foremost problem in the effort against Alzheimer's Disease.

7.1.3 Limitations of the amyloid cascade hypothesis and complimentary theories

Decorrelation between amyloid accumulation and other biomarkers. Beside amyloid deposition, physiological signs of the disease include brain atrophy and intracellular neurofibrillar changes [Braak and Braak, 1991, Jagust and Mormino, 2011]. The associated neurodegeneration leads to cognitive impairment and loss of function in certain regions of the brain, that are not necessarily correlated with the regions affected by amyloid deposition [Rabinovici et al., 2010]. This led to the search of other complimentary mechanisms involved in the progression of the disease.

The role of Tau. Tau is an intracellular protein that is also involved in the progression of Alzheimer's Disease. It self-assembles into large tangles in prion-like manner. It is hypothesized that extracellular accumulation of misfolded Aβ favors the msifolding of intracellular Tau [Bloom, 2014]. Including the action of Tau revealed important to recapitulate some discrepancies between the accumulation of Aβ and the physiological changes associated with neurodegeneration in different parts of the brain. One important characteristic of Tau is that it accumulates intracellularly and can thus be transmitted along synapses. This aspect of Alzheimer's Disease is not considered in our study, but it will have to be taken into account if a full multi-scale model is to be built (see Subsection 8.3.3).

Long range propagation. The propagation of amyloid aggregates from one brain region to another is not attributable to simple diffusion. Indeed the temporal and regional characteristic do not follow a simple diffusive pattern, they rather follow a specific and reproducible order [Braak and Braak, 1991, Hardy and Selkoe, 2002]. This indicates

that long propagation mechanisms are at play, such as exosome transport and axonal propagation. Exosomes are small vesicles or capsules that contain protein material to be transmitted between different neurons. In particular they transport proteins such as Aβ and Tau, and may propagate misconformed protein from one brain region to anohter [Xiao et al., 2017]. Axonal propagation correponds to the transmission of protein along axons (*i.e.* neuronal connections), which is suggested to happen for the transmission of small assemblies of Tau [Braak and Del Tredici, 2011]. This mechanisms is supported by the correlation between regional and temporal patterns of the disease progression and models based on network diffusion, see Subsection 7.2.2.

Alzheimer's Disease results form the complex interactions of different processes, including protein misfolding and self-aggregation, short and long range propagation, inflammatory response and protein quality control. However structural diversity of protein assemblies plays a crucial role in the progression and toxicity of the disease, and models of amyloid processes need to take this aspect into account.

7.2 Spatio-temporal models for the propagation of misfolded proteins in the brain

We introduce here modeling studies that include the effect of spatio-temporal propagation of amyloid aggregates in the progression of Alzheimer's Disease. Our interest lies in the importance of structural diversity, but we are also concerned with the interplay between regional and temporal deposition and the emergence of patterns. Different methods and approcahes are possible to tackle this issue, but the main two are reaction-diffusion equations and network-diffusion models.

7.2.1 Models with structural diversity

Different kinetic models have been suggested to take into account the different structures formed by self-assembly of Aβ. In particular [Webb et al., 2013, Helal et al., 2019]. These models introduced the novel concept of interaction between Aβ and the PrP protein in the context of Alzheimer's Disease, but they also introduced different structures including fibrils, plaques and small oligomers. They do not consider a spatial dimension and the models consist of systems of autonomous ordinary differential equations. In these models, the plaques act as inactive reservoirs where oligomers and fibrils are trapped. Fibrils grow following a polymerization-depolymerization mechanism (which gives a Becker-Döring scheme, see Subsection 1.2.1). Oligomers also grow by polymerizing Aβ monomers, but are stabilized once they reach a critical size.

7.2.2 Reaction-diffusion models

One classical approach that allows studying spatial propagation is the use of reaction-diffusion equations. This was used in the context of a full brain, in two dimensions with

simple diffusion [Bertsch et al., 2017]. This model combines the Smoluchowski equation (fragmentation-coagulation) with size-dependent diffusion. It gives a system of partial differential equations, that is solved numerically on a two-dimensionnal mesh representing a whole brain. In this case the fibrils do not have structural diversity, only one type of assemblies is considered. Different limitations apply to this model, in particular the scales involved. Indeed, Stokes-Einstein diffusion is only applicable to short spatial and time scales. For long range propagation and longer time scales, the brain molecular clutter restricts the application of classical diffusion laws. In those conditions, other processes have to be taken into account such as exosome transport or axonal propagation.

7.2.3 Network diffusion-based models

Another approach, more adapted to larger temporal and spatial scales is the network-diffusion method. In [Raj et al., 2012], a network is built from imaging data of real (healthy) human brains. The connectome is reduced to a graph containing 90 nodes, corresponding to different regions of interest in the brain. This graph is then used to simulate a simple model of exponential growth couple with network-diffusion. Even with a very simple model of molecular processes (not exactly prion-like), the propagation mimics the temporal and regional evolution of actual symptoms such as brain atrophy. This supports the idea that the long range propagation of the neurotoxic agents is mostly driven by the connectome of the brain.

Different approaches have been suggested to study amyloid propagation in the context of Alzheimer's pathogenesis, each specific to certain temporal and spatial scales. To the best of our knowledge, there exists no model which can take into account all the different scales involved, from molecular processes to brain atrophy and degeneration, and link all the processes at play. We propose one contribution in Chapter 8 which focuses on the early stages of the amyloid cascade.

Chapter 8

A spatial model of $A\beta$ oligomers

Chapter 8 is adapted from published work [Andrade-Restrepo et al., 2019]

This chapter is dedicated to the introduction and preliminary study of a spatial model for the propagation of Aβ oligomers. Considering the different scales and processes at play in Alzheimer's Disease and the complexity of their interplay (see Chapter 7), our approach focuses on a restricted setting with the intent to build a robust modeling basis. We consider the early phases of the disease, at the beginning of the amyloid cascade and in the vicinity of a few neurons, and we investigate the influence of diffusion combined with secondary nucleation on the propagation of Aβ oligomers and their toxicity on neurons.

8.1 Introducing a model which combines secondary nucleation and spatial diffusion

8.1.1 Model setting and biological hypotheses

Scope of the model. In the context of the amyloid cascade hypothesis, and with recent discoveries that oligomers play a crucial role in the pathogenesis of Alzheimer's Disease (see Section 7.1), we propose a model that focuses on Aβ oligomers. The scope of the model is necessarily restricted to the vicinity of a few neurons, and time scales of a few hours. With these restrictions, we are entitled to study the propagation of assemblies under the main drive of Stokes-Einstein diffusion and to ignore long range interactions, as well as cyclic effects of the brain metabolism. We place the focus on the early events in the amyloid cascade, after a seed has been formed. The random aspects of the process we ignore, so that we can focus on the impact of deterministic kinetic schemes and secondary nucleation mechanisms. Since the time scale is limited to a few hours, we also neglect the formation of long fibers and plaques. The objects we study are thus fairly small (less than 100 monomers) so we use a discrete size-description.

Molecular scale phenomena. The model tracks the spatio-temporal distribution of the concentration of Aβ and Aβ oligomers, in space x and time t. Normal Aβ monomers, of density $m(x,t)$, are produced by neurons and released through their membrane with a rate λ, and they are cleared from the brain environment with a rate δ. These monomers are captured by proto-oligomers, or non-mature oligomers through a simple polymerization process of rate r_i (depending on the size i of the proto-oligomer). For mathematical reasons, we assume the sequence of polymerization rates $(r_i)_i$ is (non-strictly) increasing. The density of proto-oligomers of size i is denoted by $\mu_i(x,t)$. Monomers are also released from proto-oligomers through depolymerization with a constant rate b. When a proto-oligomer grows above the size threshold $i_0 > 2$, it becomes stable and can no longer vary in size. We refer to this process as oligomerization. Finally, proto-oligomers grow in numbers through a secondary nucleation mechanism which we model as a fragmentation process. In particular we consider a uniform fragmentation process of rate β, and we formulate our equations as a Nucleated Polymerization model (see Subsection 1.2.3) with a nucleus size of 2 and a maximum size of i_0 (oligomer threshold).

Mesoscopic scale. The model evolves in a bounded domain Ω of $\mathbb{R}^2$ of external boundary Γ, in which a N neurons are present. The neurons are represented by disks $\omega_1, \omega_2, \dots, \omega_N$. Each neuron $k = 1 \dots N$ produces Aβ monomers through its membrane $\partial\omega_k$ with a time-dependent $\lambda_k(t)$. Each considered species of size $i = 1 \dots i_0$ diffuses in space with a size-dependent diffusion coefficient D_i. We assume that the smaller the assembly, the faster it diffuses, and the specific scaling of these coefficients is described in Subsection 8.1.2. We assume diffusion is isotropic in the brain (a strong hypothesis since the cerebrospinal fluid is crowded by numerous proteins and structures), which allows us to use two-dimensional

results as a good approximation of three-dimensional properties. Oligomers are assumed to be the toxic species for neurons. Their action is assumed to rely on their presence in the effector zone Σ_k^ε of each neuron k, which is the annulus of radius ε surrounding ω_k. When oligomers are in the vicinity of a neuron, they induce a reduction of the Aβ production rate $\lambda_k(t)$. This models the effect of an inflammatory response or of neuronal death, and we assume it is irreversible. The Aβ monomer production rate of neuron k decreases exponentially fast, with an instantaneous rate that is proportional to the quantity of oligomers present in the annulus Σ_k^ε. This writes as

$$\begin{aligned} \frac{d\lambda_k}{dt} =& -\tau\lambda_k \int_{\Sigma_k^\varepsilon} \mu_{i_0}(x,t)dx, \\ \lambda_k(0) =& \lambda_k^0, \end{aligned} \tag{8.1}$$

where λ_k^0 represents the healthy production rate of Aβ of neuron k (in practice we assume it is the same for all neurons $\lambda^0 > 0$). This is a very simple and pessimistic model of toxicity since there is no possible healing for the neurons. However we have no precise indication of the effect that Aβ oligomers have on neurons so we start with the simplest assumptions. In order to properly define the mathematical formulation of the model, the behavior at the boundaries needs to be specified. Along the neurons we impose non-flux (Neumann) boundary conditions, except for the monomers because the neurons produce Aβ monomers. The domain boundary is dealt with as an absorbing boundary of coefficient γ, which represents loss of mass towards other parts of the brain. This implies that the process starts in the region of interest Ω and then propagates outwards. Another possibility would be to use periodic boundary conditions in order to represent a closed environment in isolation of the rest of the brain. All the processes we detail here are illustrated by Figure 8.1, and the domain definition as well as the geometry of the neurons are described in Figure 8.2. These hypotheses and processes allow us to define the model as a mathematical problem.

8.1.2 Mathematical formulation

Initial formulation as a system of partial differential equations. We introduce the mathematical formulation. Let us first define the following sets

$$\begin{aligned} X =& L^2(0,T:H^1(\Omega)), \\ X_+ =& \{v \in X | v(x,t) \geq 0, a.e.\ (x,t) \in \Omega \times [0,T]\}, \\ V_+ =& \{v \in L^2(\Omega) | v(x) \geq 0,\ a.e.\ x \in \Omega\}. \end{aligned}$$

The processes described in Subsection 8.1.1 are translated into the following partial differential equation problem, which combines a Becker-Döring scheme with a simplified Nucleated Polymerization model (see Section 1.2). We assume all kinetic parameters are

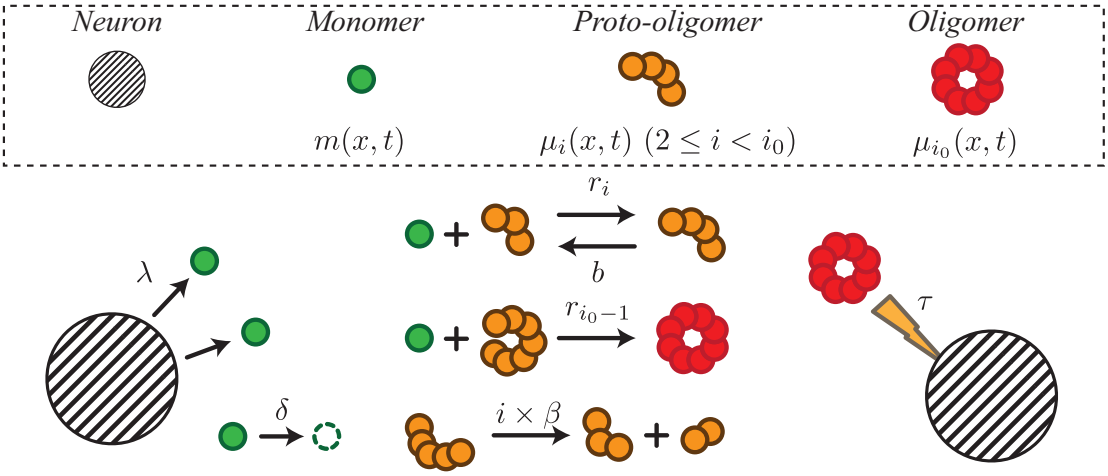

Figure 8.1 – **Biological processes represented in the Aβ oligomer model.** Although it is not illustrated in the scheme, all agents (except neurons) are diffusing in space with a size-dependent diffusivity. All processes illustrated are described in detail in Subsection 8.1.1 and the corresponding mathematical formulation is presented in Subsection 8.1.2.

positive.

Problem 1. *Given initial conditions* $(m^0, \mu_2^0, \dots, \mu_{i_0}^0) \in V_+^{i_0}$ *and* $\lambda^0 > 0$, *find* $(m, \mu_2, \dots, \mu_{i_0})$ *in* $X_+^{i_0}$ *such that*

$$
\begin{aligned}
\frac{\partial m}{\partial t} =& D_1 \Delta m + \sum_{j=3}^{i_0-1} b\mu_j - \sum_{j=2}^{i_0-1} r_j \mu_j m + 2\beta \sum_{j=2}^{i_0-1} \mu_j - \delta m, \\
\frac{\partial \mu_2}{\partial t} =& D_2 \Delta \mu_2 + b\mu_3 - r_2 \mu_2 m - \beta \mu_2 + 2\beta \sum_{j=3}^{i_0-1} \mu_j, \\
\forall i \in \{3, \dots, & i_0 - 2\}, \\
\frac{\partial \mu_i}{\partial t} =& D_i \Delta \mu_i + b\mu_{i+1} - b\mu_i + r_{i-1}\mu_{i-1} m - r_i \mu_i m - \beta(i-1)\mu_i + 2\beta \sum_{j=i+1}^{i_0-1} \mu_j, \\
\frac{\partial \mu_{i_0-1}}{\partial t} =& D_{i_0-1} \Delta \mu_{i_0-1} - b\mu_{i_0-1} + r_{i_0-2}\mu_{i_0-2} m - r_{i_0-1}\mu_{i_0-1} m - \beta(i_0-2)\mu_{i_0-1}, \\
\frac{\partial \mu_{i_0}}{\partial t} =& D_{i_0} \Delta \mu_{i_0} + r_{i_0-1}\mu_{i_0-1} m,
\end{aligned}
\tag{8.2}
$$

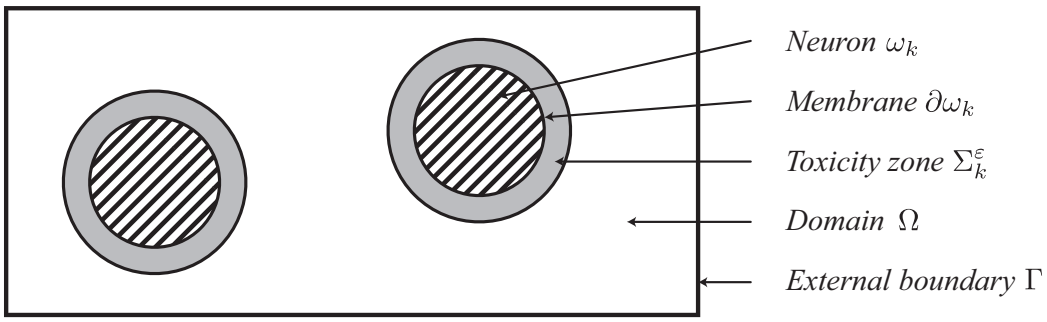

Figure 8.2 – **Domain geometry for the Aβ oligomer model.**

and

$$a.e. x \in \Omega, m(x,0) = m^0(x), \mu_2(x,0) = \mu_2^0(x), \dots, \mu_{i_0}(x,0) = \mu_{i_0}^0(x),$$

with the following boundary conditions on the external boundary Γ *and for each neuron* $k = 1 \dots N$

$$\begin{aligned} i = 2, \dots, i_0, D_i \frac{\partial \mu_i}{\partial \nu} &= -\gamma \mu_i \ \textit{on}\ \Gamma, \\ i = 2, \dots, i_0, D_i \frac{\partial \mu_i}{\partial \nu} &= 0 \ \textit{on}\ \partial\omega_k, \\ D_1 \frac{\partial m}{\partial \nu} &= -\gamma m \ \textit{on}\ \Gamma, \\ D_1 \frac{\partial m}{\partial \nu} &= \lambda_k(t) \ \textit{on}\ \partial\omega_k. \end{aligned} \tag{8.3}$$

The source term λ_k *of neuron* k *follows the differential equation*

$$\begin{aligned} \frac{d\lambda_k}{dt}(t) &= -\tau \lambda_k \int_{\Sigma_k^\varepsilon} \mu_{i_0}(x,t) dx, \\ \lambda_k(0) &= \lambda^0. \end{aligned} \tag{8.4}$$

Note that the depolymerization of one monomer from a proto-oligomer (rate b) and the fragmentation of a monomer from a proto-oligomer (rate β) are different processes biologically, but they produce the same outcome in the model equations. They could be reconciled into a single chemical rate but with a more complex fragmentation kernel, however we choose to keep all processe as simple as possible so that each term is interpretable and controlable. Table 8.1 summarizes all parameters of the model, as well as the values used in numerical simulation (see Subsection 8.2.2 for more detail).

Table 8.1 – **Parameter values used for the simulations of Equation 8.2** (unless specified otherwise). See Subsection 8.2.2 for a detailed justification of the parameter choice.

Parameter	Value	Unit	Description
T	50000	s	Time scale
L	100	μm	Length scale
C_0	10^{-9}	M	Concentration scale
i_0	20	-	Size of oligomers
D_i	$D_1/i^{1/3}$	$m^2.s^{-1}$	Diffusion coefficient of size i
D_1	$2.2.10^{-14}$	$m^2.s^{-1}$	Diffusion coefficient of monomers
δ	5.10^{-4}	s^{-1}	Degradation coefficient of monomers
γ	1	$m.s^{-1}$	Surface absorption rate
r_i	r_0	$M^{-1}s^{-1}$	Polymerization rate of size i
r_0	10^7	$M^{-1}s^{-1}$	Basal poplymerization rate
b	10^{-3}	s^{-1}	Depolymerization rate
β	10^{-4}	s^{-1}	Fragmentation rate
$\lambda_0 \times \pi R^2_{\text{neuron}}/V_{\text{neuron}}$	2.10^{-13}	$M.s^{-1}$	Monomer production rate of a neuron
τ	10^{10}	$M^{-1}.s^{-1}$	Infectivity rate
R_{neuron}	2	μm	Radius of a neuron
V_{neuron}	20	μm^3	Apparent volume of isolation for a neuron
ε	2	μm	Radius of activity for oligomers

Remark. *The analytical expression of the monomer production rate for each neuron k is known analytically as*

$$\lambda_k(t) = \lambda_k^0 \exp\left(-\tau \int_0^t \int_{\Sigma_k^\varepsilon} \mu_{i_0}(x,s) dx ds \right). \tag{8.5}$$

8.1.3 Theoretical results

Before moving on to simulating and exploiting the model, we present a few preliminary theoretical results.

The healthy case. In the case where no oligomers are present ($\mu_2 = \mu_3 = \ldots = \mu_{i_0} = 0$), the monomer concentration distribution verifies the following heat equation

$$\begin{aligned} \frac{\partial m}{\partial t} &= D_1 \Delta m - \delta m, \\ D_1 \nabla m \cdot \vec{n}|_\Gamma &= -\gamma m, \\ D_1 \nabla m \cdot \vec{n}|_{\partial\omega_k} &= \lambda^0. \end{aligned} \tag{8.6}$$

This equation clearly admits a unique solution in X_+. In particular, the steady-state solution of this equation is obtained by solving the corresponding Laplace equation on

the domain. The geometry of the problem has no reason for being symmetrical in any way, so no analytical solution is available. However in practice, solving numerically this initial problem allows us to build a relevant initial condition for the monomer density in the full problem (see Section 8.2).

Existence, uniqueness and positivity of solutions. The theoretical basis of our model is given by the following theorem.

Theorem 8.1. *We assume that all parameters are positive and that the sequence $(r_i)_i$ is non-strictly increasing, i.e. $\forall i \in \{2, \dots, i_0 - 2\}, r_i \leq r_{i+1}$. In these conditions, Problem 1 admits a unique solution.*

Proof. The proof of this result relies on a fixed-point result, which is obtained for a regularized version of the problem and the nextended to the initial problem. The full proof is lengthy and has been submitted for publication as a follow-up study of [Andrade-Restrepo et al., 2019]. □

8.2 Numerical results

With the model formulated in Section 8.1 we run a numerical investigation of the behavior of Aβ oligomers in the vicinity of a few neurons.

8.2.1 Variational formulation and numerical scheme

In order to numerically simulate the full partial differential equations model expressed in Equation 8.2, we use the finite elements method. This requires to specify the variational formulation associated with our model. First we write the partial differential equation system as a system of reaction-diffusion equations of general form

$$\begin{cases} i = 1, \dots, i_0, \dfrac{\partial \mu_i}{\partial t} = D_i \Delta \mu_i + F_i(\mu_1, \dots, \mu_{i_0}), \\ i = 1, \dots, i_0, D_i \dfrac{\partial \mu_i}{\partial \nu} = -\gamma \mu_i \text{ on } \Gamma, \\ i = 2, \dots, i_0 \text{ and } k = 1 \dots N, D_i \dfrac{\partial \mu_i}{\partial \nu} = 0, \text{ and } D_1 \dfrac{\partial \mu_1}{\partial \nu} = \lambda_k(t) \text{ on } \partial\omega_k. \end{cases}$$

By convention and for simplicity $\mu_1 = m$ is the monomer distribution. For the sake of clarity, the reaction terms are explicitly given by

$$\begin{cases} F_1(\mu_1,\dots,\mu_{i_0}) = -\delta\mu_1 + b\sum_{j=3}^{i_0-1}\mu_j + 2\beta\sum_{j=2}^{i_0-1}\mu_j - \sum_{j=2}^{i_0-1} r_j\mu_j\mu_1, \\ F_2(\mu_1,\dots,\mu_{i_0}) = b\mu_3 - r_2\mu_2\mu_1 - \beta\mu_2 + 2\beta\sum_{j=3}^{i_0-1}\mu_j, \\ F_i(\mu_1,\dots,\mu_{i_0}) = b\mu_{i+1} - b\mu_i + r_{i-1}\mu_{i-1}\mu_1 - r_i\mu_i\mu_1 - \beta(i-1)\mu_i + 2\beta\sum_{j=i+1}^{i_0-1}\mu_j, \\ F_{i_0-1}(\mu_1,\dots,\mu_{i_0}) = -b\mu_{i_0-1} + r_{i_0-2}\mu_{i_0-2}\mu_1 - r_{i_0-1}\mu_{i_0-1}\mu_1 - \beta(i_0-2)\mu_{i_0-1}, \\ F_{i_0}(\mu_1,\dots,\mu_{i_0}) = r_{i_0-1}\mu_{i_0-1}\mu_1. \end{cases}$$

To discretize this system in time, we use an semi-implicit Euler scheme, with implicit diffusion and explicit reaction. For a pace δ_t and at step n, it writes

$$\frac{\mu_i^{n+1}-\mu_i^n}{\delta_t} = D_i\Delta\mu_i^{n+1} + F_i(\mu_1^n,\dots,\mu_{i_0}^n).$$

By multiplying with a suitable test function, and integrating over the whole domain we get

$$\int_\Omega(\mu_i^{n+1}v - \mu_i^n v)dx - \int_\Omega \delta_t D_i\Delta\mu_i^{n+1}vdx - \int_\Omega \delta_t F_i(\mu_1^n,\dots,\mu_{i_0}^n)vdx = 0.$$

By the divergence theorem we are left with

$$\begin{aligned}&\int_\Omega(\mu_i^{n+1}v + \delta_t D_i\nabla\mu_i^{n+1}\cdot\nabla v)dx - \int_\Gamma \delta_t D_i(\nabla\mu_i^{n+1}\cdot\vec{n})vdx \\ &-\sum_k\int_{\partial\omega_k}\delta_t D_i(\nabla\mu_i^{n+1}\cdot\vec{n})vdx - \int_\Omega\mu_i^n vdx - \int_\Omega\delta_t F_i(\mu_1^n,\dots,\mu_{i_0}^n)vdx = 0.\end{aligned}$$

The boundary conditions give us the variational formulation for each variable $i = 2,\dots,i_0$

$$\int_\Omega(\mu_i^{n+1}v + \delta_t D_i\nabla\mu_i^{n+1}\cdot\nabla v)dx + \int_\Gamma \delta_t\gamma\mu_i^{n+1}vdx \tag{8.7}$$

$$-\int_\Omega\mu_i^n vdx - \int_\Omega\delta_t F_i(\mu_1^n,\dots,\mu_{i_0}^n)vdx = 0, \tag{8.8}$$

and for the monomers

$$\int_\Omega (\mu_1^{n+1} v + \delta_t D_1 \nabla \mu_1^{n+1} \cdot \nabla v) dx + \int_\Gamma \delta_t \gamma \mu_1^{n+1} v dx - \sum_{k=1}^{N} \int_{\partial \omega_k} \delta_t \lambda_k^{n+1} v dx \\ - \int_\Omega \mu_1^n v dx - \int_\Omega \delta_t F_1(\mu_1^n, \dots, \mu_{i_0}^n) v dx = 0. \tag{8.9}$$

Note that since diffusion is implicit, the source term in the boundary condition is also implicit (λ_k^{n+1}). We evaluate it with a forward Euler scheme, requiring the equation on the monomers to be solved last. In this case we can directly solve

$$\lambda_k^{n+1} - \lambda_k^n = -\delta_t \tau \lambda_k^{n+1} \int_{\Sigma_k^\varepsilon} \mu_{i_0}^{n+1} dx.$$

8.2.2 Parameter choice and scaling

Nondimensional parameters. To ease the numerical simulation, we nondimensionalize the model. In the following we consider SI units. In particular, we express lengths in meters and time in seconds. For concentrations we use the molar concentration unit M ($1M = 1\ mol.L^{-1}$), and we use the following scales:

- Spatial scale: L defines the characteristic length of the domain. Typically L is about 100 μm.
- Time scale: the characteristic time is T, it is about 10000 s.
- Concentration scales: the characteristic concentration is C_0, around $10^{-9}M$.

Using these scales we can nondimensionalize the model. In the rest of this section, a superscript $*$ will indicate nondimensional variables. We define

$$t^* = \frac{t}{T}, x^* = \frac{x}{L}, y^* = \frac{y}{L}, \xi^* = \frac{\xi}{C_0}, \xi = \mu_1, \dots, \mu_{i_0}. \tag{8.10}$$

The non-dimensional operators are given by

$$\begin{aligned} \frac{\partial}{\partial t} &= \frac{1}{T} \frac{\partial}{\partial t^*}, \\ \nabla &= \frac{1}{L} \nabla^*, \\ \Delta &= \frac{1}{L^2} \Delta^*. \end{aligned} \tag{8.11}$$

Now using the equations of the model, we obtain the nondimensional model. The equations are the same as (8.2), replacing the operators by the non-dimensional operators

and modifying the coefficients as follows

$$D^* = D\frac{T}{L^2},\ r_i^* = r_i C_0 T,\ b^* = bT,\ \beta^* = \beta T,$$
$$\delta^* = \delta T,\ \gamma^* = \gamma\frac{T}{L},\ \lambda_k^* = \lambda_k\frac{T}{LC_0},\ \tau^* = \tau C_0 T.$$

Parameter choices. In order to be consistent with biology we need to choose the coefficients with care. We know from anatomy that neurons have a size of a few μm and are separated by around 10 μm in the brain. Accordingly, the characteristic spatial scale will be $L = 100\ \mu m$.

For specific data on Aβ, we refer to [Murphy and Pallitto, 2000]. The diffusion coefficients will be chosen using the Stokes-Einstein relation

$$D = \frac{k_b T}{6\pi\mu r_h},$$

where k_b is the Boltzmann constant ($k_b = 1.38.10^{-23}\ m^2.kg.s^{-2}.K^{-1}$), T the temperature, μ the dynamical viscosity of the fluid, and r_h the hydrodynamic radius of the particle considered. In the case of Aβ particles in the cerebrospinal fluid we have (in SI units) $T = 310\ K(37°C)$, $\mu = 10^{-3}\ kg.m^{-1}.s^{-1}$ [Bloomfield et al., 1998]. The hydrodynamic radius of monomers is $r_h = 1\ nm$ [Nag et al., 2011]. For oligomeric species, the hydrodynamic radius grows with the size and we suggest it scales as $i^{1/3}$ where i is the size of the oligomers (to represent 3D rearrangement of the particle as it grows in size). This ultimately gives $D_1 = 2.27.10^{-10}\ m^2 s^{-1}$, and $D_i = \frac{D_1}{i^{1/3}}$. This value is of the same order as measured by [Murphy and Pallitto, 2000]. However when we use this value for the diffusion coefficient in the simulations, the distribution of Aβ monomers in the spatial scale $L \approx 100\ \mu m$ is almost homogeneous. To obtain a significant variation of the monomer distribution on this scale, the diffusion coefficient has to be reduced to $D \approx 10^{-14}\ m^2.s^{-1}$. This in turn corresponds to a displacement of 1 μm in approximately 10 s. To justify the use of a diffusion coefficient 4 orders of magnitude lower than the one suggested by the Stokes-Einstein formula, we suggest that the cerebrospinal fluid is very crowded by other proteins and assemblies, which impairs the diffusion of molecules. Furthermore, the spatial spreading of the neurons could be increased in the model, because *in vivo* not all the neurons produce Aβ. Without more detailed data, we choose to use $D \approx 10^{-14}\ m^2.s^{-1}$.

For the production and degradation of monomers, we have some suggestions from literature [Murphy and Pallitto, 2000, Nag et al., 2011]. The disease-free equilibrium concentration of Aβ monomers in the cerebrospinal fluid is of about $C_b = 10\ ng.mL^{-1}$ [Mehta et al., 2000]. The molecular weight of Aβ is 4514 $g.mol^{-1}$, so this concentration amounts to about $C_b = 2.10^{-9}\ M$. The half-life of Aβ monomers is a few hours, which

corresponds to a degradation rate δ of about $10^{-4}\ s^{-1}$. The total production rate of a disease-free neuron (integrated over its surface) is $\lambda_0 \pi R^2_{\text{neuron}}$. If we consider that the measured concentration in the cerebrospinal fluid is equivalent to that of a single neuron in a domain of volume $V_{\text{neuron}} = 20\ \mu m^3$, the equilibrium between production and degradation gives us the relation $\lambda_0 \pi R^2_{\text{neuron}}/V = C_b \delta = 2.10^{-13}\ M.s^{-1}$, from which we evaluate λ_0.

The polymerization-depolymerization reaction is estimated to occur at rates $r_0 = 100\ M^{-1}s^{-1}$ and $b = 10^{-3}\ s^{-1}$. The fragmentation rate is more difficult to evaluate, it will be adjusted using the simulations. The same goes for γ and τ. The parameter choices are summarized in Table 8.1.

8.2.3 Numerical simulations

The numerical resolution of the model (using the variational formulation from Subsection 8.2.1) is conducted using Freefem++ [Hecht, 2012], and visualized in Paraview [Ayachit, 2015]. The default parameter values are presented in Table 8.1, and the initial configuration for all the simulations is presented in Figure 8.3.

Figure 8.4 shows the results of the simulation with the default parameters. We observe the successive attacks of oligomers first on the left neuron, then the right neuron. Their monomer production is progressively brought to 0 and after about 20000 s, both of the neurons are completely inactive. The balance between diffusion and replication of the proto-oligomers plays a critical role in the observed dynamics. The spatial distribution of the oligomers is strongly impacted, and their neurotoxic action is also affected. It appears that there is an optimal value for the rate of fragmentation β that induces the fastest neuron inactivation. With extremely high fragmentation rates ($\beta > 5.10^{-3}\ s^{-1}$), the oligomers reach both neurons, but their concentration does not reach sufficiently high levels to completely inactivate them in less than 50000 s, as shown in Figure 8.5. With extremely low fragmentation rates ($\beta < 10^{-5}\ s^{-1}$) the proto-oligomer distribution is shifted towards larger, so they diffuse more slowly. In this case, the first neuron is inactivated efficiently enough, but the second is still producing at half the maximum rate after 50000 s, see Figure 8.6.

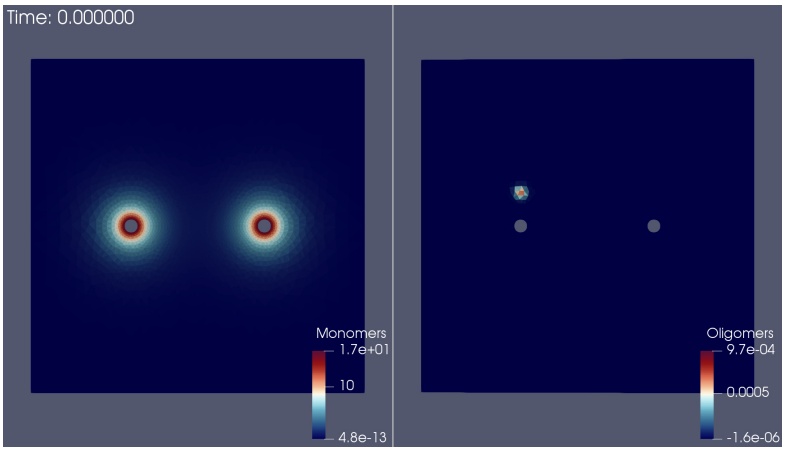

Figure 8.3 – **Initial configuration used for the simulations.** Left panel: Aβ monomer distribution. Right panel: Aβ oligomers (of size i_0) distribution.

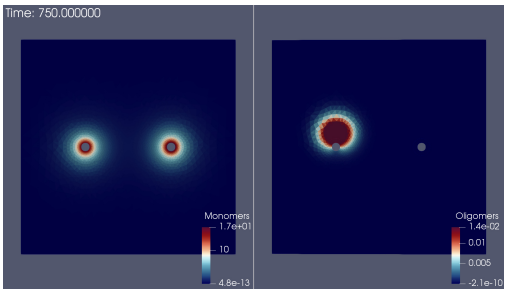

(a) $t = 750\ s$

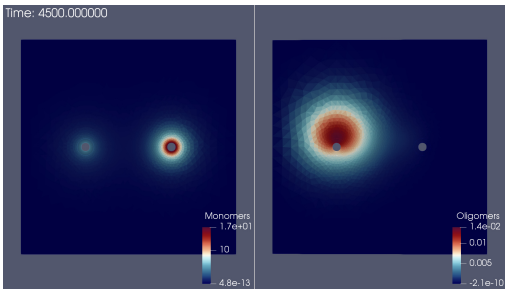

(b) $t = 4500\ s$

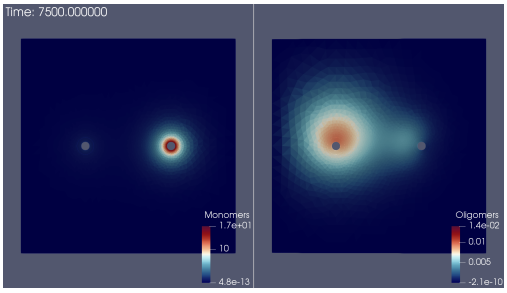

(c) $t = 7500\ s$

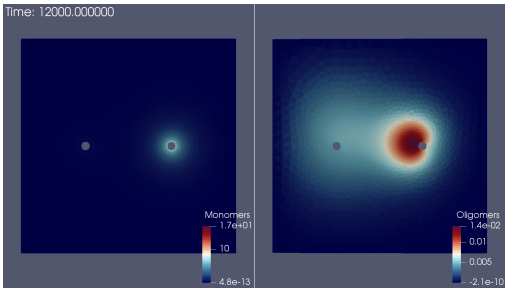

(d) $t = 12000\ s$

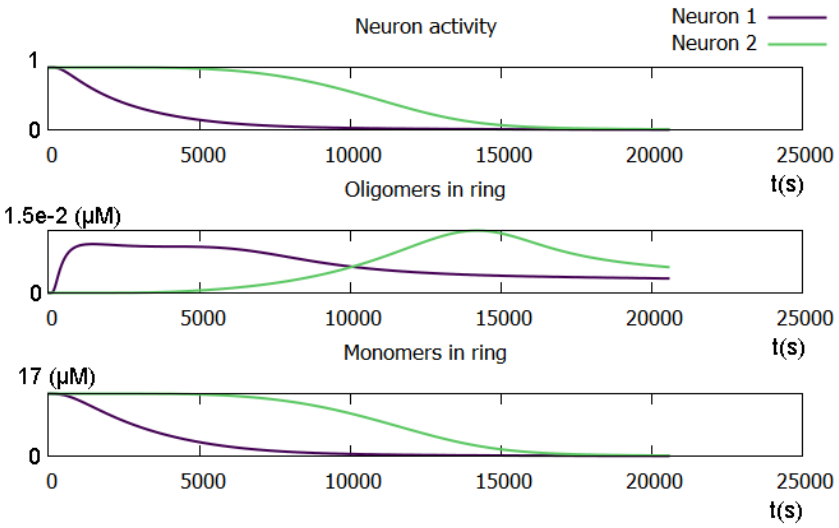

(e) Evolution of monomer production normalized by the maximum λ_0 (top), oligomer concentration in activity ring (middle) and monomer concentration in ring (bottom) for each neuron and over time.

Figure 8.4 – **Simulation results for the default parameters** (see Table 8.1). For panels (a),(b),(c) and (d), the monomer distribution is on the left, and the oligomer distribution is on the right.

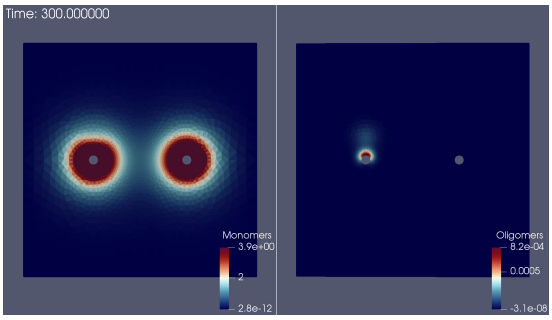

(a) $t = 300\ s$

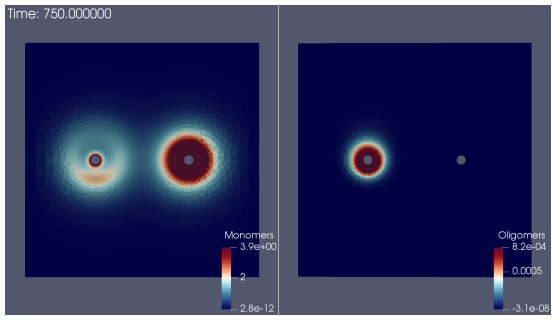

(b) $t = 750\ s$

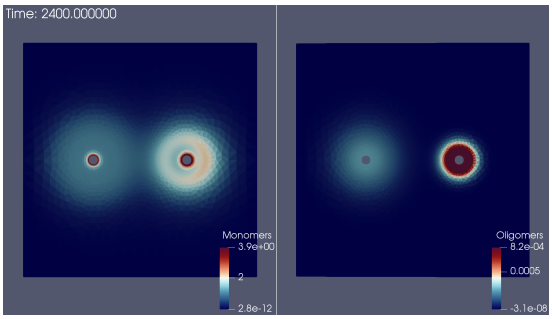

(c) $t = 2400\ s$

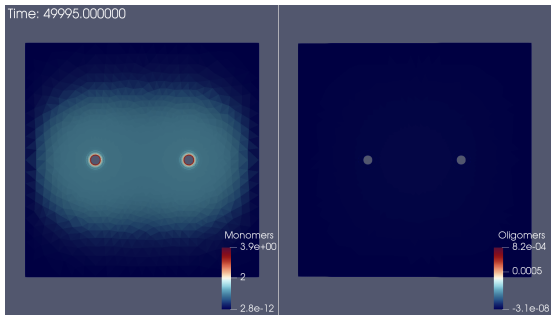

(d) $t = 49995\ s$

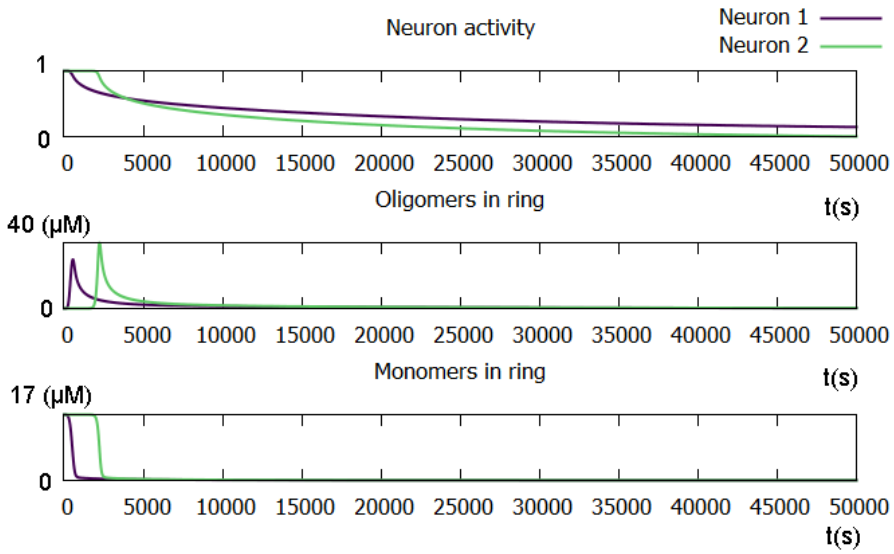

(e) Evolution of monomer production normalized by the maximum λ_0 (top), oligomer concentration in activity ring (middle) and monomer concentration in ring (bottom) for each neuron and over time.

Figure 8.5 – **Simulation results for** $\beta = 5.10^{-3}\ s^{-1}$ (see Table 8.1 for the other paramters). For panels (a),(b),(c) and (d), the monomer distribution is on the left, and the oligomer distribution is on the right.

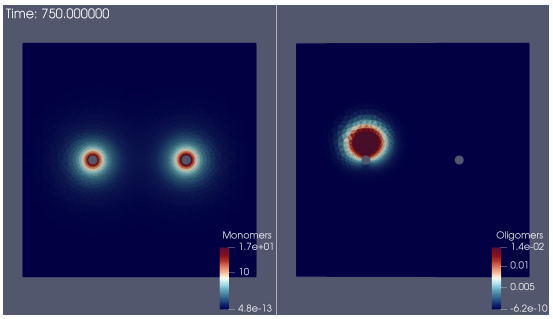

(a) $t = 750\ s$

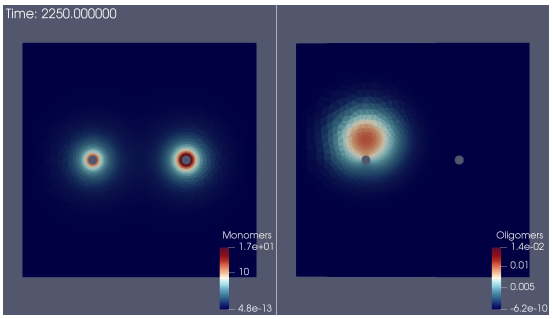

(b) $t = 2250\ s$

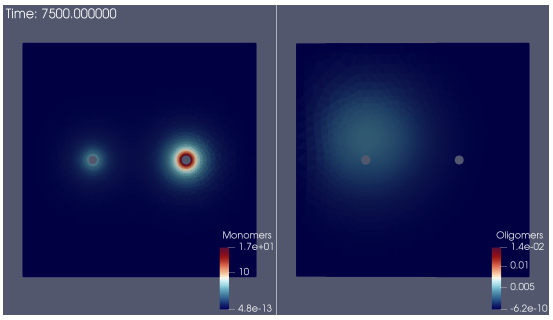

(c) $t = 7500\ s$

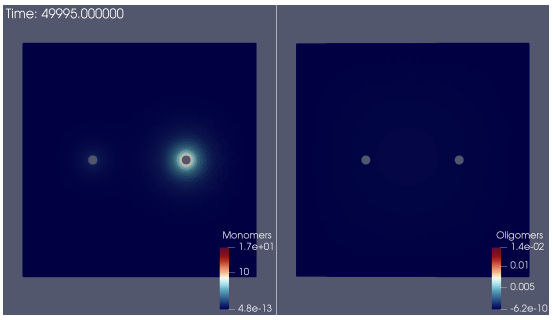

(d) $t = 49995\ s$

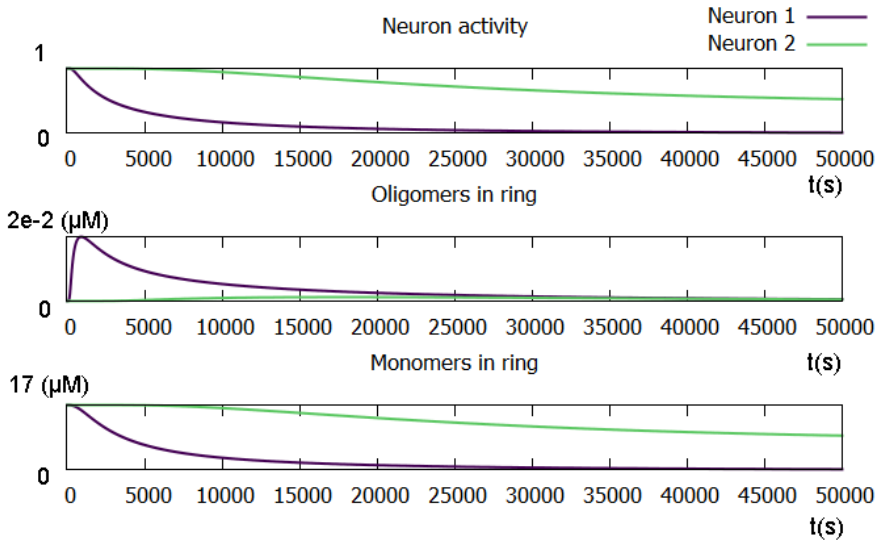

(e) Evolution of monomer production normalized by the maximum λ_0 (top), oligomer concentration in activity ring (middle) and monomer concentration in ring (bottom) for each neuron and over time.

Figure 8.6 – **Simulation results for** $\beta = 1.10^{-5}\ s^{-1}$ (see Table 8.1 for the other paramters). For panels (a),(b),(c) and (d), the monomer distribution is on the left, and the oligomer distribution is on the right.

8.3 Discussion and perspectives

8.3.1 Insight into Alzheimer's Disease and the amyloid cascade hypothesis

The balance between secondary nucleation and diffusion is crucial in determining the efficiency of the propagation of Aβ assemblies. Since the production of Aβ monomers by neurons is affected by the presence of oligomers in their vicinity, this imposes a delayed feedback loop on the formation of oligomers. The faithful propagation of oligomers to entire regions of the brain requires a precise balance between diffusion and secondary nucleation. If the secondary nucleation process is too fast, the pool of Aβ monomers will be locally depleted very rapidly, before the oligomers can reach another neuron. On the other hand if diffusion is too fast, the concentrations of proto-oligomers cannot reach levels high enough so that their replication is efficient. Our model suggests one mechanism for secondary nucleation in the form of fragmentation, however the insight provided by the model does not depend on the precise mechanism. Other hypotheses could lead to similar behavior, as long as the creation of new oligomers is autocatalytic.
Monomer production dynamics drives the evolution of the system. Our model only allows the Aβ monomer production to decrease under the influence of oligomers, however the effect might be the exact opposite [Perez et al., 2010]. Allowing more complex dynamics for the monomer production rates would greatly increase the behavior variety of the model. In particular, if we consider that neurons can recover from the effect of oligomers, oscillations become possible. Similarly, if oligomers impose a reversible positive feedback on monomer production, the balance between diffusion and secondary nucleation becomes even more crucial in the process.

8.3.2 Limitations of our model

Restricted scope. Our model only applies to the early stages in the amyloid cascade, and in the vicinity of a few neurons. This prevents us from comparing our results with clinical data. However it allows us to build a robust model with carefully controled processes, based on mechanistic hypotheses. Because of the lack of connection to experimental and clinical data, some parameters of our model cannot be inferred precisely.
Structural diversity is still not included nor explained. Our model focuses on Aβ oligomers because they drive the propagation of the amyloid cascade in the early stages, however the formation of fibrils and plaques cannot be ignored when considering the whole process. Our model is lacking a mechanistic explanation for the formation of various structures, their interactions and the way these interactions affect the disease's progression.
Alzheimer's Disease is the combined result of many different processes. As we mentioned in Subsection 7.1.3, the amyloid cascade hypothesis remains limited. Our model fits into this framework, but does not include any other complimentary theories.

In particular, we do not consider the accumulation of Tau tangles inside neurons, or the transmission of protein oligomer via mechanisms other than simple diffusion.

8.3.3 Perspectives for future work

Combining with a network-diffusion approach for a full multi-scale model. The reaction-diffusion approach suits a local approach, for short time scales and spatial scales. This could be used in combination with a network-diffusion method such as the one used in [Raj et al., 2012]. The local evolution and amplification of Aβ assemblies would be represented by reaction-diffusion systems, for a restricted domain containing a dozen to a hundred neurons. The long range interactions between different parts of the brain would be represented using a network-diffusion model based on a connectome obtained from real human brains. Building such a multi-scale model would require taking into account other processes in the pathogenesis, including the formation of Tau tangles and long range propagation of misfolded proteins via exosomes and axonal transport.

Similar modeling approach for prion diseases. Discussion with H. Rezaéi and A. Raj led to the formulation of a project aiming at developing a multi-scale model such as the one described above, but in the case of prion diseases. The mechanisms of PrP accumulation are indeed very similar to the mechanisms we developed in this chapter for Aβ, and the pathogenesis is in fact less complex. In this case, accumulation of PrP aggregates can be directly correlated with neurodegeneration. Furthermore, *in vivo* experiments in animal models could allow to track deposition patterns through time and to directly validate the results of the model.

Chapter 9

Conclusion and perspectives

In conclusion to this manuscript, we summarize here the most crucial insights provided by our literature review and modeling contributions. These are the main points we wish to emphasize because they will drive future research in the field of prion models. We also present a few open problems of interest that we did not tackle, by lack of resources.

9.1 Essential insights

9.1.1 Structural diversity plays an essential role in prion propagation

The central point of our progress in kinetic models of prion processes is structural diversity. Taking into account the existence and interaction of different types of structures, each with their own internal organization, brings a whole range of new possibilities. It provides ways for strains to coexist and interact in non-linear ways (see Chapter 3), it allows for oscillating behavior *in vitro* to be reproduced (see Chapter 4), and it offers ways of interpreting puzzling results on prion propagation both in yeast (see Chapter 6) and in mammals (see Chapter 8). Explicitly including different types of structures in a kinetic model also allows building a stronger framework for size-dependent properties.

In fact, changing kinetic rates depending on the size of an assembly (an aggregate or an oligomer) is equivalent to considering each size as a different type of chemical agent. By creating a few different types of structures that grow, replicate and interact with each other, the number of parameters is actually restricted because it does not vary with size. Conceptually the models become more complex than linear stacks of monomers that grow and fragment, but the possibilities are limitless. What is fascinating and thrilling is that the further we explore the biology of prion aggregates, the more intricate and diverse they are revealed to be. Our current understanding is nothing but a scratch on the surface. Overall, kinetic models of prion and amyloid propagation will benefit from taking into account structural diversity, as long as it is dealt with in an explicit way and confronted to experimental observations. One approach we suggest, and put to use in this manuscript, consists in using the classical models as building blocks to establish more elaborate schemes.

9.1.2 Secondary nucleation is at the core of structural diversification

One aspect that is now well established is that structural diversification is a deterministic process. The formation of aggregates follows a pathway in which secondary nucleation processes play a central role. Autocatalysis is usually suggested, with the commonly accepted mechanism of fragmentation. However, the limits of the models based on fragmentation are now clear, and new mechanisms of secondary nucleation need to be proposed and validated. In particular, catalyzed depolymerization seems a promising concept (see Chapter 4). In yeast prions, the role of molecular chaperones is essential (Chapter 6). Our modeling approach sheds light onto the essential properties that secondary nucleation processes should exhibit, but we struggle in justifying any of these mechanisms (including fragmentation) properly with experimental observations. We do not bring a decisive answer to the question of the nature of secondary nucleation. Rather the opposite, we bring many new questions, but also new paradigms and possibilities.

9.1.3 Non-linear behavior at low densities brings a broad range of behavior

In our investigations, the difference between global models and multi-stable models (see Subsection 1.2.4) came up multiple times, both in mammals (see Section 3.3) and in yeast (see Section 8.3). In the case of mammals, multi-stability has a huge impact on the asymptotic outcome of the propagation (the outcome of the disease), and could be the key to explaining many puzzling results of prion transmission such as the species barrier (see Subsection 2.1.3). In the case of yeast prions, multi-stability reflects the reversibility of the prion phenotypes and the possibility of curing yeast colonies of prions by various treatments. As we emphasize in Chapters 3 and 6, multi-stability comes from adding non-linear effects at low densities of aggregates. Understanding these non-linear effects is intimately related to the processes of secondary nucleation and structural

diversification. As is emphasized in Chapter 4, structural diversification happens in the first few minutes of early oligomerization of PrP. Given the complexity of the interactions between the different species, it becomes clear that non-linearities are commonplace in prion formation. This contrasts with the classical modeling method which consists in linearizing the equation around the prion-free equilibrium. Even though this approach is reasonable in many cases, caution is required when studying complex systems with many interacting structures or with low densities of aggregates involved.

9.2 Open problems

9.2.1 Building a mechanistic understanding for structural diversity

In order to properly model structural diversity, a mechanistic framework needs to be built. This means proposing and validating mechanisms for the establishement of structural diversity, starting from a few oligomers and ending with a full range of assemblies and structures. This is inevitably coupled with mechanisms of secondary nucleation, which have to be rigorously defined. The most commonly suggested mechanism for secondary nucleation is still fragmentation, but the need to investigate and validate other mechanisms is clear (see Subsection 1.2.4). Our study suggests a few mechanisms and processes that incorporate structural diversity into the classical frameworks. In particular, we use different types of assemblies that interact together and we include internal structure to aggregates to create polymerization pathways, or depolymerization pathways. However the possibilities are countless, and we need a better experimental understanding of these processes in order to dwindle the hypotheses. For instance, automated analysis of AFM images of OvPrP oligomers (see Subsection 4.4.2) could give us insight into the diversification process of these oligomers.

9.2.2 Understanding the role of Hsp104

In the context of yeast prions, and $[PSI^+]$ in particular, the role of the molecular chaperone Hsp104 remains unclear (see Subsection 5.1.4). With our qualitative insight obtained with the use impulsive differential equations, it appears that structural diversity and multi-stability are essential in modeling yeast prions. Investigating the role of Hsp104 is one of the main directions to explain and justify these elements. Indeed Hsp104 is at the heart of secondary nucleation, and it affects different structures in different ways. Building a multi-stable model of Sup35 aggregates taking into account an explicit role (or rather explicit roles) is the most logical next step in $[PSI^+]$ modeling. The framework we establish in Chapter 6 will then serve to validate and fit such a model.

9.2.3 A full multi-scale model of neurodegenerative diseases

Our investigation of the spatial propagation of Aβ oligomers raised more questions than answers. It is still an open problem to build a multi-scale model that includes all

aspects of protein misfolding disorders inside the brain. Our contributions are only a small step towards the full model (see Chapter 8), and the next steps require strong interactions between many research fields. Kinetic models are only relevant for the mesoscopic scale, but the macroscopic scale involves physiological phenomena that are rarely modeled explicitly. We plan to collaborate with different teams in order to build a model that includes dynamical systems for the molecular scale, coupled with a network-diffusion model to deal with the long range interactions between different regions of the brain.

9.2.4 Getting closer to the data

Most of our contributions so far are only qualitative. We use data to validate or invalidate a model or a mechanism, only by capturing certain features of the behavior. This is inevitable as we are still trying to understand the chemical processes that drive prion propagation. However, as research progresses and the models become more accurate, it is necessary to get closer to the data. This means using statistical methods and inverse problem techniques in order to fit parameters and reproduce experimental observations. It also means working in close collaboration with biologists in order to shape the progress of prion biology from both directions at the same time, conceptual and experimental.

9.3 Concluding remarks

Over the past few decades, the understanding of prion processes has progressed under the combined efforts of experimental investigation and mathematical modeling. The contributions presented in this manuscript are at the edge of these two domains. We worked in close collaboration with biologists to provide them with a set of mathematical tools and to design models under their guidance. This approach is bound to become commonplace in prion research, but also in general biology, if it is not already. Model crafting is an art that requires both sides of the expertise, joined by efficient communication. Our hope is that the present manuscript showcases the benefits as well as the difficulties of mathematical modeling in biology.

Bibliography

[Aguzzi et al., 2018] Aguzzi, A., Lakkaraju, A. K., and Frontzek, K. (2018). Toward therapy of human prion diseases. *Annual review of pharmacology and toxicology*, 58:331–351.

[Alberty and Hammes, 1958] Alberty, R. A. and Hammes, G. G. (1958). Application of the theory of diffusion-controlled reactions to enzyme kinetics. *The Journal of Physical Chemistry*, 62(2):154–159.

[Alper et al., 1967] Alper, T., Cramp, W., Haig, D. A., and Clarke, M. C. (1967). Does the agent of scrapie replicate without nucleic acid? *Nature*, 214(5090):764–766.

[Alvarez-Martinez et al., 2011] Alvarez-Martinez, M.-T., Fontes, P., Zomosa-Signoret, V., Arnaud, J.-D., Hingant, E., Pujo-Menjouet, L., and Liautard, J.-P. (2011). Dynamics of polymerization shed light on the mechanisms that lead to multiple amyloid structures of the prions portein. *Biochimica et Biophysica Acta*, 1814.

[Andrade-Restrepo et al., 2019] Andrade-Restrepo, M., Lemarre, P., Pujo-Menjouet, L., Tine, L., and Ciuperca, S. (2019). Modeling the spatial propagation of Aβ oligomers in Alzheimer's Disease. In *CEMRACS 2018: Numerical and mathematical modeling for biological and medical applications: deterministic, probabilistic and statistical descriptions*, pages 1–10.

[Armiento et al., 2017] Armiento, A., Moireau, P., Martin, D., Lepejova, N., Doumic, M., and Rezaei, H. (2017). The mechanism of monomer transfer between two structurally distinct PrP oligomers. *PLoS one*, 12(7).

[Arrhenius, 1889] Arrhenius, S. (1889). Über die dissociationswärme und den einfluss der temperatur auf den dissociationsgrad der elektrolyte. *Zeitschrift für physikalische Chemie*, 4(1):96–116.

[Ayachit, 2015] Ayachit, U. (2015). The paraview guide: a parallel visualization application.

[Bainov and Simeonov, 1993] Bainov, D. and Simeonov, P. (1993). *Impulsive differential equations: periodic solutions and applications*. Pitmans Monographs and Surveys in Pure and Applied Mathematics. Longmand Scientific and Technical.

[Banks et al., 2017] Banks, H., Flores, K. B., Langlois, C. R., Serio, T. R., and Sindi, S. S. (2017). Estimating the rate of prion aggregate amplification in yeast with a generation and structured population model. *Inverse Problems in Science and Engineering*.

[Banks et al., 2016] Banks, H., Flores, K. B., and Sindi, S. S. (2016). On analytical and numerical approaches to division and label structured population models. *Applied Mathematics Letters*, 60:81–88.

[Baskakov, 2014] Baskakov, I. V. (2014). The many shades of prion strain adaptation. *Prion*, 8(2):169–172.

[Bateman and Wickner, 2013] Bateman, D. A. and Wickner, R. B. (2013). The [PSI+] prion exists as a dynamic cloud of variants. *PLoS genetics*, 9(1):e1003257.

[Bertsch et al., 2017] Bertsch, M., Franchi, B., Marcello, N., Tesi, M. C., and Tosin, A. (2017). Alzheimer's disease: a mathematical model for onset and progression. *Mathematical medicine and biology: a journal of the IMA*, 34(2):193–214.

[Bloom, 2014] Bloom, G. S. (2014). Amyloid-β and tau: the trigger and bullet in alzheimer disease pathogenesis. *JAMA neurology*, 71(4):505–508.

[Bloomfield et al., 1998] Bloomfield, I., Johnston, I., and Bilston, L. (1998). Effects of proteins, blood cells and glucose on the viscosity of cerebrospinal fluid. *Pediatric neurosurgery*, 28(5):246–251.

[Bösl et al., 2006] Bösl, B., Grimminger, V., and Walter, S. (2006). The molecular chaperone hsp104—a molecular machine for protein disaggregation. *Journal of structural biology*, 156(1):139–148.

[Braak and Braak, 1991] Braak, H. and Braak, E. (1991). Neuropathological stageing of alzheimer-related changes. *Acta neuropathologica*, 82(4):239–259.

[Braak and Del Tredici, 2011] Braak, H. and Del Tredici, K. (2011). Alzheimer's pathogenesis: is there neuron-to-neuron propagation? *Acta neuropathologica*, 121(5):589–595.

[Byrne et al., 2009] Byrne, L. J., Cole, D. J., Cox, B. S., Ridout, M. S., Morgan, B. J., and Tuite, M. F. (2009). The Number and Transmission of $[PSI^+]$ Prion Seeds (Propagons) in the Yeast *Saccharomyces cerevisiae* . *PLoS ONE*, 3(4).

[Calvez et al., 2012] Calvez, V., Doumic, M., and Gabriel, P. (2012). Self-similarity in a general aggregation–fragmentation problem. Application to fitness analysis. *J. Math. Pures Appl.*, 98.

[Calvez et al., 2010] Calvez, V., Lenuzza, N., Doumic, M., Deslys, J.-M., Mouthon, F., and Perthame, B. (2010). Prion dynamics with size dependency-strain phenomena. *J. of Biol. Dyn.*, 4(1):28 – 42.

[Calvez et al., 2009] Calvez, V., Lenuzza, N., Oelz, D., Deslys, J.-P., Laurent, P., Mouthon, F., and Perthame, B. (2009). Size distribution dependence of prion aggregates infectivity. *Mathematical Biosciences*, 217(1):88–99.

[Chakroun et al., 2010] Chakroun, N., Prigent, S., Dreiss, C. A., Noinville, S., Chapuis, C., Fraternali, F., and Rezaei, H. (2010). The oligomerization properties of prion protein are restricted to the H2H3 domain. *The FASEB Journal*, 24(9):3222–3231.

[Chen et al., 2011] Chen, B., Retzlaff, M., Roos, T., and Frydman, J. (2011). Cellular strategies of protein quality control. *Cold Spring Harbor perspectives in biology*, 3(8):a004374.

[Chernoff, 2016] Chernoff, Y. (2016). Are there prions in plants? *PNAS*, 113.

[Chernova et al., 2017] Chernova, T. A., Chernoff, Y. O., and Wilkinson, K. D. (2017). Prion-based memory of heat stress in yeast. *Prion*, 11(3):151–161.

[Chernova et al., 2019] Chernova, T. A., Chernoff, Y. O., and Wilkinson, K. D. (2019). Yeast Models for Amyloids and Prions: Environmental Modulation and Drug Discovery. *Molecules*, 24(18):3388.

[Christiano et al., 2014] Christiano, R., Nagaraj, N., Fröhlich, F., and Walther, T. C. (2014). Global proteome turnover analyses of the Yeasts S. cerevisiae and S. pombe. *Cell reports*, 9(5):1959–1965.

[Cohen et al., 1994] Cohen, F. E., Pan, K.-M., Huang, Z., Baldwin, M., Fletterick, R. J., and Prusiner, S. B. (1994). Structural clues to prion replication. *Science*, 264(5158):530–532.

[Cohen et al., 2015] Cohen, M. L., Kim, C., Haldiman, T., ElHag, M., Mehndiratta, P., Pichet, T., Lissemore, F., Shea, M., Cohen, Y., Chen, W., Blevins, J., Appleby, B. S., Surewicz, K., Surewicz, W. K., Sajatovic, M., Tatsuoka, C., Zhang, S., Mayo,

P., Butkiewicz, M., Haines, J. L., Lerner, A. J., and Safar, J. G. (2015). Rapidly progressive Alzheimer's disease features distinct structures of amyloid-beta. *Brain Research*, 135:1009–1022.

[Cohen et al., 2013] Cohen, S. I., Linse, S., Luheshi, L. M., Hellstrand, E., White, D. A., Rajah, L., Otzen, D. E., Vendruscolo, M., Dobson, C. M., and Knowles, T. P. (2013). Proliferation of amyloid-β42 aggregates occurs through a secondary nucleation mechanism. *Proceedings of the National Academy of Sciences*, 110(24):9758–9763.

[Colby and Prusiner, 2011] Colby, D. W. and Prusiner, S. B. (2011). Prions. *Cold Spring Harbor perspectives in biology*, 3(1):a006833.

[Cole et al., 2004] Cole, D. J., Morgan, B. J., Ridout, M. S., Byrne, L. J., and Tuite, M. F. (2004). Estimating the number of prions in yeast cells. *Mathematical medicine and biology: a journal of the IMA*, 21(4):369–395.

[Collinge, 2001] Collinge, J. (2001). Prion diseases of humans and animals: their causes and molecular basis. *Annual review of neuroscience*, 24(1):519–550.

[Collinge, 2010] Collinge, J. (2010). Prion strain mutation and selection. *Science*, 328(5982):1111–1112.

[Collinge and Clarke, 2007] Collinge, J. and Clarke, R. (2007). A General Model of Prion Strains and Their Pathogenicity. *Science*, 318:930 – 936.

[Cox et al., 2003] Cox, B., Ness, F., and Tuite, M. (2003). Analysis of the generation and segregation of propagons: entities that propagate the [PSI+] prion in yeast. *Genetics*, 165(1):23–33.

[Cox and Tuite, 2018] Cox, B. and Tuite, M. (2018). Life of $[PSI]$. *Curr. Genet.*, 64:1–8.

[Cox et al., 2007] Cox, B. S., Byrne, L., and Tuite, M. F. (2007). Prion stability. *Prion*, 1(3):170–178.

[Davis and Sindi, 2016] Davis, J. K. and Sindi, S. S. (2016). A mathematical model of the dynamics of prion aggregates with chaperone-mediated fragmentation. *Journal of Mathematical Biology*, 72(6):1555–1578.

[Dean et al., 2016] Dean, D. N., Pate, K. M., Moss, M. A., and Rangachari, V. (2016). Conformational dynamics of specific Aβ oligomers govern their ability to replicate and induce neuronal apoptosis. *Biochemistry*, 55(15):2238–2250.

[Declerck and Meester, 2003] Declerck, S. and Meester, L. D. (2003). Impact of fish predation on coexisting Daphnia taxa: a partial test of the temporal hybrid superiority hypothesis. *Hydrobiologia*, 500(1):83–94.

[Derdowski et al., 2010] Derdowski, A., Sindi, S. S., Klaips, C. L., DiSalvo, S., and Serio, T. R. (2010). A size threshold limits prion transmission and establishes phenotypic diversity. *Science*, 330(6004):680–683.

[Doumic et al., 2019] Doumic, M., Fellner, K., Mezache, M., and Rezaei, H. (2019). A bi-monomeric, nonlinear Becker–Döring-type system to capture oscillatory aggregation kinetics in prion dynamics. *Journal of theoretical biology*, 480:241–261.

[Doumic and Gabriel, 2010] Doumic, M. and Gabriel, P. (2010). Eigenelements of a general aggregation-fragmentation model. *Mathematical Models and Methods in Applied Sciences*, 20(05):757–783.

[Doumic et al., 2009] Doumic, M., Goudon, T., and Lepoutre, T. (2009). Scaling limit of a discrete prion dynamics model. *Communications in Mathematical Sciences*, 7(4).

[Dufrêne et al., 2017] Dufrêne, Y. F., Ando, T., Garcia, R., Alsteens, D., Martinez-Martin, D., Engel, A., Gerber, C., and Müller, D. J. (2017). Imaging modes of atomic force microscopy for application in molecular and cell biology. *Nature nanotechnology*, 12(4):295–307.

[Eaglestone et al., 2000] Eaglestone, S. S., Ruddock, L. W., Cox, B. S., and Tuite, M. F. (2000). Guanidine hydrochloride blocks a critical step in the propagation of the prion-like determinant $[PSI^+]$ of *Saccharomyces cerevisiae* . *PNAS*, 97(1).

[Eckland et al., 2018] Eckland, T. E., Shikiya, R. A., and Bartz, J. C. (2018). Independent amplification of co-infected long incubation period low conversion efficiency prion strains. *PLoS pathogens*, 14(10).

[Eghiaian et al., 2007] Eghiaian, F., Daubenfeld, T., Quenet, Y., Van Audenhaege, M., Bouin, A.-P., Van Der Rest, G., Grosclaude, J., and Rezaei, H. (2007). Diversity in prion protein oligomerization pathways results from domain expansion as revealed by hydrogen/deuterium exchange and disulfide linkage. *Proceedings of the National Academy of Sciences*, 104(18):7414–7419.

[Eigen, 1996] Eigen, M. (1996). Prionics or the kinetic basis of prion diseases. *Biophysical chemistry*, 63(1):A1–A18.

[Engler et al., 2006] Engler, H., Prüss, J., and Webb, G. F. (2006). Analysis of a model for the dynamics of prions II. *Journal of Mathematical Analysis and Applications*, 324(1):98 – 117.

[Gao et al., 2007] Gao, S., Teng, Z., Nieto, J. J., and Torres, A. (2007). Analysis of an SIR Epidemic Model with Pulse Vaccination and Distributed Time Delay. *Journal of Biomedicine and Biotechnology*.

[Girel and Crauste, 2018] Girel, S. and Crauste, F. (2018). Existence and stability of periodic solutions of an impulsive differential equation and application to CD8 T-cell differentiation. *Journal of Mathematical Biology*.

[Gliwicz and Wrzosek, 2008] Gliwicz, Z. M. and Wrzosek, D. (2008). Predation-Mediated Coexistence of Large- and Small-Bodied Daphnia at Different Food Levels. *The American Naturalist*, 172(3):358–374.

[Greene et al., 2018] Greene, L. E., Zhao, X., and Eisenberg, E. (2018). Curing of [PSI+] by Hsp104 Overexpression: Clues to solving the puzzle. *Prion*, 12(1):9–15.

[Greer et al., 2006] Greer, M. L., Pujo-Menjouet, L., and Webb, G. F. (2006). A mathematical analysis of the dynamics of prion proliferation. *Journal of Theoretical Biology*, 242(3):598 – 606.

[Greer et al., 2007] Greer, M. L., van den Driessche, P., Wang, L., and Webb, G. F. (2007). Effects of general incidence and polymer joining on nucleated polymerization in a model of prion proliferation. *SIAM Journal on Applied Mathematics*, 68(1):154–170.

[Griffith, 1967] Griffith, J. S. (1967). Nature of the scrapie agent: Self-replication and scrapie. *Nature*, 215(5105):1043–1044.

[Haass and Selkoe, 2007] Haass, C. and Selkoe, D. J. (2007). Soluble protein oligomers in neurodegeneration: lessons from the alzheimer's amyloid β-peptide. *Nature reviews Molecular cell biology*, 8(2):101–112.

[Hadlow et al., 1959] Hadlow, W. J. et al. (1959). Scrapie and Kuru. *Scrapie and Kuru.*, pages 289–90.

[Hardy and Selkoe, 2002] Hardy, J. and Selkoe, D. J. (2002). The amyloid hypothesis of Alzheimer's disease: progress and problems on the road to therapeutics. *science*, 297(5580):353–356.

[Hecht, 2012] Hecht, F. (2012). New development in FreeFem++. *J. Numer. Math.*, 20(3-4):251–265.

[Helal et al., 2019] Helal, M., Igel-Egalon, A., Lakmeche, A., Mazzocco, P., Perrillat-Mercerot, A., Pujo-Menjouet, L., Rezaei, H., and Tine, L. M. (2019). Stability analysis of a steady state of a model describing Alzheimer's disease and interactions with prion proteins. *Journal of mathematical biology*, 78(1-2):57–81.

[Hingant et al., 2014] Hingant, E., Fontes, P., Alvarez-Martinez, M. T., Arnaud, J.-D., Liautard, J.-P., and Pujo-Menjouet, L. (2014). A Micellar On-Pathway Intermediate

Step Explains the Kinetics of Prion Amyloid Formation. *PLoS Computational Biology*, 10.

[Hingant and Yvinec, 2017] Hingant, E. and Yvinec, R. (2017). Deterministic and stochastic Becker–Döring equations: Past and recent mathematical developments. In *Stochastic processes, multiscale modeling, and numerical methods for computational cellular biology*, pages 175–204. Springer.

[Ho et al., 2018] Ho, B., Baryshnikova, A., and Brown, G. W. (2018). Unification of protein abundance datasets yields a quantitative saccharomyces cerevisiae proteome. *Cell systems*, 6(2):192–205.

[Hulst and van de Hulst, 1981] Hulst, H. C. and van de Hulst, H. C. (1981). *Light scattering by small particles*. Courier Corporation.

[Igel-Egalon et al., 2018] Igel-Egalon, A., Béringue, V., Rezaei, H., and Sibille, P. (2018). Prion strains and transmission barrier phenomena. *Pathogens*, 7(1):5.

[Igel-Egalon et al., 2019a] Igel-Egalon, A., Bohl, J., Moudjou, M., Herzog, L., Reine, F., Rezaei, H., and Béringue, V. (2019a). Heterogeneity and architecture of pathological prion protein assemblies: Time to revisit the molecular basis of the prion replication process? *Viruses*, 11(5):429.

[Igel-Egalon et al., 2019b] Igel-Egalon, A., Laferrière, F., Moudjou, M., Bohl, J., Mezache, M., Knäpple, T., Herzog, L., Reine, F., Jas-Duval, C., Doumic, M., et al. (2019b). Early stage prion assembly involves two subpopulations with different quaternary structures and a secondary templating pathway. *Communications biology*, 2(1):1–13.

[Igel-Egalon et al., 2017] Igel-Egalon, A., Moudjou, M., Martin, D., Busley, A., Knäpple, T., Herzog, L., Reine, F., Lepejova, N., Richard, C.-A., Béringue, V., and Rezaei, H. (2017). Reversible unfolding of infectious prion assemblies reveals the existence of an oligomeric elementary brick. *PLoS Pathogens*.

[Ironside et al., 2018] Ironside, J. W., Ritchie, D. L., and Head, M. W. (2018). Prion diseases. In *Handbook of clinical neurology*, volume 145, pages 393–403. Elsevier.

[Jagust and Mormino, 2011] Jagust, W. J. and Mormino, E. C. (2011). Lifespan brain activity, β-amyloid, and alzheimer's disease. *Trends in cognitive sciences*, 15(11):520–526.

[Jones and Tuite, 2005] Jones, G. and Tuite, M. (2005). Chaperoning prions : the cellular machinery for propagating an infectious protein ? *BioEssays*, 27(8):823 – 832.

[Kobayashi et al., 2019] Kobayashi, A., Iwasaki, Y., Takao, M., Saito, Y., Iwaki, T., Qi, Z., Torimoto, R., Shimazaki, T., Munesue, Y., Isoda, N., et al. (2019). A novel combination of prion strain co-occurrence in patients with sporadic Creutzfeldt-Jakob Disease. *The American journal of pathology*, 189(6):1276–1283.

[Kryndushkin et al., 2003] Kryndushkin, D., Alexandrov, I., Ter-Avanesyan, M., and Kushnirov, V. (2003). Yeast [psi^+] Prion Aggregates Are Formed by Small Sup35 Polymers Fragmented by Hsp104. *Journal of Biological Chemistry*, 278(49).

[Kuo-Chen and Shou-ping, 1974] Kuo-Chen, C. and Shou-ping, J. (1974). Studies on the rate of diffusion-controlled reactions of enzymes. Spatial factor and force field factor. *Sci Sin*, 27(5):664–680.

[Lakshmikanthanm et al., 1989] Lakshmikanthanm, V., Bainov, D. D., and Simeonov, P. S. (1989). *Theory of impulsive differential equations*, volume 6 of *Series in Modern Applied Mathematics*. World Scientific.

[Langenfeld et al., 2016] Langenfeld, K. A., Shikiya, R. A., Kincaid, A. E., and Bartza, J. C. (2016). Incongruity between Prion Conversion and Incubation Period following Coinfection. *Journal of Virology*, 90(12).

[Lansbury and Caughey, 1995] Lansbury, P. T. and Caughey, B. (1995). The chemistry of scrapie infection: implications of the ice 9 metaphor. *Chem. Biol.*, 2:1–5.

[Laurent, 1998] Laurent, M. (1998). Bistability and the species barrier in prion diseases: stepping across the threshold or not. *Biophysical chemistry*, 72(1-2):211–222.

[Le Dur et al., 2017] Le Dur, A., Laï, T. L., Stinnakre, M.-G., Laisné, A., Chenais, N., Rakotobe, S., Passet, B., Reine, F., Soulier, S., Herzog, L., Tilly, G., Rézaei, H., Béringue, V., Vilotte, J.-L., and Laude, H. (2017). Divergent prion strain evolution driven by PrP^C expression level in transgenic mice. *Nature Communications*.

[Lemarre et al., 2018] Lemarre, P., Pujo-Menjouet, L., and Sindi, S. S. (2018). Generalizing a mathematical model of prion aggregation allows strain coexistence and co-stability by including a novel misfolded species. *Journal of mathematical biology*, pages 1–31.

[Lemarre et al., 2020] Lemarre, P., Pujo-Menjouet, L., and Sindi, S. S. (2020). A unifying model for the propagation of prion proteins in yeast brings insight into the [PSI+] prion. *PLoS Computational Biology*, 16(5):e1007647.

[Lenuzza, 2009] Lenuzza, N. (2009). *Modélisation de la réplications des Prions: Implication de la dépendance en taille des agrégats de PrP et de l'hétérogénéité des populations cellulaires.* PhD thesis.

[Liebman and Chernoff, 2012] Liebman, S. W. and Chernoff, Y. O. (2012). Prions in yeast. *Genetics*, 191(4):1041–1072.

[Lindquist and Krishnan, 2005] Lindquist, S. and Krishnan, R. (2005). Structural insights into a yeast prion illuminate nucleation and strain diversity. *Nature*, 435.

[Liu and Takeuchi, 2007] Liu, X. and Takeuchi, Y. (2007). Periodicity and global dynamics of an impulsive delay Lasota–Wazewska model. *Journal of mathematical analysis and applications*, 327(1):326–341.

[March et al., 2016] March, Z., King, O., and Shorter, J. (2016). Prion-like domains as epigenetic regulators, scaffolds for subcellular organization and driver of neurodegenerative disease. *Brain Research*, 164:9–18.

[Marín-Moreno et al., 2018] Marín-Moreno, A., Aguilar-Calvo, P., Pitarch, J. L., Espinosa, J. C., and Torres, J. M. (2018). Nonpathogenic heterologous prions can interfere with prion infection in a strain-dependent manner. *Journal of virology*, 92(24):e01086–18.

[Masel et al., 1999] Masel, J., Jansen, V., and Nowak, M. (1999). Quantifying the kinetic parameters of prion replication. *Biophysical Chemistry*, 77:139–152.

[Mays et al., 2015] Mays, C. E., van der Merwe, J., Kim, C., Haldiman, T., McKenzie, D., Safar, J. G., and Westaway, D. (2015). Prion Infectivity Plateaus and Conversion to Symptomatic Disease Originate from Falling Precursor Levels and Increased Levels of Oligomeric PrP^{Sc} Species. *Journal of Virology*, 89(24).

[Mehta et al., 2000] Mehta, P., Pirttilä, T., Mehta, S., Sersen, E., Aisen, P., and Wisniewski, H. (2000). Plasma and cerebrospinal fluid levels of amyloid β proteins 1-40 and 1-42 in Alzheimer disease. *Archives of neurology*, 57(1):100–105.

[Morales, 2017] Morales, R. (2017). Prion strains in mammals: Different conformations leading to disease. *PLoS Pathogens*.

[Murphy and Pallitto, 2000] Murphy, R. and Pallitto, M. (2000). Probing the kinetics of β-amyloid self-association. *Journal of structural biology*, 130(2-3):109–122.

[Nag et al., 2011] Nag, S., Sarkar, B., Bandyopadhyay, A., Sahoo, B., Sreenivasan, V., Kombrabail, M., Muralidharan, C., and Maiti, S. (2011). The nature of the amyloid-β monomer and the monomer-oligomer equilibrium. *Journal of Biological Chemistry*, pages jbc–M110.

[Nee, 2016] Nee, S. (2016). The evolutionary ecology of molecular replicators. *Royal Society open science*, 3(8):160235.

[Ness et al., 2017] Ness, F., Cox, B. S., Wongwigkarn, J., Naeimi, W. R., and Tuite, M. F. (2017). Over-expression of the molecular chaperone Hsp104 in Saccharomyces cerevisiae results in the malpartition of $[PSI^+]$ propagons. *Molecular Biology*, 104(1):125–143.

[Ness et al., 2002] Ness, F., Ferreira, P., Cox, B. S., and Tuite, M. F. (2002). Guanidine Hydrochloride Inhibits the Generation of Prion "Seeds" but Not Prion Protein Aggregation in Yeast. *Molecular and Cellular Biology*, 22(15):5593–5605.

[Olsson et al., 2018] Olsson, T. T., Klementieva, O., and Gouras, G. K. (2018). Prion-like seeding and nucleation of intracellular amyloid-β. *Neurobiology of disease*, 113:1–10.

[Park et al., 2012] Park, Y.-N., Morales, D., Rubinson, E. H., Maison, D., Eisenberg, E., and Greene, L. E. (2012). Differences in the Curing of $[PSI^+]$ Prion by Various Methods of Hsp104 Inactivation. *PLoS ONE*, 7(6).

[Park et al., 2014] Park, Y.-N., Zhao, X., Yim, Y.-I., Todor, H., Ellerbrock, R., Reidy, M., Eisenberg, E., Masison, D. C., and Greene, L. E. (2014). Hsp104 Overexpression Cures *Saccharomyces cerevisiae* $[PSI^+]$ by Causing Dissolution of the Prion Seeds. *Eukaryotic Cell*, 13(5):635–647.

[Perez et al., 2010] Perez, J., Carrero, I., Gonzalo, P., Arevalo-Serrano, J., Sanz-Anquela, J., Ortega, J., Rodriguez, M., and Gonzalo-Ruiz, A. (2010). Soluble oligomeric forms of beta-amyloid (Aβ) peptide stimulate Aβ production via astrogliosis in the rat brain. *Experimental neurology*, 223(2):410–421.

[Prusiner, 1982] Prusiner, S. B. (1982). Novel proteinaceous infectious particles cause scrapie. *Science*, 216(4542):136–144.

[Prüss et al., 2006] Prüss, J., Pujo-Menjouet, L., Webb, G., and Zacher, R. (2006). Analysis of a model for the dynamics of prions. *Discrete and Continuous Dynamical Systems - Series B*, 6(1):225 – 235.

[Pujo-Menjouet, 2016] Pujo-Menjouet, L. (2016). Etude de modèles mathématiques issus de la biologie du cycle cellulaire et de la dynamique des protéines. Habilitation à diriger des recherches, Université Claude Bernard Lyon 1 - Institut Camille Jordan.

[Rabinovici et al., 2010] Rabinovici, G. D., Furst, A. J., Alkalay, A., Racine, C. A., O'Neil, J. P., Janabi, M., Baker, S. L., Agarwal, N., Bonasera, S. J., Mormino, E. C., et al. (2010). Increased metabolic vulnerability in early-onset Alzheimer's disease is not related to amyloid burden. *Brain*, 133(2):512–528.

[Raj et al., 2012] Raj, A., Kuceyeski, A., and Weiner, M. (2012). A network diffusion model of disease progression in dementia. *Neuron*, 73(6):1204–1215.

[Rodrigue et al., 2013] Rodrigue, K. M., Rieck, J. R., Kennedy, K. M., Devous, M. D., Diaz-Arrastia, R., and Park, D. C. (2013). Risk factors for β-amyloid deposition in healthy aging: vascular and genetic effects. *JAMA neurology*, 70(5):600–606.

[Romanova and Chernoff, 2009] Romanova, N. V. and Chernoff, Y. O. (2009). Hsp104 and Prion Propagation. *Protein Pept. Lett.*, 16(6):598–605.

[Rubenstein et al., 2007] Rubenstein, R., Gray, P., Cleland, T., Piltch, M., Hlavacek, W., Roberts, R., Ambrosiano, J., and Kim, J.-I. (2007). Dynamics of the nucleated polymerization model of prion replication. *Biophysical chemistry*, 125(2-3):360–367.

[Rubenstein et al., 1991] Rubenstein, R., Merz, P. A., Kascak, R. J., Scalici, C. L., Papini, M. C., Carp, R. I., and Kimberlin, R. H. (1991). Scrapie-Infected Spleens: Analysis of Infectivity, Scrapie-Associated Fibrils, and Protease-Resistant Proteins. *The Journal of Infetious Diseases*, 164(1).

[Samoilenko and Perestyuk, 1995] Samoilenko, A. M. and Perestyuk, N. A. (1995). *Impulsive differential equations*, volume 14 of *World Scientific Series on Nonlinear Science - A*. World Scientific.

[Satpute-Krishnan et al., 2007] Satpute-Krishnan, P., Langseth, S. X., and Serio, T. R. (2007). Hsp104-Dependent Remodeling of Prion Complexes Mediates Protein-Only Inheritance. *PLoS Biology*, 5(2).

[Scialò et al., 2019] Scialò, C., De Cecco, E., Manganotti, P., and Legname, G. (2019). Prion and prion-like protein strains: deciphering the molecular basis of heterogeneity in neurodegeneration. *Viruses*, 11(3):261.

[Scott et al., 1991] Scott, S. K., Peng, B., Tomlin, A. S., and Showalter, K. (1991). Transient chaos in a closed chemical system. *The Journal of chemical physics*, 94(2):1134–1140.

[Sengupta et al., 2016] Sengupta, U., Nilson, A. N., and Kayed, R. (2016). The role of amyloid-β oligomers in toxicity, propagation, and immunotherapy. *EBioMedicine*, 6:42–49.

[Sharma et al., 2017] Sharma, J., Wisniewski, B. T., Paulson, E., Obaoye, J. O., Merrill, S. J., and Manogaran, A. L. (2017). De novo $[PSI^+]$ prion formation involves multiple pathways to form infectious oligomers. *Scientific Reports*.

[Shorter and Lindquist, 2006] Shorter, J. and Lindquist, S. (2006). Destruction or Potentiation of Different Prions Catalyzed by Similar Hsp104 Remodeling Activities. *Molecular Cell*, 23:425–438.

[Shorter and Lindquist, 2008] Shorter, J. and Lindquist, S. (2008). Hsp104, Hsp70 and Hsp40 interplay regulates formation, growth and elimination of Sup35 prions. *The EMBO journal*, 27(20):2712–2724.

[Silveira et al., 2005] Silveira, J. R., Raymond, G. J., Hughson, A. G., Race, R. E., Sim, V. L., Hayes, S. F., and Caughey, B. (2005). The most infectious prion protein particles. *Nature*, 437(7056):257–261.

[Sindi and Serio, 2009] Sindi, S. and Serio, T. (2009). Prion Dynamics and the Quest for the Genetic Determinant in Protein-Only Inheritance. *Current Opinion in Microbiology*, 12(6):623–630.

[Sindi, 2017] Sindi, S. S. (2017). Mathematical Modeling of Prion Disease. In *Prion-An Overview*. InTech.

[Sindi and Olofsson, 2013] Sindi, S. S. and Olofsson, P. (2013). A discrete-time branching process model of yeast prion curing curves. *Mathematical Population Studies*, 20(1).

[Sondag et al., 2009] Sondag, C. M., Dhawan, G., and Combs, C. K. (2009). Beta amyloid oligomers and fibrils stimulate differential activation of primary microglia. *Journal of neuroinflammation*, 6(1):1–13.

[Soto, 2003] Soto, C. (2003). Unfolding the role of protein misfolding in neurodegenerative diseases. *Nature Reviews Neuroscience*, 4(1):49.

[Sowade and Jahn, 2017] Sowade, R. F. and Jahn, T. R. (2017). Seed-induced acceleration of amyloid-β mediated neurotoxicity in vivo. *Nature communications*, 8(1):1–12.

[Stamova, 2009] Stamova, I. (2009). *Stability Analysis of Impulsive Functional Differential Equations*. Gruyter Expositions in Mathematics. Walter de Gruyter.

[Tanaka et al., 2006] Tanaka, M., Collins, S., Toyama, B., and Weissman, J. (2006). The physical basis of how prions conformations determine strain phenotypes. *Nature*, 442:585 – 589.

[Thal et al., 2002] Thal, D. R., Rüb, U., Orantes, M., and Braak, H. (2002). Phases of Aβ-deposition in the human brain and its relevance for the development of AD. *Neurology*, 58(12):1791–1800.

[Tuite and Cox, 2003] Tuite, M. and Cox, B. (2003). Propagation of yeast prions. *Nature Reviews Molecular Cell Biology*, 4:878 – 889.

[Tuite and Serio, 2010] Tuite, M. and Serio, T. (2010). The prion hypothesis : from biological anomaly to regulatory mechanism. *Nature Reviews Molecular Cell Biology*, 11(12):823 – 833.

[Villali et al., 2020] Villali, J., Dark, J., Brechtel, T. M., Pei, F., Sindi, S. S., and Serio, T. R. (2020). Nucleation seed size determines amyloid clearance and establishes a barrier to prion appearance in yeast. *Nature Structural & Molecular Biology*.

[Wattis, 1999] Wattis, J. A. (1999). A Becker-Döring model of competitive nucleation. *Journal of Physics A: Mathematical and General*, 32(49):8755.

[Webb et al., 2013] Webb, G., Pujo-Menjouet, L., Hingant, E., and M., H. (2013). Alzheimer's disease: analysis of a mathematical model incorporating the role of prions. *Journal of Mathematical Biology*.

[Wegrzyn et al., 2001] Wegrzyn, R. D., Bapat, K., Newnam, G. P., Zink, A. D., and Chernoff, Y. O. (2001). Mechanism of Prion Loss after Hsp104 Inactivation in Yeast. *Molecular and Cellular Biology*, 21(14):4656–4669.

[Weiss, 1997] Weiss, J. N. (1997). The Hill equation revisited: uses and misuses. *FASEB J.*, 11.

[Weissman et al., 2004] Weissman, J., Chien, P., and DePace, A. (2004). Emerging Principles of Conformation-Based Prion Inheritance. *Annual Reviews Biochem.*, 73:617 – 656.

[Winkler et al., 2012] Winkler, J., Tyedmers, J., Bukau, B., and Mogk, A. (2012). Hsp70 targets Hsp100 chaperones to substrates for protein disaggregation and prion fragmentation. *Journal of Cell Biology*, 198(3):387 – 404.

[Xiao et al., 2017] Xiao, T., Zhang, W., Jiao, B., Pan, C.-Z., Liu, X., and Shen, L. (2017). The role of exosomes in the pathogenesis of Alzheimer's disease. *Translational neurodegeneration*, 6(1):3.

[Yvinec, 2012] Yvinec, R. (2012). *Probabilistic modeling in cellular and molecular biology*. PhD thesis, Université Claude Bernard - Lyon 1.

[Yvinec et al., 2015] Yvinec, R., Deschamps, J., and Hingant, E. (2015). From Becker-Döring to Lifshitz-Slyozov: deriving the non-local boundary condition of a non-linear transport equation. In *ITM Web of Conferences*, volume 5, page 00017. EDP Sciences.

[Zhao et al., 2017] Zhao, X., Rodriguez, R., Silberman, R. E., Ahearn, J. M., Saidha, S., Cummins, K. C., Eisenberg, E., , and Greene, L. E. (2017). Heat shock protein 104 (Hsp104)-mediated curing of $[PSI^+]$ yeast prions depends on both $[PSI^+]$ conformation and the properties of the Hsp104 homologs. *J. Biol. Chem.*, 292(21):8630–8641.

Chapter A

Global stability the multiple strain Nucleated Polymerization model

This chapter is dedicated to the proof of Theorem 2.1. For the existence and uniqueness of solutions we refer to [Prüss et al., 2006], from which the results can easily be extended to the general N strain case.

A.1 Global stability of the Disease-Free Equilibrium

Proof. When $\mathcal{R}_0 = \max_{i=1\dots N} R_0^i \leq 1$, we define the function L given by

$$L(V, U_1, P_1 \dots, U_N, P_N) = \frac{1}{2}\Big(V - \frac{\lambda}{\gamma}\Big)^2 + \sum_{i=1}^{N} b_i \Big(\frac{\mu_i}{\beta_i} U_i + P_i\Big), \text{ with } b_i = 2\frac{(\mu_i + \beta_i x_i)^2}{\beta_i \tau_i} - \frac{\lambda}{\gamma} - \frac{\beta_i^2 x_i^2}{\beta_i \tau_i}.$$

This function is a Lyapunov function for the Disease-Free Equilibrium $(\lambda/\gamma, 0, 0, \dots, 0, 0)$. Indeed it is positive, because $R_0^i \leq 1$ implies $\frac{(\mu_i+\beta_i x_i)^2}{\beta_i \tau_i} \geq \frac{\lambda}{\gamma}$ and thus $b_i \geq \frac{(\mu_i+\beta_i x_i)^2 - \beta_i^2 x_i^2}{\beta_i \tau_i} > 0$ for $i = 1 \dots N$. It evaluates to 0 at the Disease-Free Equilibrium, and its derivative along trajectories is

$$\begin{aligned}
\dot{L} =& \Big(V - \frac{\lambda}{\gamma}\Big)\Big(\lambda - \gamma V - \sum_{i=1}^{N} (\tau_i V U_i + \beta_i x_i^2 U_i)\Big) - \sum_{i=1}^{N} b_i U_i \Big(\frac{\mu_i^2}{\beta_i} + 2\mu_i x_i - \tau_i V + \beta_i x_i^2\Big), \\
=& -\frac{1}{\gamma}\Big(V - \frac{\lambda}{\gamma}\Big)^2 - \sum_{i=1}^{N} \tau_i U_i \left(V^2 - V\Big(\frac{\lambda}{\gamma} + \frac{\beta_i x_i^2}{\tau_i} + b_i\Big) + x_i^2 \frac{\lambda \beta_i}{\gamma \tau_i} + b_i \frac{(\mu_i + \beta_i x_i)^2}{\tau_i \beta_i} \right).
\end{aligned}$$

The choice of b_i yields

$$\begin{aligned}
\dot{L} = -\frac{1}{\gamma}\Big(V - \frac{\lambda}{\gamma}\Big)^2 - \sum_{i=1}^{N} \tau_i U_i \Bigg(V^2 - 2V \frac{(\mu_i + \beta_i x_i)^2}{\beta_i \tau_i} + \Big(\frac{(\mu_i + \beta_i x_i)^2}{\tau_i \beta_i}\Big)^2 \\
+ \frac{\mu_i(\mu_i + 2\beta_i x_i)}{\beta_i \tau_i}\Big(\frac{(\mu_i + \beta_i x_i)^2}{\beta_i \tau_i} - \frac{\lambda}{\gamma}\Big)\Bigg),
\end{aligned}$$

$$\dot{L} = -\frac{1}{\gamma}\Big(V - \frac{\lambda}{\gamma}\Big)^2 - \sum_{i=1}^{N} \tau_i U_i \left(\Big(V - \frac{(\mu_i + \beta_i x_i)^2}{\beta_i \tau_i}\Big)^2 + \frac{\mu_i(\mu_i + 2\beta_i x_i)}{\beta_i \tau_i}\Big(\frac{(\mu_i + \beta_i x_i)^2}{\beta_i \tau_i} - \frac{\lambda}{\gamma}\Big)\right).$$

It is simple to verify that, under the hypothesis that $R_0^i \leq 1$ for each strain, the derivative of L is negative along the trajectories, and evaluates to 0 at the Disease-Free Equilibrum only. □

A.2 Global stability of the endemic steady-state

Proof. As in the Theorem 2.1, let us assume all strains have distinct R_0^i values, and that Strain 1 has the maximal value $\mathcal{R}_0 = R_0^1 = \max_{i=1\dots N} R_0^i$. It is convenient for this part to consider a modification of the model, namely choosing to study $W_i = P_i - x_i U_i$ instead of P_i for each strain. The equations of the model now read

$$\begin{aligned}
\frac{dV}{dt} =& \lambda - \gamma V(t) + \sum_{i=1}^{N} (-\tau_i V(t) U_i(t) + \beta_i x_i^2 U_i(t)),\\
\frac{dU_i}{dt} =& \beta_i W_i(t) - (\mu_i + \beta_i x_i) U_i(t),\ i = 1 \dots N,\\
\frac{dW_i}{dt} =& \tau_i V(t) U_i(t) - (\mu_i + \beta_i x_i) W_i(t),\ i = 1 \dots N.
\end{aligned}$$

In this system, the disease steady-state (involving Strain 1) is given by $V^* = \frac{(\mu_1+\beta_1 x_1)^2}{\beta_1 \tau_1}$, $U_1^* = \frac{\lambda\beta_1\tau_1 - \gamma(\mu_1+\beta_1 x_1)^2}{\mu_1\tau_1(\mu_1+\beta_1 x_1)}$, $W_1^* = \frac{\mu_1+\beta_1 x_1}{\beta_1} U_1^*, \forall j \in \{2 \dots N\}, U_j^* = P_j^* = 0$.

When $\mathcal{R}_0 = R_0^1 = \max\limits_{i=1\dots N} R_0^i > 1$, we define the function L given by

$$\begin{aligned}
L(V, U_1, W_1, \dots, U_N, W_N) =& \Big(1 + \frac{\beta_1 x_1^2}{\tau_1 V^* - \beta_1 x_1^2}\Big)(V - V^* - V^* \log(V/V^*))\\
&+ \frac{\mu_1 + \beta_1 x_1}{\beta_1}(U_1 - U_1^* - U_1^* \log(U_1/U_1^*))\\
&+ (W_1 - W_1^* - W_1^* \log(W_1/W_1^*))\\
&+ \Big(1 + \frac{\beta_1 x_1^2}{\tau_1 V^* - \beta_1 x_1^2}\Big) \sum_{j=2}^{N} (1 - \frac{1}{\eta_j})(\frac{\mu_j + \beta_j x_j}{\beta_j} U_j + W_j),\\
\text{with } \eta_j =& \frac{\frac{\beta_j^2 x_j^2}{\beta_j \tau_j} V^* + \Big(\frac{(\mu_j+\beta_j x_j)^2}{\beta_j \tau_j} - V^*\Big)\Big(\frac{(\mu_j+\beta_j x_j)^2}{\beta_j \tau_j} - \frac{\beta_j^2 x_j^2}{\beta_j \tau_j}\Big)}{\Big(\frac{(\mu_j+\beta_j x_j)^2}{\beta_j x_j} - \frac{\beta_j^2 x_j^2}{\beta_j \tau_j} - V^*\Big)^2} \text{ for } j = 2 \dots N.
\end{aligned}$$

This function is a Lyapunov function for the disease-steady state mentioned above. First it is positive, recalling that the classical function

$$\phi : \xi \to \xi - \xi^* - \xi^* \log(\xi/\xi^*)$$

for $\xi^* > 0$ is positive on $\mathbb{R}_+^*$, with a global minimum of 0 in $\xi = \xi^*$. Notice also that $\tau V^* > \beta_1 x_1^2$. The terms in the sum are also all positive, because for $j \in \{2 \dots N\}$, $\eta_j > 1$. Indeed, the

numerator of η_j can be expressed as

$$\underbrace{\Big(\frac{(\mu_j+\beta_j x_j)^2}{\beta_j x_j}-\frac{\beta_j^2 x_j^2}{\beta_j\tau_j}-V^*\Big)^2}_{\text{denominator of }\eta_j}+V^*\Big(\frac{(\mu_j+\beta_j x_j)^2}{\beta_j\tau_j}-V^*\Big)+\frac{\beta_j^2 x_j^2}{\beta_j\tau_j}\Big(\frac{(\mu_j+\beta_j x_j)^2}{\beta_j\tau_j}-\frac{\beta_j^2 x_j^2}{\beta_j\tau_j}\Big).$$

The fact that Strain 1 has the highest R_0^i value means it is associated with the lowest $\frac{(\mu_i+\beta_i x_i)^2}{\beta_i\tau_i}$. With the formulation above, this proves that for all $j=2\dots N$, $\eta_j>1$ and thus $1-\frac{1}{\eta_j}>0$. It is easy to verify that L evaluates to 0 at the point of the disease steady-state.

To compute the derivative of L along the trajectories, recall that $\frac{d}{dt}\phi(\xi)=\frac{\xi-\xi^*}{\xi}\frac{d\xi}{dt}$. Straightforward calculations lead to, after simplifications,

$$\begin{aligned}
&\dot L(V,U_1,W_1,\dots,U_N,W_N)=\\
&-\Big(\gamma+(\gamma+\tau_1U_1)\frac{\beta_1x_1^2}{\tau_1V^*-\beta_1x_1^2}\Big)\frac{(V-V^*)^2}{V}+\tau_1V^*U_1^*\left(3-\frac{V^*}{V}-\frac{W_1}{W_1^*}\frac{U_1^*}{U_1}-\frac{V}{V^*}\frac{U_1}{U_1^*}\frac{W_1^*}{W_1}\right)\\
&-\Big(1+\frac{\beta_1x_1^2}{\tau_1V^*-\beta_1x_1^2}\Big)\sum_{j=2}^N\tau_j\frac{U_j}{V}\frac{1}{\eta_j}\left(V^2+V\left(\eta_j\Big(\frac{(\mu_j+\beta_jx_j)^2}{\beta_j\tau_j}-V^*-\frac{\beta_j^2x_j^2}{\beta_j\tau_j}\Big)\right.\right.\\
&\qquad\left.\left.-\frac{(\mu_j+\beta_jx_j)^2}{\beta_j\tau_j}\right)+\eta_j\frac{\beta_j^2x_j^2}{\beta_j\tau_j}V^*\right).
\end{aligned}$$

Details of the calculations are not shown but can be made available. The first term in this expression is obviously negative along trajectories. The second term can be studied through the function defined on $\mathbb{R}_+^*\times\mathbb{R}_+^*$

$$(x,y)\to 3-x-y-\frac{1}{xy}.$$

This function is negative if $x+y>3$ or if $\frac{1}{xy}>3$. The complementary of this region is closed and bounded, and the function being continuous on this region, it admits a maximum value. Canceling the gradient leads to the only extremum $x=y=1$ where the function evaluates to 0. If we now replace x by $\frac{V}{V^*}$ and y by $\frac{W_1}{W_1^*}\frac{U_1^*}{U_1}$, we have shown that the second term in $\dot L$ is negative along trajectories, with a maximum value of 0 being reached at $V=V^*,U_1=U_1^*$ and $W_1=W_1^*$. The last term remains to be studied, especially the second order polynomials in V. For $j\in\{2\dots N\}$, the polynomial in the j-th term of the sum can be expressed (using the choice for η_j):

$$V^2+2\frac{\frac{\beta_j^2x_j^2}{\beta_j\tau_j}V^*}{\frac{(\mu_j+\beta_jx_j)^2}{\beta_j\tau_j}-\frac{\beta_j^2x_j^2}{\beta_j\tau_j}-V^*}V+\frac{\beta_j^2x_j^2}{\beta_j\tau_j}V^*\frac{\frac{\beta_j^2x_j^2}{\beta_j\tau_j}V^*+\Big(\frac{(\mu_j+\beta_jx_j)^2}{\beta_j\tau_j}-V^*\Big)\Big(\frac{(\mu_j+\beta_jx_j)^2}{\beta_j\tau_j}-\frac{\beta_j^2x_j^2}{\beta_j\tau_j}\Big)}{\Big(\frac{(\mu_j+\beta_jx_j)^2}{\beta_jx_j}-\frac{\beta_j^2x_j^2}{\beta_j\tau_j}-V^*\Big)^2}V.$$

Its discriminant is given by

$$\begin{aligned}\Delta =& 4\frac{\frac{\beta_j^2 x_j^2}{\beta_j\tau_j}V^*}{\left(\frac{(\mu_j+\beta_j x_j)^2}{\beta_j\tau_j}-\frac{\beta_j^2x_j^2}{\beta_j\tau_j}-V^*\right)^2}\times \\ & \left(\frac{\beta_j^2x_j^2}{\beta_j\tau_j}V^*-\left(\frac{\beta_j^2x_j^2}{\beta_j\tau_j}V^*+\left(\frac{(\mu_j+\beta_jx_j)^2}{\beta_j\tau_j}-V^*\right)\left(\frac{(\mu_j+\beta_jx_j)^2}{\beta_j\tau_j}-\frac{\beta_j^2x_j^2}{\beta_j\tau_j}\right)\right)\right), \\ =& -4\frac{\frac{\beta_j^2x_j^2}{\beta_j\tau_j}V^*}{\left(\frac{(\mu_j+\beta_jx_j)^2}{\beta_j\tau_j}-\frac{\beta_j^2x_j^2}{\beta_j\tau_j}-V^*\right)^2}\left(\frac{(\mu_j+\beta_jx_j)^2}{\beta_j\tau_j}-V^*\right)\left(\frac{(\mu_j+\beta_jx_j)^2}{\beta_j\tau_j}-\frac{\beta_j^2x_j^2}{\beta_j\tau_j}\right).\end{aligned}$$

For the same reasons as before, this quantity is negative. The polynomial thus has no real roots, and is always positive. This proves that each term in the sum in $\dot{L}$ is positive. Overall, we have shown that every term in derivative is negative along trajectories and they cancel out at the point of the disease steady-state. This concludes the proof of the global stability of this equilibrium. □

Prions come in all shapes and sizes - Mathematical modeling of protein self-aggregation and conversion

Abstract: Following the discovery that prions are self-replicating assemblies of proteins, mathematical models were developed in parallel with experimental methods in order to conceptualize this phenomenon. After four decades of research, much insight has been gained into protein misfolding processes and the neurodegenerative diseases which they cause. However, the complexity of these systems remains undiminished and the classical models of protein aggregation are now showing their limits. In particular, the observed spectrum of objects generated during the propagation of prions is not accounted for in any model, whereas it keeps expanding under the development of experimental tools. In the present manuscript, our aim is to identify the weaknesses of classical models of prion propagation in light of recent biological evidence. We then suggest modified and improved models, by including different processes, by adding more levels of organization and more diversity to protein aggregates. Three main topics are presented, corresponding to different instances of protein aggregation and different biological systems. The first part takes place in the mammalian nervous system, and investigates the self-aggregation kinetics of PrP, the aptly named prion protein. In the second part, we model the replication of protein aggregates inside dividing yeast cells, by proposing a novel multi-scale approach. In the third part, we explore the spatial propagation of small protein oligomers in the early stages of Alzheimer's Disease. These three axes are linked by the central role of structural diversity in the global protein aggregation system.
Key words: Protein aggregation, kinetic model, ordinary differential equations, dynamical systems.

Le prion sous toutes ses formes - Modélisation mathématique des processus d'agrégation et de conversion des protéines

Résumé : Depuis la découverte de la nature des prions, de nombreux modèles mathématiques ont été proposés afin de représenter ces assemblages de protéines et leur réplication. Après quatre décennies de recherche expérimentale et conceptuelle, la compréhension des phénomènes d'agrégation de protéines, ansi que des maladies neurodégénératives qui leurs sont associées, a grandement progressé. Cependant la complexité de ces systèmes reste entière, et les modèles classiques commencent à montrer leurs limites. En particulier, aucun modèle ne reproduit l'immense diversité des objets qui sont observés au cours de la propagation des prions, alors que l'on en découvre continuellement de nouveaux sous l'avancée des procédés expérimentaux. Dans ce manuscrit, notre objectif est d'identifier les faiblesses des modèles classiques à travers l'apport de résultats biologiques récents. Par la suite, nous proposons des améliorations à ces modèles en incluant de nouveaux processus, en ajoutant des niveaux de structuration et de diversité aux agrégats. Trois axes orientent les résultats, correspondant à trois contextes biologiques différents. La première partie se déroule dans le système nerveux des mammifères, et étudie la cinétique d'auto-agrégation de PrP, la bien nommée protéine prion. Dans la seconde partie nous abordons une approche multi-échelle novatrice pour représenter la propagation d'agrégats de protéines dans des cellules de levure en croissance. La troisième partie explore la dissémination spatiale de petits oligomères dans les étapes précoces de la maladie d'Alzheimer. Ces trois axes se recoupent autour du thème central de la diversité structurale et son rôle crucial dans la propagation.

Mots clés : Agrégats de protéines ; modèle cinétique ; équations différentielles ordinaires ; systèmes dynamiques.

Image en couverture : Représentation de la structure de la protéine PrP humaine.
Image from the RCSB PDB (rcsb.org) of PDB ID 1QM2 (Zahn, R., Liu, A., Lührs, T., Riek, R., von Schroetter, C., García, F. L., ... & Wüthrich, K. (2000). NMR solution structure of the human prion protein. Proceedings of the National Academy of Sciences, 97(1), 145-150.).

UNIVERSITÉ DE LYON